



UNIVERSITY OF TWENTE.

Faculty of Electrical Engineering,
Mathematics & Computer Science

Range characterization of backscatter wireless sensor networks

R.J. de Jong BSc

Committee:

dr.ir. A.B.J. Kokkeler
dr.ir. R.A.R. van der Zee
dr.ing. D.M. Ziener

Faculty of Electrical Engineering,
Mathematics and Computer Science
University of Twente
P.O. Box 217
7500 AE Enschede
The Netherlands

Abstract

Radios are a major consumer of energy in wireless sensor nodes. Reduction of this energy consumption can be a large push towards a cost effective realization of perpetual wireless sensor networks (perpetual WSN). Backscatter radio is an interesting candidate technology for realizing this objective, since it can significantly reduce the power and energy spent on radio transmission.

Backscatter radio enjoys several favourable properties for a sensor node, such as micro-watt level power consumption of data communication, however it's wide-spread usage is constrained by very limited range. This thesis aims to improve the range of backscatter transceiver(s) by investigating the relationship between range and radio properties such as sensitivity, communication throughput and power levels.

This thesis describes a design space exploration tailoring towards the specific requirements of WSNs. The design and implementation of a backscatter transceiver is demonstrated, while reviewing the applicability to perpetual WSN.

The results of this thesis are the design of an experimental backscatter platform, which allows for experimentation with backscatter communication. The design includes the low power exploration of modern analog and digital parts.

The design and implementation of a low power backscatter transceiver will be shown, which is expected to have an active power consumption of less than $100\mu\text{W}$. Measurements have been performed to characterize the link budget of the backscatter transceiver. The most important insight is how backscatter communication range can be improved.

Keywords: wireless sensor networks, backscatter radio, radio transceivers, low power design

Voorwoord

Een master scriptie schrijven betekent het afronden van een hoofdstuk in het leven. Maar voor mij betekent het ook de opstap om mijn promotiewerk te kunnen beginnen. Ik heb een hobbelige levensweg moeten afleggen om tot dit punt te komen. Daarin kan het leven net zoals zeilen kan zijn: je kan ook met tegenwind vooruit gaan. Ik wil graag even stilstaan bij enkele mensen die mij de afgelopen tijd hebben bijgestaan.

Als eerste mijn dank naar mijn ouders, Willy en Marinus. Ik weet nog goed de verbijsterde reactie toen ik zei aan de universiteit te willen studeren. Ik ben de eerste in de nabije familie die de stap naar de universiteit maakt. Dat was een grote stap.. van Wieringerwerf naar Enschede verhuizen, maar ook op persoonlijk vlak een nieuw leven opbouwen. Zij hebben mij al die jaren onvoorwaardelijk bijgestaan en gesteund.

Ik wil mijn broer Mark bedanken voor het bijstaan en meedenken, wanneer ik voor de wind of tegenwind had. We konden altijd goed relativeren met elkaar, aangezien we uit hetzelfde nest komen. Dit heeft mij de laatste jaren doen nadenken over wat ik wil, en gebracht tot waar ik nu sta.

Ik wil ook graag de broers van Willy bedanken, Koos en Frans. Jullie zijn voor mij altijd meer geweest dan "derdegraads" familie zoals dat officieel heet. De steun en interesse is net zo onvoorwaardelijk als mijn ouders geweest. Maar in het bijzonder ook de set van 2 rechter handen: van het verhuizen van inboedel tot het maken van een provisorische installatie voor de aircoconditioner thuis. Niets was teveel, ik kon altijd terecht.

Ik wil André Kokkeler bedanken voor het begeleiden van mijn master scriptie. Het was bijzonder leerzaam om te zien hoe je het overzicht kan initiëren en bewaren; over het onderzoek, de materie waar ik in probeer te verdiepen, het schrijven, maar ook af en toe daar buiten. Ik kijk erg uit onze samenwerking als aio.

Tenslotte wil ik mijn vriendengroep "de huiskamer" bedanken die tijdens de studie is ontstaan. Het is fijn om te zien dat we de studie straks allemaal tot een goed resultaat volbracht hebben. Jullie dus ook erg bedankt, maar ook evenveel success.

Allen, heel erg bedankt!

Hans de Jong

Enschede, 28 juni 2019.

Glossary

ambient backscatter Ambient backscatter is a variant of bistatic backscatter communication, where the continuous wave exciter has been replaced by an ambient communication beacon, for example a FM radio station, TV tower, WiFi access point, etc.

baseband signal The baseband signal is the communication signal before or after mixing with the RF carrier frequency.

bistatic backscatter In bistatic backscatter, the reader is separated from the exciter. Tags can use the exciter signal for backscatter communication, while other tags can receive the backscatter using their receiver for tag-to-tag communication.

chirp A chirp is defined within the CSS modulation, and describes the frequency sweep for a specific symbol.

duty cycling In the context of efficient electronics, duty cycling refers to the process of switching on and off a clock or power domain such that power can be saved. A domain can be as little as a few transistors up to whole boards and modules.

exciter An exciter provides an incident signal which can be scattered by tags in the network.

gateway A (often central) device that performs communication between the WSN and an external network, for example the internet.

isotropic radiator An isotropic radiator is an ideal representation of an antenna, which receives, transmits or "scatters" the same magnitude of electromagnetic waves on all directions.

mesh network A mesh network consists of multiple nodes or tags, which communicate between each other to relay packets so that the radio coverage is extended.

monostatic backscatter In monostatic backscatter, the exciter and reader are integrated into a single device called an interrogator. Tags can then communicate using backscatter. In this thesis, this arrangement is also called single-hop backscatter.

Range-Reach Budget (RRB) The product of the range (transmitter to receiver distance) and the reach (exciter to transmitter distance).

reflection coefficient The reflection coefficient, denoted by the symbol Γ , is a complex number that denotes the magnitude and phase of a reflected signal (also see scattering).

relay node All WSN nodes can perform relaying duties, where packets are relayed (received and retransmitted) such that it propagates through the network. A relay node sole purpose is relay functions.

scattering Scattering describes the reflection of electromagnetic waves, much like a diffuse surface may reflect light. The magnitude and phase of scattering is expressed using the reflection coefficient. load impedance modulation can be used to transmit symbols.

sink node A sink node is the target to which sample measurements is sent.

subcarrier A subcarrier is a concept of a baseband signal, where data is modulated on an intermediate frequency. When this intermediate frequency is then backscattered with a RF carrier, a frequency spacing is created equal to the subcarrier frequency.

tag-to-tag Communication among tags in a RFID network, often with the purpose to increase the networks range.

TSS Tangential Signal Sensitivity. For a square law / diode detector, this is typically the signal at which 8dB SNR remains after detection. It is typically modeled using Johnson-Nyquist noise of the dynamic impedance of the diode across the defined bandwidth.

wireless sensor node A device that can sample sensors and communicates the measurements wirelessly through a combination of relay node, sink node or gateway to an user.

Acronyms

RFID Radio Frequency Identification

IoT Internet of Things

ASK Amplitude Shift Keying

PSK Phase Shift Keying

FSK Frequency Shift Keying

MCU Microcontroller Unit

DMA Direct Memory Access

LDO Low-Dropout Regulator

RCS Radar Cross Section

ME Modulation Efficiency

LNA Low Noise Amplifier

WSN Wireless Sensor Network

CDMA Code Division Multiple Access

FDMA Frequency Division Multiple Access

TDMA Time Division Multiple Access

OOK On-Off Keying

PA Power Amplifier

COTS Complete Off The Shelf

GBW Gain-Bandwidth Product

CSS Chirp Spread Spectrum modulation

SWD Serial Wire Debug

MPN Manufacturer Part Number

BSP Board Support Package

Contents

Abstract	iii
Voorwoord	iv
Glossary	v
Acronyms	vii
Contents	viii
1 Introduction	1
1.1 Parking Sensor Networks	1
1.2 Backscatter radio	1
1.3 Thesis Outline & Contributions	2
2 Background	3
2.1 Backscatter Networking	3
2.2 Backscatter Radio	3
2.2.1 Modulated Scattering Technique	3
2.2.2 Backscatter Transmitter	4
2.2.3 Radar Cross Section & Modulation Efficiency	5
2.2.4 Carrier Configurations	6
2.2.5 Backscatter Receivers	7
2.2.6 Link Budget	8
2.3 Related Work	9
2.3.1 WSN nodes and RFID tags	9
2.3.2 Energy harvesting	9
2.3.3 Network Size	10
2.3.4 Processing energy costs	10
2.3.5 Offloading	10
2.3.6 Backscatter within IoT	11
2.3.7 Multiple access for simplex and duplex radios	11
2.3.8 Low power active radios	12
2.4 Research Boundaries	12
2.5 Research Questions	13
3 Tag-to-tag channel model	14
3.1 Introduction	14
3.2 Symbols	15
3.3 Symmetric & Asymmetric channels	15
3.4 Range-Reach Budget	16
3.5 Range vs Reach Analysis	17
3.5.1 Monostatic backscatter (single-hop)	17
3.5.2 Bistatic backscatter (multi-hop)	18

3.6	Node Positioning	19
3.6.1	Definitions	19
3.6.2	Exciter-receiver distance d_1	20
3.6.3	Transmitter-receiver distance d_2	20
3.7	Modulation Index	21
3.7.1	Definition	21
3.7.2	Minimum index in forward channel	21
3.7.3	Minimum index in backward channel	22
3.7.4	Comparison	23
4	Node Design	24
4.1	Node System Architecture	24
4.2	Design Space Exploration	24
4.2.1	Backscatter transceiver (analog)	24
4.2.2	Power Management	26
4.2.3	Backscatter transceiver (digital) & Controller	26
5	Backscatter Transmitter	30
5.1	Backscatter Modulation	30
5.1.1	Amplitude and phase modulation	30
5.1.2	Aliasing of BPSK modulation	30
5.1.3	Phase cancellation	31
5.2	Transmitter Design	32
5.3	Component schematic	33
6	Low power ASK receiver	35
6.1	Block Diagram	35
6.2	Circuit Design	35
6.2.1	Envelope Detector	36
6.2.2	Opamp 1/f noise mitigation	36
6.3	Circuit Analysis	37
6.4	Part Choice	37
6.4.1	Opamp Comparison	37
6.4.2	Passives	40
6.4.3	Performance	40
6.4.4	Comparator Hysteresis	40
6.5	Bitrate efficacy on sensitivity	40
7	Radio Firmware	42
7.1	Software Architecture	42
7.2	Radio Physical & Data Link	43
7.2.1	Tight Coupling	43
7.2.2	FM0 Encoding	43
7.2.3	Radio Frames & Packet definitions	44
7.2.4	Transmitter Implementation	44
7.2.5	Receiver Implementation	45
7.3	BSP	48
7.3.1	Timer & DMA	48

7.3.2	Radio RTL equivalent description	48
8	Implementation & Measurements	52
8.1	Experimental Platform	52
8.1.1	Board Design	52
8.1.2	Power Consumption	53
8.2	Measurements	54
8.2.1	Base-band Packet Tests	54
8.2.2	Sensitivity without exciter presence	55
8.2.3	Sensitivity with exciter presence	55
8.2.4	Board Power Consumption	56
8.2.5	Observations	57
8.3	Results	58
9	Conclusion & Discussion	59
9.1	Conclusion	59
9.2	Future Work	60
A	Receiver Circuit Analysis	61
A.1	Model	61
A.2	Transfer Functions	62
A.2.1	Input Band-pass filter	62
A.2.2	PGA Transfer Function	64
A.2.3	Resonance	64
A.2.4	Comparator	65
A.2.5	Complete Transfer Function	65
A.3	Noise Sources	66
A.3.1	Diode detector	66
A.3.2	Opamp bias network	67
A.3.3	Opamp voltage noise	67
A.3.4	Opamp current noise	68
A.3.5	Opamp feedback network	68
A.3.6	Comparator filter	69
A.3.7	Total Result	69
A.4	Comparator Hysteresis	70
B	Schematic & Bill of materials	72
	References	76

1 | Introduction

1.1 Parking Sensor Networks

Parking lots can be equipped with smart capabilities where each parking space has an occupancy sensor. A small wireless sensor node is installed that monitors the occupancy and communicates this to a gateway[1]. The gateway communicates the received samples to a server, which allows the road manager insight into the usage statistics of the parking facility.

Current generation sensor nodes are battery operated devices, with a typical battery life span of 3 to 5 years[2]. Sensor networks can span potentially multiple hundreds of devices, resulting in high maintenance costs. This thesis will study the application of backscatter in this industry application.

However, backscatter is often limited by its operating range. A current generation relay node product has a range of approximately 35m[2]. Range experimentation from backscatter literature show results an order of magnitude lower[3], [4], typically only several meters. It has been shown that exceptions are possible, however, these experiments have used very high exciter transmit powers[5] (several km, 90dBm TV tower as exciter, "passive" receiver consuming 0.54 μ W) or high sensitivity receivers[6] (2.8km, 30dBm exciter, -149dBm receiver, consuming 22mW).

If these sensor networks are going to be used in assistance of autonomous driving vehicles, for example, to guide them to free parking spaces in a busy city area, then the availability of WSN will play a crucial role. Availability is depletion of energy for individual sensor nodes, which may result in part(s) of a parking infrastructure to fail.

WSN's that contain perpetual sensor nodes could provide the necessary hardware to achieve such high availability while managing the maintenance costs. Perpetual operation can be implemented with the use of energy harvesting, where the energy supply originates from energy sources such as radio waves, heat, solar or other means.

Sensor networks with perpetual levels of operation require sufficient energy harvesting, improved energy and power management, in particular, energy efficient radios that offer sufficient communication range.

1.2 Backscatter radio

Radio is the major consumer of energy in a wireless sensor node[7], [8]. Reduction of this energy budget can be a key driver in the realization of perpetual sensor networks. Backscatter radio is an interesting candidate for realizing this objective since it can significantly reduce the power spent on a sensor node.

This thesis will focus on backscatter radio and will assume that accompanying energy harvesting is sufficiently scalable to be used in the μ W to mW of power range. However, ultimately any efficiency gains can result in less strict requirements, which may reduce the device form factor or bill of material costs.

Saving energy can also be accomplished in other means, which are summarized by Anastasi et al.[8]. Common techniques include hardware and data-based techniques, such as radio & CPU duty cycling and local data processing to reduce radio usage.

Bachir et al.[7] discusses multiple access protocols that reduce energy consumption by tuning the access scheme close to the traffic properties of the application: interval, quantity and

traffic direction.

The techniques described in these studies may apply to the sensor network built in this thesis as well but will be outside the scope of discussion.

1.3 Thesis Outline & Contributions

First background information is given about the operation of backscatter radio for IoT in general. Given this background information, an analysis can be performed about the application of backscatter for long-range wireless sensor networks, which will result in a proposal for a network design. The proposal includes key design constraints on the radio hardware level combined with the intrinsics of tag-to-tag communication.

Given this information, the focus shifts towards the sensor node components and the optimization of the radio power consumption. A brief design space exploration is performed to select the best (individual) components for a sensor node. A discrete radio transceiver employing backscatter will be designed combined with a low power receiver. Based on the theoretical model and performance simulations, some experiments will be performed to identify the correlation between these predictions.

The main contributions of this thesis are the extension of the operable range of backscatter sensor networks. This is accomplished by analyzing the properties of communication channels in a backscatter tag-to-tag network. These properties suggest hardware changes that could potentially increase the range of backscatter sensor networks. In addition, the low power design of a sensor node is shown using COTS (complete off the shelf) components.

2 | Background

This section aims to introduce the reader into backscatter radio. Common patterns and key constraints in the literature of backscatter sensor networks are highlighted, which are connected with the application to formulate the research questions of this thesis.

2.1 Backscatter Networking

Figure 2.1 shows the concept of a parking lot sensor network that employs backscatter. Each parking space has a red dot indicating a sensor node, which is located under a vehicle when the space is occupied. Each sensor will communicate the parking space status to a central sink node, which collects sensor data and can relay this to a gateway.

The backscatter network has a centralized exciter (depicted as "E"). The exciter transmits a continuous tone (single frequency) at a fixed power level, i.e. a radio signal with no modulation applied. At each node, information can be 'transmitted' by scattering the radio signal from the exciter. The scattering is accompanied in some power being absorbed or reflected back at the antenna of the node back to the exciter, hence the name back-scatter.

Note that "transmitting" is not in the literal sense (i.e. actively sending out power), although this type of radio will be called "scattering transmitter" in the remaining of this thesis. The term transmitter is used to indicate that it is a radio which is sending data (i.e. transmitting). The process of scattering these radio signals can be accomplished by changing the load impedance on the antenna[9].

Introducing backscatter into a wireless sensor network poses a few challenges. Each node will have a path loss proportional to r^2 with respect to the exciter, making it such that the scattering transmitter at each node has a different range. In addition, after scattering there is an additional path between the scatterer and receiver is present (also proportional to r^2), creating a large path loss proportional up to r^4 ([9], eq 26).

Moreover, the receiver then needs to receive the information signal from a combination of the exciter signal (called incident wave) and the scattered signal (the desired information). This problem is different from conventional receivers, since the "interference" in this case could be in-band.

2.2 Backscatter Radio

2.2.1 Modulated Scattering Technique

Scattering is the process of scattering electromagnetic waves originating from an exciter source using an antenna[9]. The scattering can electronically be modulated to reflect or absorb the signal, realized by varying the load impedance on the antenna.

Figure 2.2 shows this process in the application setting of RFID, where an interrogator/reader (exciter + receiver) and a backscatter tag is shown. The exciter emits a single tone that reaches the backscatter tag. The tag modulates the load impedance of the antenna to scatter this single tone, which emission approaches an isotropic radiator[10]. The modulated scattering can then be picked up by the receiver in the interrogator/reader.

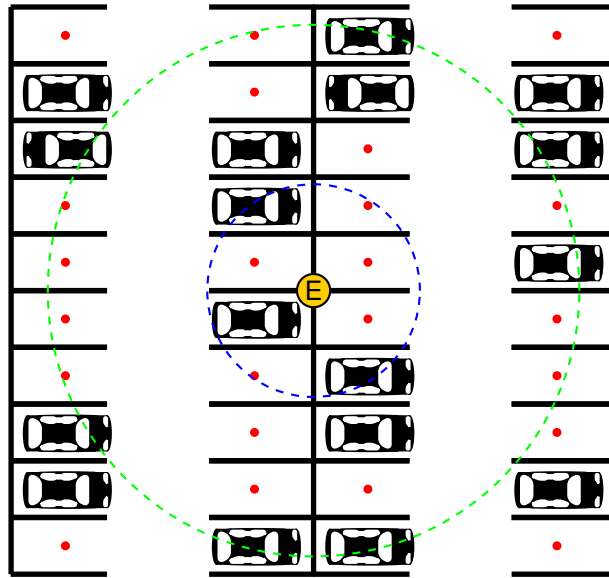


Figure 2.1: A smart parking lot with backscatter infrastructure

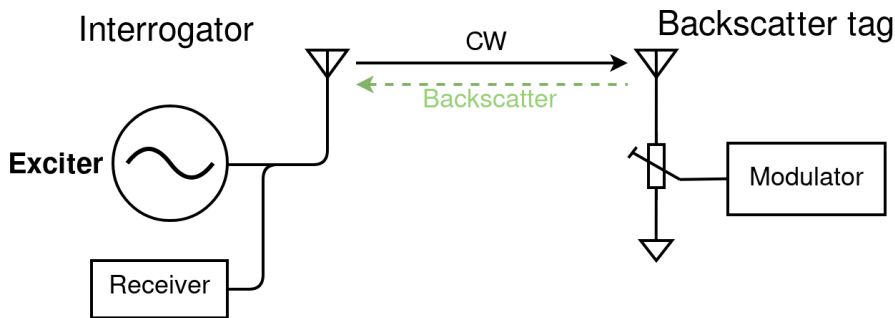


Figure 2.2: RFID communication setup using backscatter

Scattering can be realized both with real (resistive) and complex (capacitive, inductive) load modulation. This results in amplitude (ASK) and phase modulation (PSK) [11]. FM (FSK) modulation in backscatter can be realized by using AM/PM modulation and a subcarrier, introducing a frequency shift from the exciter tone frequency[12].

Backscatter implies that the scattered signal is destined to reach back to the exciter, however, this is not necessary. The scattering antenna can approach an isotropic radiator[10], which means that the signal can be picked up by other devices from all directions.

2.2.2 Backscatter Transmitter

Scattering is established by (mis)matching the load and antenna impedance. The quantity of mismatch can be expressed using S_{11} (further referenced as reflection coefficient $\Gamma_{L,i}$, as defined in figure 2.3)[13]:

$$\Gamma_{L,i} = \frac{Z_{L,i} - Z_a^*}{Z_{L,i} + Z_a} \quad (2.1)$$

where $Z_{L,i}$ is the load impedance, i is the index of the load, Z_a is the antenna impedance and Z_a^* is the complex conjugate of Z_a . This equation shows that $\Gamma_{L,i} = 0$ when $Z_L = Z_a^*$.

Figure 2.3 shows a binary backscatter transmitter. The antenna is loaded with impedance $Z_{L,1}$ or $Z_{L,2}$ depending on the (electronic) switch position. Equation 2.1 applies individually for each load, depending on the switch position, resulting in $\Gamma_{L,1}$ and $\Gamma_{L,2}$.

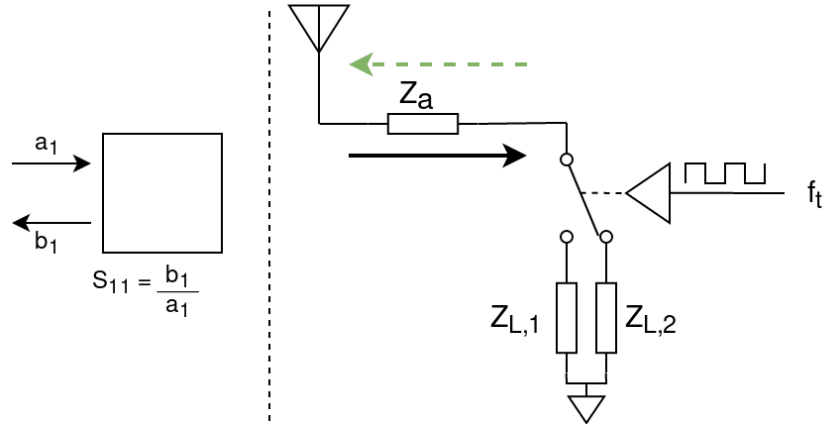


Figure 2.3: Binary backscatter transmitter showing dualities with a one-port scattering network

The figure shows tones with frequency f_c and f_t , where f_c indicates the carrier (or incident wave) from the exciter and f_t the symbol stream to transmit. The scattering modulation leads to a mixing effect between f_c and f_t , scattering the dominant frequency components $f_c + f_t$ and $f_c - f_t$ [12], [14]–[16]. Since the impedance modulation is performed using discrete levels, many harmonics may be emitted as per the square wave frequency spectrum[6].

Several improved designs of the scattering transmitter exist, most commonly scaling to 4 load impedances. These can be used to transmit multiple bits per symbol period[16]–[18], such that higher throughput can be sustained in favourable channel conditions.

More than 2 load impedances may also be needed to perform phase cancellation[19], [20]. Phase cancellation uses a combination of ASK and PSK modulation in order to maximize the received amplitude at the receiver, depending on the arrived phase of the propagated scattered wave versus that of the exciter[20].

Zhang et al. [21] shows that a single side-band backscatter signal can also be created by backscattering the carrier twice with slight delays of the baseband signal.

The realization of multiple reflection coefficients does not require 4 distinct load impedances. Daskalakis et al.[16] uses an RF transistor being driven by a DAC to vary the impedance level.

2.2.3 Radar Cross Section & Modulation Efficiency

Scattering is also commonly used in radar applications, where the quantity of scattering is expressed using the radar cross section RCS. The RCS expresses how large the cross section (expressed as a surface area) of an imaginary sphere needs to be to represent that object[22]. The sphere is used, since its cross section remains the same independent of the direction at which the object is viewed.

The RCS of an antenna can be described as the field scattered from the structural mode contribution and antenna mode contribution. Herein the structural mode describes the scattering from the physical representation of the antenna. The antenna mode contribution, however, depends on the load impedance matching of the antenna and can be modulated[23]. Bolomey et al. uses the following definition for the antenna-mode contribution of the RCS[9], [23]:

$$\sigma_T^{AM} = \frac{\lambda^2 G_T^2 (\text{Re}\{Z_a\})^2}{\pi |Z_{L,i} + Z_a|^2} \quad (2.2)$$

where λ is the wavelength of the exciter signal and G_T is the gain of the tag antenna. The differential RCS is the difference between 2 load impedances $Z_{L,1}$ and $Z_{L,2}$. The differential

RCS can be described as [9], [24]:

$$\Delta\sigma_T^{AM} = \frac{\lambda^2 G_T^2}{4\pi} |\Gamma_{L,1} - \Gamma_{L,2}|^2 \quad (2.3)$$

The change in power received by the exciter in backscatter is then [9], [24]:

$$\Delta P_{AM}^{RCS} = \frac{\lambda^2 G_R^2 \Delta\sigma_T^{AM}}{(4\pi)^3 r^4} P_a = \frac{\lambda^4 G_T^2 G_R^2}{(4\pi)^4 r^4} |\Gamma_{L,1} - \Gamma_{L,2}|^2 P_a \quad (2.4)$$

where G_R is the gain of the reader antenna, r is the distance between the interrogator and tag and P_a is the power output of the exciter.

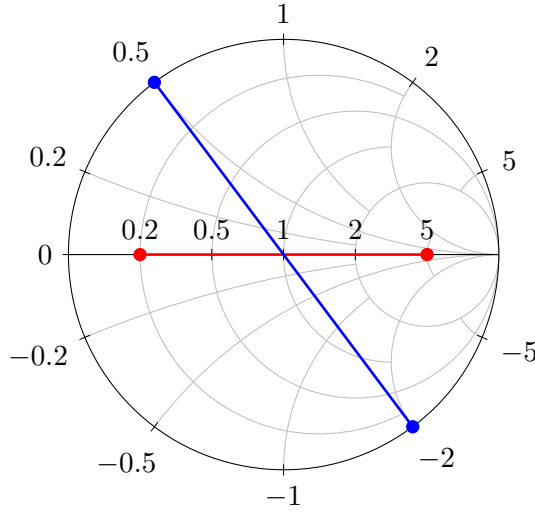


Figure 2.4: Smith chart with $Z_a = 50\Omega$ representing two example binary impedance pairs of $Z_{L,i} = (10\Omega, 250\Omega)$ (red) and $Z_{L,i} = (25j\Omega, -100j\Omega)$ (blue).

Equation 2.4 shows that power change is maximized when the distance between $\Gamma_{L,2}$ and $\Gamma_{L,1}$ is maximized. Bolomey et al.[9] have introduced the term modulation efficiency (ME) for this scalar value, which expresses the effectiveness of the chosen backscatter impedance loads:

$$ME = |\Gamma_{L,1} - \Gamma_{L,2}|^2 = \frac{4R_T^2 |Z_{L,1} - Z_{L,2}|^2}{|Z_a + Z_{L,1}|^2 |Z_a + Z_{L,2}|^2} \quad (2.5)$$

where $0 \leq ME \leq 4$.

The Smith chart of figure 2.4 shows 2 binary impedance example pairs with $Z_{L,i} = (10\Omega, 250\Omega)$ (red) and $Z_{L,i} = (25j\Omega, -100j\Omega)$ (blue). The scalar factor ME is 1.78 for the red impedance pair, and 4 for the blue impedance pair, highlighting the importance of choosing "conjugate" modulation loads to maximize the magnitude of the chosen impedance pair.

2.2.4 Carrier Configurations

Borrowing terminology from radar, the setup is shown in figure 2.2 was a monostatic backscatter configuration. The exciter and receiver are integrated into the same device, which is a typical configuration used in RFID. Figure 2.5 shows two alternative exciter configurations.

In bistatic backscatter, the exciter and receiver are now separated, however, the incident wave on the backscatter transmitter is still a single tone. In ambient backscatter a similar setup

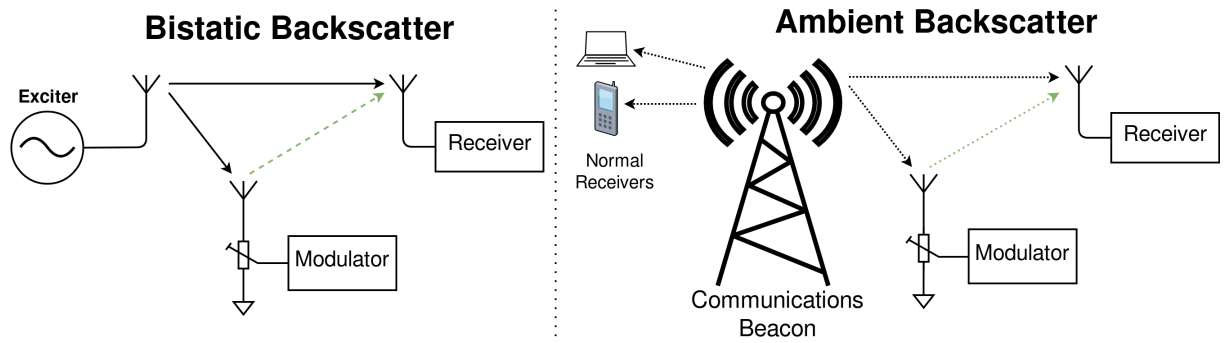


Figure 2.5: Bistatic and ambient backscatter carrier configurations[25]

as bistatic is used, however, an already modulated incident wave (e.g. a GSM or WiFi signal) is used as excitement signal.

Ambient backscatter has received increasing attention in the literature. Iyer et al.[26] shows a cross-protocol (back)scattering where a BlueTooth signal is used as an exciter source, and the (back)scattered signal is modulated and translated to be compatible with WiFi. This allows compatibility with existing devices such as laptops and smartphones, and does not require dedicated infrastructure (pure tone exciters) to function. The low power properties of backscatter allow these devices to be used in new applications where power is hard to apply, such a patient monitoring.

However, it is considerably more difficult to utilize ambient signals in sensor networks due to a poor link budget, resulting in poor range[27], [28]. The poor link budget originates primarily from the significant path loss from the ambient exciter signal to the backscatter transmitter[28]. In addition, the ambient exciter location is unpredictable/uncontrollable, which makes the network design highly unpredictable.

2.2.5 Backscatter Receivers

A "backscatter receiver" can be little different from regular RF receivers, as shown in studies [6], [12], [21]. However, the unique issue in backscatter receivers is that they must function with the presence of a strong exciter signal, which is in-band. This results in extremely low modulation indices ($< 1\%$)[29].

Mixer based receiver architectures are seldom used in low power radios, due to high power components such as oscillators and active mixers. Typically diode envelope detectors and ASK modulation is used (as shown in figure 2.6), in which the sensitivity is roughly -40dBm to -50dBm [30], [31].

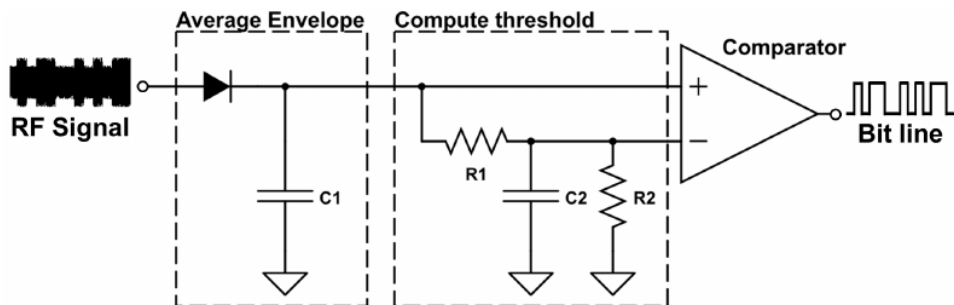


Figure 2.6: Schematic diagram of a low power envelope detector [5]

Karimi et al.[29] shows a variant of this receiver while adding base-band amplification between the detector and comparator. The amplification is configured to only pass the symbol frequency band. Due to the additional gain and relative carrier suppression, the design can receive signals with a modulation index of 0.6%[29]. More importantly, an expression for the modulation index has been identified using the channel length r_r between the scattering transmitter and receiver:

$$m(r_r) = \frac{1}{1 + k(r_r)} \text{ with } k(r_r) = 2 \cdot \frac{4\pi r_r}{G_T \lambda} \sqrt{\frac{P_{RX}}{P_{TX}}} \quad (2.6)$$

where P_{RX} is the incident power at the receiver, and P_{TX} is the incident power at the transmitter. The modulation index decreases for a longer transmitter-receiver channel, but also for a higher exciter incident power at the receiver (the scattered signal has proportionally weakened), or less incident power at the scattering transmitter.

2.2.6 Link Budget

Backscatter has a unique link budget, in that it has two RF channels with only a single excitation source. In an ideal model, where the RCS of the scattering antenna is ideal[10], the exciter and scattered signal spread using an isotropic radiation pattern. Effectively, this means that two Friis transmission equations (free space path loss for an isotropic radiator) must be put together to calculate the link budget. The path loss in a single path channel using the Friis transmission equation is:

$$L(r) = G_T G_R \left(\frac{\lambda}{4\pi} \right)^2 \frac{1}{r^n} \quad (2.7)$$

where n is the path loss exponent (typically $n = 2..4$). Consequently, if an arrangement such as the one in figure 2.7 is made, then the received scattered power is[9], [32]:

$$P_R(r_t, r_r) = P_T L(r_t) |\Gamma_{L,1} - \Gamma_{L,2}|^2 L(r_r) = P_T G_T^2 G_R^2 |\Gamma_{L,1} - \Gamma_{L,2}|^2 \left(\frac{\lambda}{4\pi} \right)^4 \left(\frac{1}{r_t \cdot r_r} \right)^n \quad (2.8)$$

where P_T is the exciter transmit power, r_t is the channel length of the exciter to backscatter transmitter, and r_r is the channel length of backscatter transmitter to the receiver. Equation 2.8 can be rewritten into[4]:

$$r_t \cdot r_r = \sqrt[n]{\left(\frac{\lambda}{4\pi} \right)^4 \frac{P_T}{P_R} G_T^2 G_R^2 |\Gamma_{L,1} - \Gamma_{L,2}|^2} \quad (2.9)$$

where P_R now resembles the minimum signal strength at the receiver (sensitivity).

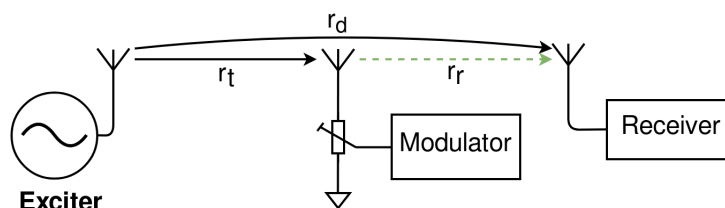


Figure 2.7: Example of a backscatter link

A crucial insight is that the maximum channel length is determined by the product of and not the sum. The minimum "range" $r_d = r_t + r_r$ is achieved by choosing $r_r = r_t$. This non-intuitive behaviour has often been observed in backscatter literature[6], [12], [27].

2.3 Related Work

This section discusses some trends in the literature of WSN and RFID employing backscatter.

2.3.1 WSN nodes and RFID tags

The boundaries between RFID and WSN are fading. Both RFID and WSN implementations are appearing that are passive (using energy harvesting) and active (battery) powered.

RFID is used for identification purposes, which can also be seen as a variant of sensor sampling, however, the sampling event is often triggered by proximity or a physical event. Another key differentiation in RFID is the protocol role of each device, such as the EPCglobal Gen2 specification [33]. Here the interrogator always initiates communication with tags, while tags only respond to incoming commands.

This is in contrast to wireless sensor networks where nodes operate autonomously. Nodes adhere to a MAC scheme and communicate with each other to create a network of nodes[7]. The firmware on each node can decide when it needs to sample & process sensor data, rather than an external device triggering it.

There is common literature applying backscatter communication in both contexts. Throughout this thesis, the terms nodes and tags may be used interchangeably, as it depends on the application context which role a device may serve.

2.3.2 Energy harvesting

A reliable source of energy is necessary such that backscatter tags/nodes can operate perpetually. Since batteries result in a limited lifetime, it is necessary to include energy harvesting to create perpetual sensor nodes and networks.

Common energy harvesting sources include solar (photovoltaic cells), vibration (piezoelectric), thermoelectric (peltiers), magnetic (inductive coupling) or RF (electromagnetic). The latter 2 are commonly used in RFID tags, where inductive coupling requires a short range (<1 meter) and RF energy harvesting tends to be applicable in mid-range applications (several meters).

Although RF energy harvesters are popular to combine with backscatter radio, its limitations must also be highlighted. RF energy harvesters found in literature can operate down to -25.7dBm with 37% efficiency[34], yielding $1\mu\text{W}$ of power.

Although this is a useful amount of power; there are 2 issues in relying on the stretching of this performance boundary. First, $1\mu\text{W}$ is typically the leakage of conventional electronics (typically also in the neighbourhood of $1\mu\text{W}$)[35], meaning there is scarce energy budget to perform additional networking functions.

In addition, -30dBm equals $1\mu\text{W}$ of power; meaning that pushing the efficiency of harvesters to lower power levels will not yield a satisfactory increase in realizable range, as the absolute amount of available power will also decrease. Accompanying the decreasing amount of available power, energy harvesters will be proportionally less efficient due semiconductor threshold voltages[34].

A range example: a typical exciter is limited to approximately 30dBm by many government regulations[36]. Thereby a 55dB of path loss is tolerable that can yield $1.0\mu\text{W}$ energy harvesting

when an energy harvester is realized with 37% efficiency at -25.7dBm[34]. A free-space path loss of 55dB at 868MHz is reached for a line of sight channel of only 15.5 meters.

If perpetual operation is necessary outside of this range, then it is necessary to use alternative energy harvesting sources.

2.3.3 Network Size

The range is defined by the link budget, which is bound by the exciter output power (up to 30dBm[36]) and the receiver sensitivity. Typical passive (wake-up) receivers are sensitive to approximately -50dBm with single-digit kilo-bits per second[31] and $<100\mu\text{W}$ (868MHz band), resulting in 80dB link budget. Then in a monostatic backscatter configuration, a range of 7.5m is possible[4].

Although the link-budget can be increased by using active coherent receivers and/or LNAs, this is typically at the dramatic increase of power consumption. Talla et al. performed an experiment using a LoRa radio with -149dBm sensitivity at 18bps[6], however, the chipset had a power consumption of 22mW. In this experiment, a link budget resulted in a range 2.8km, by placing the scattering transmitter only 5 meters from the exciter.

Although the experiment shows that theoretically backscatter can be used to create very large communication links, the chosen radio is not a terrific match for this application due to the power consumption. In addition, the experiment also showed that the range dropped dramatically as soon as the transmitter was placed further from the exciter.

2.3.4 Processing energy costs

It has been shown that it is possible to build backscatter transmitters and receivers with a very low analog power consumption ($<0.5\mu\text{W}$, 1kbit/s)[5]. The dramatically reduced cost of radio transmitting may break the rule of thumb which states that local processing is cheaper than radio usage[37].

Microcontrollers are popular in WSN because of their low power operation, low cost per sensor node, and high flexibility in custom applications. Modern 16-bit and 32-bit microcontrollers are available with power consumption figures of approximately $200\mu\text{W}$ at 1MHz[38]–[44]. Despite these efficiency figures, such microcontrollers can only run at an average clock speed of 250Hz for it not to dominate the energy budget (neglecting any leakage in sleep).

2.3.5 Offloading

With the relatively high cost of processing, a popular architecture is to offload as many computations onto a central unit that is less bound by an energy budget. The most intuitive node of choice would be the data sink which collects all sensor data and communicates it to the necessary equipment for usage[45].

In an abstract way backscatter is also a form of offloading. The cost of transmitting RF power is offloaded onto an exciter, which enables backscatter transmission at a very low cost for the node.

However, offloading may have some side effects. If the data processing is offloaded to a central node, then it is to be expected that the volume of traffic to that node will increase. This puts pressure on the available bandwidth in the network and would require higher bitrate radios to be used. This is in contrast with many backscatter implementations that are low bit rate ($\geq 10\text{kbit/s}$)[35].

Additionally, when radios are used in a tag-to-tag or multi-hop network, nodes will need to act as relays for neighbouring nodes traffic. This means that the energy expenditure of a single node is a function of its own duties but also the neighbour's traffic output. The energy savings on a single node may be ruled out by the inflation of relaying traffic.

2.3.6 Backscatter within IoT

Backscatter radio implementations for IoT can be subdivided into two major categories: RFID/WSN and personal media devices. Tag/sensor nodes typically operate in the 434MHz and 868MHz ISM frequency bands, which are used by conventional IoT and WSN devices. Most implementations use a custom protocol and FM0 encoding taken from the EPCglobal gen2 protocol[33], although there has also been work performed on LoRa[6] and 802.15.4[46].

Personal media devices aim to operate directly with consumer media equipment such as home routers, computers and smartphones. Typically these devices use Bluetooth[12], [47] or WiFi[21], [26] protocols, with a mixture of pure tone and ambient excitors.

Although both categories reside in the IoT design space, the used radio technologies are different. 2.4GHz multimedia communication standards often use frequency-hopping, higher order modulation schemes such as QAM and therefore need coherent receivers to obtain the amplitude and phase (I/Q) information[26].

Sensor network radios focus on the best sensitivity (range), and while maintaining efficient & low power operation. Typically this limits the modulation type to simpler variants such as (a mixture) of ASK or PSK modulation schemes[29]. Then an ASK/OOK receivers can be built using a non-coherent architecture, which can be largely passive as figure 2.6 has shown.

2.3.7 Multiple access for simplex and duplex radios

In a sensor network, multiple nodes may want to use the RF spectrum simultaneously to communicate. A multiple access regime, either at a physical or packet level is needed, to deal with the potential collisions of symbols.

When considered at a physical level, this subject ties directly into the necessity for simplex or duplex radios.

In order to strive for low cost and power sensor nodes, networks using only a backscatter transmitter have been shown to work[15] using FDMA. This results in multiple communication channels of about 5kHz per sensor. Although the work uses FM modulation, it is foreseeable that digital symbols (e.g. FSK or OOK) are used instead.

One problem is that scaling such a sensor network results in a large number of channels to be assigned for each sensor. Additionally, the sensors showed by Kampianakis et al.[15] continuously transmit measurement data, while most sensor applications only need to sample data occasionally (once per second or minute).

Spectrum reuse is temporally non-existent since transmit-only nodes cannot adhere to a TDMA or contention based MAC scheme (synchronization needs a receiver). Spectrum reuse thereby needs to be established spatially, such as a frequency plan (depending on their location) for each sensor node before deploying them. The latter can be accomplished by using different subcarrier frequencies in the transmitter[15].

Netscatter[45] shows an alternative solution for sensor networks where multiple access is needed. In this work, a synchronous CDMA scheme is created using CSS coding and OOK. Each sensor node is assigned a single symbol of a traditional CSS modulation (allowing CDMA). Sensors then modulate symbols using OOK.

The complexity of receiving this CDMA scheme is significant, removing the possibility of a mesh network. Nodes however, still need a receiver with accurate synchronization to the exciter, since the CSS chirps are very sensitive to cyclic shifts from time latencies of the chirp.

2.3.8 Low power active radios

Although backscatter is promising as a low power transmitter in sensor nodes and tags, it is important not to forget how these implementations compare to state-of-the-art active transceivers.

The RF power amplifier (PA) is dominant in the power consumption of a transmitter. A CMOS implementation by Pandey et al.[48] has been demonstrated that consumes $90\mu\text{W}$ at -17dBm output ($20\mu\text{W}$) and 200kbps, with a PA efficiency of 22%. Additionally, higher power transmitters have been shown with PA efficiencies in the order of 35 to 40% [49] [50].

State-of-the-art CMOS receivers also significantly outperform discrete counterparts. For example, Huang et al.[51] has shown a $123\mu\text{W}$ wake-up receiver with -81dBm sensitivity (100kbps).

Hypothetically, if designs from Pandey et al.[48] and Huang et al.[51] are cherry-picked into a single transceiver, then a link budget of approximately 64dB is established with $\sim 100\mu\text{W}$ (assuming half-duplex operation with full power gating support) of active power consumption. A 64dB link budget in the 868MHz band could allow a range of up to 43m (using eq 2.7).

Huang et al.[52] demonstrated an ASIC OOK envelope detector receiver, which can be made power-scalable and bit-rate scalable to influence the required sensitivity. Here it is observed that a higher amplification factor yields more sensitivity, but also increases power consumption. However, a lower bit-rate can also be used to increase the sensitivity of the receiver at the same power level.

This raises the question whether a similar trade-off and improvement can be made in a backscatter receiver, where the bit-rate is traded for sensitivity at a fixed power level. It was shown in equation 2.9 that receiver sensitivity plays a major role in the achievable distances of a backscatter communication system.

2.4 Research Boundaries

Wireless radios are becoming increasingly energy efficient, which is not limited to just backscatter radio technology. Without overstating the promise of backscatter radio, it is clear that both active and passive radios are an interesting option for wireless sensor networks.

Backscatter radio has the advantage of using fixed-power transmitters due to the absence of a power amplifier in the design. However, the range, and in particular the variability, is a bottleneck. It has been shown that monostatic backscatter is unfavourable in terms of range[12], [27]. A bistatic configuration, where either the exciter-transmitter or transmitter-receiver channel is minimized, allows for a significant range improvement[6].

However, bistatic backscatter implies that nodes must perform relay duties as well (tag-to-tag or multi-hop radio). This increases the radio duty cycle on a node, thereby increasing its energy consumption. In particular nodes near the gateway (and exciter, as per the introduction), which is at a central position in the network, must relay more packets.

Spatial information about these nodes suggests that the radios can trade some sensitivity for increased throughput, which could reduce the radio duty cycle again. Likewise, spatial information about nodes in outer regions tells that their relaying traffic is limited, and as such can communicate at a reduced bitrate for improved sensitivity, and potentially improved range.

This thesis will perform research to qualify and quantify backscatter radio range improvement by using bitrate as the main parameter to influence of the backscatter transceiver, that can be used for multi-hop backscatter. Design, dimensioning and experimentation are performed using an experimental backscatter node. Experimental results will be compared with models to prove or disprove the hypothesis.

2.5 Research Questions

The main research question is:

Can lowering the bitrate of a backscatter transceiver be used to increase the range of a multi-hop backscatter network?

The sub-research questions are as follows, with parenthesis indicating which chapter discusses the question:

1. What is the relationship between link budget and range in a single-hop and multi-hop backscatter network? (Chapter 3)
2. How (much) will a multi-hop network improve the range in a backscatter network over a single-hop network? (Chapter 3)
3. What is the design space of a backscatter radio to be used in wireless sensor networks? (Chapters 4, 5, 6 and 7)
4. What is the relationship between symbol frequency and receiver sensitivity? (Chapter 6)
5. What is the power consumption of such a radio in transmit and receive? (Chapter 8)
6. What is the backscatter range and throughput while staying under $100\mu\text{W}$ active power consumption for the complete backscatter node? (Chapter 8)

3 | Tag-to-tag channel model

This chapter will quantify the performance of backscatter channels and nodes placement. In addition, the model can indicate the required receiver such that a sufficient range can be realized.

3.1 Introduction

Figure 3.1 shows a typical backscatter channel. The exciter and 2 tags are placed along a one-dimensional line, with distances d_1 and d_2 separating them. Both tag 1 and tag 2 have a receiver and scattering transmitter (depicted in the figure as an impedance modulator), which can be used as a half-duplex radio transceiver.

In a forward channel (abbreviated as FW channel), where tag 1 sends a message to tag 2, the path length of the exciter to the receiver (direct path; r_d) is $r_d^{FW} = d_1 + d_2$. The product of path lengths exciter-transmitter (transmitter path; r_t) and transmitter-receiver (receiver path; r_r) is $r_t^{FW} r_r^{FW} = d_1 d_2$.

In a wireless sensor network with tag-to-tag communication, a node may reply to packets (handshaking) or must relay them. Figure 3.2 shows the case where the same node positions are taken, but the scattering channel is reversed creating a "backward" channel, i.e. tag 2 sends a message to tag 1.

In a backward channel (abbreviated as BW channel), the path length definitions change. Now the exciter-receiver path is $r_d^{BW} = d_1$, while $r_t^{BW} r_r^{BW} = (d_1 + d_2) \cdot d_2 = d_1 d_2 + d_2^2$.

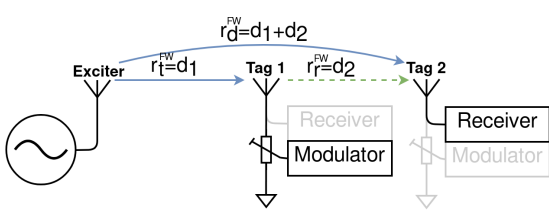


Figure 3.1: A forward facing channel.

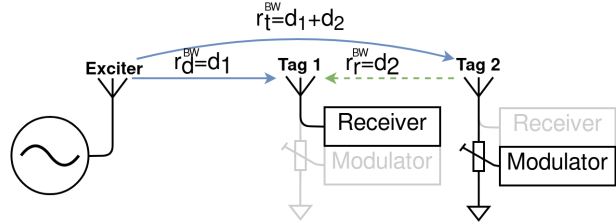


Figure 3.2: A backward facing channel.

In both figures, the distance parameter d_1 is varied, which places "tag 1" closer or farther from the exciter. The channel lengths r_t and r_r are defined separately for each channel, where $r_t^{FW} = d_1$, $r_r^{FW} = d_2$, $r_t^{BW} = d_1 + d_2$ and $r_r^{BW} = d_2$. The length $d_1 + d_2$ is kept constant at 10m, meaning that $d_2 = 10 - d_1$. The line of sight path loss functions for the FW channel and BW channel are:

$$L^{FW}(d_1) = L(r_t^{FW})L(r_r^{FW}) = L(d_1) \cdot L(10 - d_1) \tag{3.1}$$

$$L^{BW}(d_1) = L(r_t^{BW})L(r_r^{BW}) = L(10) \cdot L(10 - d_1) \tag{3.2}$$

The value of d_1 for which the maximum loss is present in the channel is when:

$$\arg \max_{d_1 \in [0,10]} L^{FW}(d_1) = d_2 \tag{3.3}$$

$$\arg \max_{d_1 \in [0,10]} L^{BW}(d_1) = 0 \tag{3.4}$$

In an FW channel, the maximum loss is when $d_1 = d_2$ and since $d_2 = 10 - d_1$, it means that $2d_1 = 10$ and thereby $d_1 = d_2 = 5m$. The importance of this difference is shown in figure 3.3 and 3.4. The figures plot $L^{FW}(d_1)$ and $L^{BW}(d_1)$ using equation 2.7 with $\lambda = \frac{300}{434}$.

For the BW channel, the worst path loss is attained when d_1 is minimized. This behaviour highlights that while scattering channels may work in a forward configuration, however, they may fail in a backward configuration.

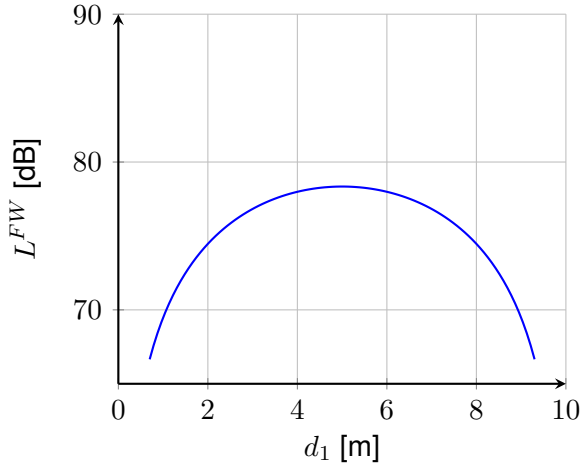


Figure 3.3: Path loss in a FW channel as a function of d_1

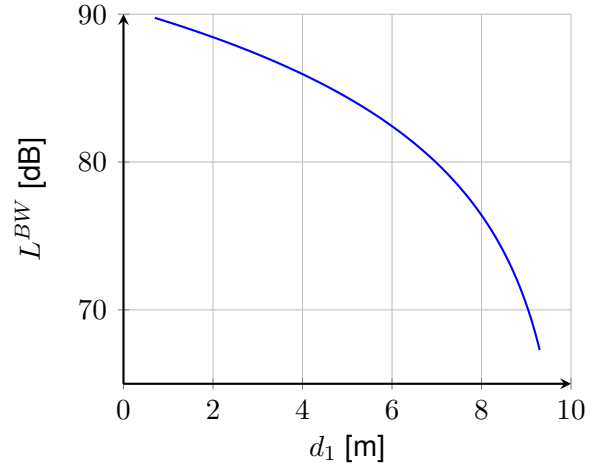


Figure 3.4: Path loss in a BW channel as a function of d_1

3.2 Symbols

Some symbol representations will be used to make the drawing of node layouts simpler. Figure 3.5 shows the 4 vertices (nodes) and 2 edges (channel) to be used in the remainder of this thesis. The "I" node stands for interrogator and refers to an exciter with a reader. The "E" symbol is an exciter only. The "T" and "R" gray symbols both indicate a tag equipped with a half-duplex radio. The symbol shows whether the transmitter ("T") or receiver ("R") is active.



Figure 3.5: Symbols used in this chapter

The 2 edges indicate the communication channels. A blue solid edge indicates an unmodulated incident signal from the exciter. When the edge is connected to a transmitter, it indicates the reach r_t . When the edge is connected to a receiver, it indicates the incident wave of the exciter on the direct path r_d . A green dashed edge indicates a scattered signal, which is between the transmitter and receiver and is the range r_r .

3.3 Symmetric & Asymmetric channels

In the introduction, the path loss for an FW and BW channel was shown when nodes are placed on a line in 1 dimension. This placement shows the largest difference in path loss between both

communication directions. However, it is also possible to create symmetric channels when nodes are placed on a 2-dimensional grid.

Figure 3.6 shows the various arrangements of backscatter nodes. Part (a) shows 2 symmetric channels, where both tags are placed at an equal distance from the exciter. In both directions of channel r_r , the exciter-transmitter r_t and exciter-receiver r_d distances are equal, thus $r_t = r_d$. Thereby the scattering channel behaves symmetrically.

In parts (b) and (c) however, when the channel r_r is reversed, a large difference in the exciter-transmitter r_t and exciter-receiver r_d is observed. This highlights the loss characteristics of paragraph 3.1, where a backward channel is far less favourable than a forward channel.

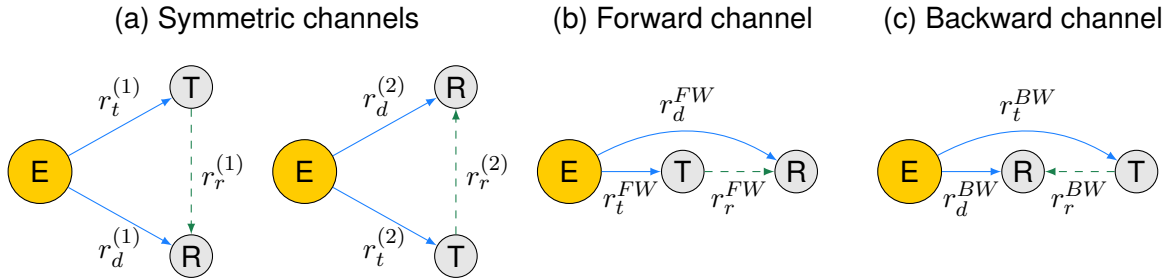


Figure 3.6: Symmetric and asymmetric (forward & backward) channels in backscatter

3.4 Range-Reach Budget

The previous section(s) showed a unique property of scattering radio systems, where their radio link performance is dependent on two channels. Naming either one of these channels "the range" is confusing. Specifically, the product of r_t and r_r shows that either the distance from exciter (in r_t and indirectly in r_d) or the distance between tags (r_r) can be optimized.

Conventional radio systems use the term "range" to name the channel length with modulated information (r_r). However, backscatter radio introduces an unmodulated channel r_t which is also crucial in the size of a backscatter network. Thereby, the term "reach" will be used to measure how far a transmitter is placed from the exciter.

With the observed channel product, the combination of both distances gives the range-reach product (or "budget", since it must be adhered to). Equation 2.9[4] showed that the product of range r_r and reach r_t can be calculated using the link budget of the radio system. The following equation 3.5 repeats that expression (eq 2.9[4]):

$$B = r_t \cdot r_r = \sqrt[n]{\left(\frac{\lambda}{4\pi}\right)^4 \frac{P_T}{P_R} G_T^2 G_R^2 |\Gamma_{L,1} - \Gamma_{L,2}|^2} \quad (3.5)$$

where B is the range-reach budget (shortened as Range-Reach Budget (RRB)) and has a unit of m^2 . In the remaining of this chapter, it is assumed that $G_T = G_R = 1$, $\Gamma_{L,1} - \Gamma_{L,2} = 1$, $\lambda = \frac{300}{434}$ and $n = 2$, unless stated otherwise.

Figure 3.7 indicates of representative range-reach budgets for such a radio system. In the parking terrain application, the goal is to create a network with a range of $r_r = 3m$ and a reach of $r_t = 30m$, requiring an RRB of $90m^2$. This means a link budget of $\geq 90dB$ is necessary, which can be realized with a 30dBm exciter and -60dBm sensitive receiver. These are quite rather optimistic sensitivity values for passive receivers, as was found in the literature background.

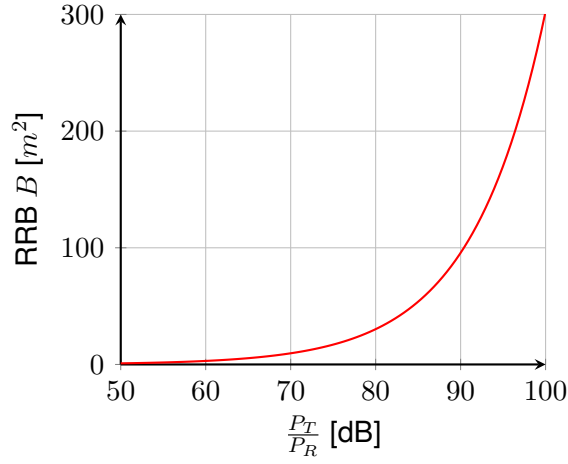


Figure 3.7: Feasible range-reach budgets as a function of link budget

3.5 Range vs Reach Analysis

This section will focus on the maximum reach and range that can be created for a particular carrier configuration. Since the exciter tone at the receiver is not of interest, the channel r_d will be omitted throughout this section.

3.5.1 Monostatic backscatter (single-hop)

Figure 3.8 shows a monostatic backscatter scenario. In this configuration, the exciter transmits a pure tone to the scattering transmitter. The scattered signal from the transmitter is then received by a reader inside the interrogator, which is at the same location as the exciter.

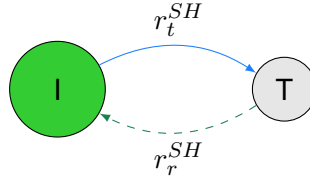


Figure 3.8: Monostatic backscatter or single-hop communication

In this situation, the defined terminology range and reach have little meaning, since the dimensions are $r_t^{SH} = r_r^{SH}$. However, to calculate the maximum value for r_t^{SH}, r_r^{SH} , the range-reach budget will still be used (eq 3.5):

$$r_t^{SH} r_r^{SH} = B \implies r_t^{SH} = \sqrt{B} \quad (3.6)$$

Figure 3.9 shows the distance that can be reached as a function of link budget. Equation 3.5 is substituted into equation 3.6:

$$r_t^{SH} = \sqrt{B} = \sqrt[2n]{\left(\frac{\lambda}{4\pi}\right)^4 \frac{P_T}{P_R} G_T^2 G_R^2 |\Gamma_{L,1} - \Gamma_{L,2}|^2} \quad (3.7)$$

And rewritten assuming $n = 2$:

$$r_t^{SH} = \sqrt{B} = \left(\frac{\lambda}{4\pi}\right) \sqrt{G_T G_R |\Gamma_{L,1} - \Gamma_{L,2}|} \sqrt[4]{\frac{P_T}{P_R}} \quad (3.8)$$

Finally when using the assumptions of antenna gains and ME are all 1, then:

$$r_t^{SH} = \sqrt{B} = \left(\frac{\lambda}{4\pi}\right)^4 \sqrt[4]{\frac{P_T}{P_R}} \quad (3.9)$$

In equation 3.9, it is clearly visible that improvements in $\frac{P_T}{P_R}$ by e.g. +10dB (10x) only results in a factor $\sqrt[4]{10} = 1.78$ improvement in r_t^{SH} .

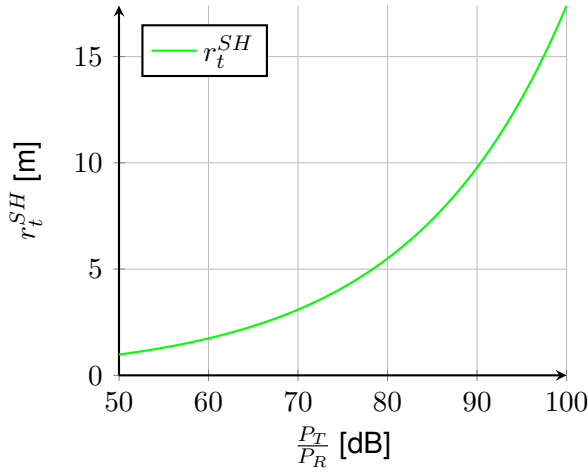


Figure 3.9: Range/reach for a monostatic backscatter system as a function of link budget

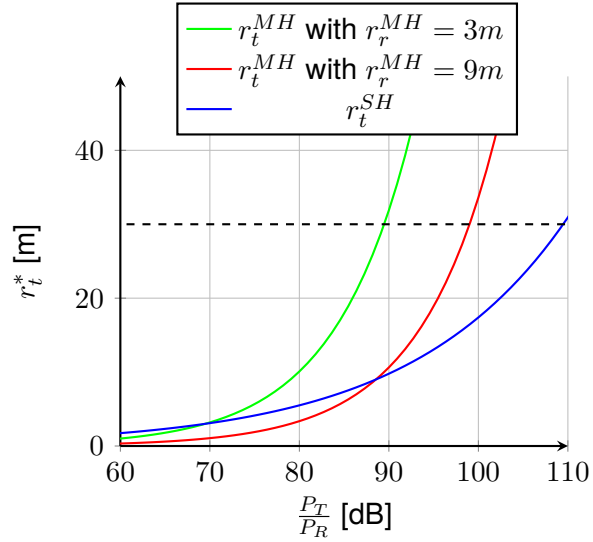


Figure 3.10: In section 3.5.2: Reach for backscatter systems as a function of link budget

3.5.2 Bistatic backscatter (multi-hop)

Figure 3.11 shows an FW and BW backscatter channel, with nodes positioned at the same distances d_1 and d_2 . The only difference then is the reversal of the backscatter communication channel r_r . In this paragraph, a multi-hop analysis is performed for a forward channel (since it is the most favourable), where it will be distinguished as r_t^{MH} , r_r^{MH} and r_d^{MH} .

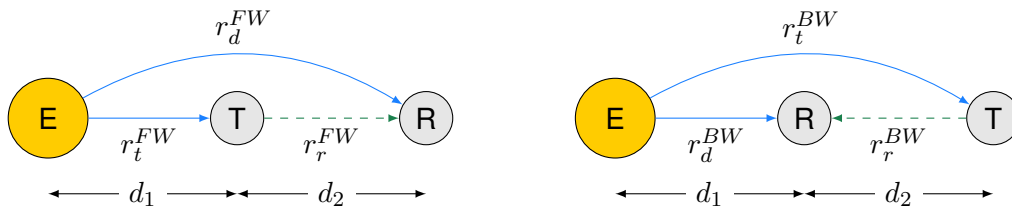


Figure 3.11: Multi-hop backscatter node communication arrangement

This shows that a backwards channel always requires more range-reach budget. Thereby, for backscatter radio to facilitate a generic wireless network, the analysis will remain focus on the backward channel.

Since $B = r_t^{MH} r_r^{MH}$, it follows that $r_t^{MH} = \frac{B}{r_r^{MH}}$ and $r_r^{MH} = \frac{B}{r_t^{MH}}$. In bistatic backscatter, it is possible to vary r_r^{MH} and r_t^{MH} independently, in contrast to monostatic backscatter where $r_t^{SH} = r_r^{SH}$. Then range-reach budget (eq 3.5) is substituted, a more favourable scaling of link budget and range relationship appears:

$$r_t^{MH} = \frac{B}{r_r^{MH}} = \frac{\sqrt[n]{\left(\frac{\lambda}{4\pi}\right)^4 \frac{P_T}{P_R} G_T^2 G_R^2 |\Gamma_{L,1} - \Gamma_{L,2}|^2}}{r_r^{MH}} \quad r_r^{MH} = \frac{B}{r_t^{MH}} = \frac{\sqrt[n]{\left(\frac{\lambda}{4\pi}\right)^4 \frac{P_T}{P_R} G_T^2 G_R^2 |\Gamma_{L,1} - \Gamma_{L,2}|^2}}{r_t^{MH}} \quad (3.10) \quad (3.11)$$

Then when the same assumptions as in the monostatic backscatter calculation are applied ($n = 2$, $G_T = G_R = 1$ and $ME=1$), then:

$$r_t^{MH} = \frac{B}{r_r^{MH}} = \left(\frac{\lambda}{4\pi}\right)^2 \frac{\sqrt{\frac{P_T}{P_R}}}{r_r^{MH}} \quad (3.12) \quad r_r^{MH} = \frac{B}{r_t^{MH}} = \left(\frac{\lambda}{4\pi}\right)^2 \frac{\sqrt{\frac{P_T}{P_R}}}{r_t^{MH}} \quad (3.13)$$

Compared to the result of monostatic backscatter in equation 3.9, it shows a far more favourable dependency on the link budget: a $\sqrt[4]{\cdot}$ has been replaced by $\sqrt[2]{\cdot}$. Although both formulations also show an extra $\frac{\lambda}{4\pi}$ factor, it is reasonable to expect that $\sqrt{\frac{P_T}{P_R}} \gg \frac{\lambda}{4\pi}$.

Figure 3.10 shows the (potential) range of a multi-hop compared to single-hop. The maximum reach r_t^{MH} is plotted against a chosen r_r^{MH} of 3 or 9 meters. The dashed line indicates the goal reach of 30m. The single-hop trace is the same as from figure 3.9.

The intersection between r_t^{SH} and r_t^{MH} occurs at the point where the achievable range of r_r^{SH} becomes equal to r_r^{MH} . This means that multi-hop backscatter can give a reach improvement (r_t^{MH}), but only under the condition that for the given link budget a single-hop link is also able to sustain the range of r_r^{MH} . Namely, $r_t^{SH} < r_t^{MH}$ can only occur if and only if $r_r^{SH} > r_r^{MH}$, where $r_t^{SH} = r_r^{SH}$ and the same range-reach budget: $r_t^{SH} r_r^{SH} = r_t^{MH} r_r^{MH} = B\left(\frac{P_T}{P_R}\right)$.

The graph shows that multi-hop can be used to increase the reach of a backscatter WSN, however, it must be assured that relatively high link budgets are available. For 3m hop distance to be beneficial, at least 70dB link budget is required. However, the reach scales far faster in multi-hop than in single-hop. To achieve 30m reach with multi-hop using $r_r^{MH} = 3m$, around 90dB link budget is required. Single-hop would require around 110dB, which is 20dB more.

3.6 Node Positioning

Having established that multi-hop can provide either a range or reach improvement over single-hop, this section will relate the positioning of nodes to the range-reach budget of equation 3.5.

3.6.1 Definitions

Figure 3.11 shows an FW and BW bistatic backscatter channel that can be used to realize a wireless network. In a BW channel, d_1 represents the exciter-receiver distance and d_2 the transmitter-receiver distance.

The following formulations are defined for the reach r_t , the range r_r and exciter incident signal r_d using d_1 and d_2 , in both FW and BW configurations:

$$r_r^{FW} = d_2 \quad (3.14) \quad r_r^{BW} = d_2 \quad (3.17)$$

$$r_t^{FW} = d_1 \quad (3.15) \quad r_t^{BW} = d_1 + d_2 \quad (3.18)$$

$$r_d^{FW} = r_t + r_r = d_1 + d_2 \quad (3.16) \quad r_d^{BW} = r_t - r_r = d_1 \quad (3.19)$$

Using these formulations, it is possible to show that a BW channel always requires more range-reach budget than a forward channel:

$$r_t^{BW} r_r^{BW} \geq r_t^{FW} r_r^{FW} \quad (3.20)$$

$$(d_1 + d_2)d_2 \geq d_1 d_2 \quad (3.21)$$

Which is always true when $d_1 > 0$ and $d_2 > 0$. Using this remark, the remaining of this section will analyze the BW channel since it gives a more pessimistic expectation on the realizable distances in a backscatter network.

3.6.2 Exciter-receiver distance d_1

The reach in a BW channel is defined as $r_t^{BW} = d_1 + d_2$, which means that d_1 is not a direct representation of the reach. However, for fixed values of d_2 , then d_1 will need to be used such that the reach can be maximized.

From the formulations, the following equation needs to be solved for d_1 :

$$B = (d_1 + d_2)d_2 = d_1 d_2 + d_2^2 \quad (3.22)$$

Which is equal to:

$$d_1 = \frac{B}{d_2} - d_2 \quad (3.23)$$

For example, if a tag-to-tag distance of $d_2 = 3$ meters is required while $B = 30m^2$, then the maximum value of d_1 is $\frac{30}{3} - 3 = 7m$. The reach is then $d_1 + d_2 = 10m$.

The formula also shows that large values of d_1 can be accomplished by increasing the range-reach budget B , or by decreasing the tag-to-tag distance d_2 (range). For example, if $B = 60m^2$ with $d_2 = 3m$, then $d_1 = \frac{60}{3} - 3 = 17m$ with a reach of $d_1 + d_2 = 20m$. This behaviour shows that the exciter-receiver distance d_1 can scale faster than the factor 2 improvement in the RRB.

3.6.3 Transmitter-receiver distance d_2

The maximum tag-to-tag distance d_2 is dependent on the range-reach budget B and d_1 . Again using the range-reach budget formula for the BW channel:

$$B = (d_1 + d_2)d_2 = d_1 d_2 + d_2^2 \quad (3.24)$$

Which can be rewritten into:

$$d_2^2 + d_1 d_2 - B = 0 \quad (3.25)$$

Solved for d_2 (using the quadratic formula):

$$d_2 = \frac{\sqrt{d_1^2 + 4B} - d_1}{2} \quad (3.26)$$

Then, for a range-reach budget of $B = 30m^2$ and a maximum exciter-receiver distance d_1 of 7m, then $d_2 = 3m$. It is important to note that d_2 does not increase that quickly with B in a BW channel, due to the value d_2 being proportional to the square root of B . For example, when $B = 60m^2$ and $d_1 = 7m$, then d_2 increases to only 5m.

3.7 Modulation Index

The modulation index is an interesting property in backscatter systems, as it depends on the node locations and the contributing incident power of the exciter and scattering transmitter in its definition. This section aims to characterize the minimum modulation index that an ASK backscatter receiver may observe, as a function of node positions or the range-reach budget.

3.7.1 Definition

The range-reach model is based on using transmit power and receive sensitivity only. However, from the background study (equation 2.6), the modulation index was found to be[29]:

$$m(r_r) = \frac{1}{1 + h(r_r)} \text{ with } h(r_r) = 2 \cdot \frac{4\pi r_r}{G\lambda} \sqrt{\frac{P_{RX}}{P_{TX}}} \quad (3.27)$$

It is assumed that G represents antenna gain(s) to simplify the initial modelling of the modulation index. Here the formulations of the incident powers at the receiver P_{RX} and transmitter P_{TX} can be added accordingly:

$$P_{TX}(r_t) = P_E L(r_t) = P_E \left(\frac{\lambda}{4\pi}\right)^2 \frac{1}{r_t^n} \quad (3.28) \quad P_{RX}(r_d) = P_E L(r_d) = P_E \left(\frac{\lambda}{4\pi}\right)^2 \frac{1}{r_d^n} \quad (3.29)$$

where P_E is the power transmitted by the exciter.

Since the power available at the receiver and transmitter is dependent on the channel lengths r_t , r_r and r_d , it is possible to find a lower bound on the modulation index for a forward and backward channel. The loss equations in equations 3.28 and 3.29 are substituted into equation 3.27:

$$m'(r_t, r_r, r_d) = \frac{1}{1 + h'(r_t, r_r, r_d)} \text{ with } h'(r_t, r_r, r_d) = 2 \cdot \frac{4\pi r_r}{G\lambda} \sqrt{\frac{r_t^n}{r_d^n}} =_{|n=2} \frac{8\pi}{G\lambda} \frac{r_r r_t}{r_d} \quad (3.30)$$

Where $m'(r_t, r_r, r_d)$ and $h'(r_t, r_r, r_d)$ express the modulation index as a function of the reach r_t , range r_r and exciter-receiver distance r_d .

3.7.2 Minimum index in forward channel

Using the formulations for an FW channel given in paragraph 3.6, the modulation index for an FW channel can be expressed using r_t^{FW} , r_r^{FW} and r_d^{FW} with equation 3.30:

$$m^{FW}(d_1, d_2) = \frac{1}{1 + \frac{8\pi}{G\lambda} \frac{d_1 d_2}{d_1 + d_2}} \quad (3.31)$$

To find the worst positioning of d_1 and d_2 w.r.t. the modulation index, the following equation needs to be solved:

$$\min_{d_1, d_2} m^{FW}(d_1, d_2) = \min_{d_1, d_2} \frac{1}{1 + \frac{8\pi}{G\lambda} \frac{d_1 d_2}{d_1 + d_2}} \quad (3.32)$$

which, when optimizing only d_1 and d_2 , means that the solution needs to be found for:

$$\max_{d_1, d_2} \frac{d_1 d_2}{d_1 + d_2} \quad (3.33)$$

The maximum ratio can be found when $d_1 = d_2$. It has previously been observed that the worst position (in terms of signal strength) for the transmitter is the middle of the channel. To find

a solution for d_1 and d_2 while subject to $d_1 d_2 = B$, then $d_1 = d_2 = \sqrt{B}$, such that $d_1 + d_2 = 2\sqrt{B}$ and:

$$\max_{d_1, d_2} \frac{d_1 d_2}{d_1 + d_2} = \frac{B}{\sqrt{B} + \sqrt{B}} = \frac{\sqrt{B}}{2} \quad (3.34)$$

The result in equation 3.34 is substituted into equation 3.31:

$$M^{FW}(B) = \frac{1}{1 + \frac{4\pi\sqrt{B}}{G\lambda}} \quad (3.35)$$

Where $M^{FW}(B)$ expresses the minimum modulation index in an FW channel as a function of range-reach budget B .

Equation 3.35 shows that the minimum modulation index in an FW channel is a function of the range-reach budget. As an example, if $B = 30m^2$, $G = 1$ and $\lambda = \frac{300}{434}$, then the minimum modulation index is 0.99%.

3.7.3 Minimum index in backward channel

The minimum index in a backward channel needs additional boundaries to create a practical lower bound. Namely, from equation 3.30, it can be seen that the lowest theoretical modulation index is reached when $r_d = 0$, i.e. when the tag is located at the position of the exciter:

$$\lim_{r_d \rightarrow 0} m'(r_t, r_r, r_d) = 0 \quad (3.36)$$

However, in a practical WSN it is that r_d will have a lower bound due to the placement of tags. When it is that $r_d = s$, where s is the minimum excite-receiver distance, then it is possible to find a more usable minimum.

Using the formulations for a BW channel given in paragraph 3.6, the modulation index for a BW channel can be expressed using r_t^{BW} , r_r^{BW} and r_d^{BW} with equation 3.30:

$$m^{BW}(d_1, d_2) = \frac{1}{1 + \frac{8\pi r_t r_r}{G\lambda r_d}} = \frac{1}{1 + \frac{8\pi(d_1 + d_2)d_2}{G\lambda d_1}} \quad (3.37)$$

Where again the minimum modulation must be found:

$$\min_{d_1, d_2} m^{BW}(d_1, d_2) \quad (3.38)$$

As by definition of equation 3.5 it is that $r_t r_r = B$, the following result can be found for the minimum modulation index of a BW channel:

$$M^{BW}(B, s) = \frac{1}{1 + \frac{8\pi r_t r_r}{G\lambda r_d}} = \frac{1}{1 + \frac{8\pi B}{G\lambda s}} \quad (3.39)$$

Where $M^{BW}(B, s)$ expresses the minimum modulation index in a BW channel as a function of range-reach budget B and minimum exciter-receiver distance s . As an example, if $B=90m^2$, $G = 1$ and $s = 2\lambda = 2\frac{300}{434} = 1.38m$, then the minimum modulation index is only 0.0422% (422ppm). However, for the parking systems, it is more likely that s is in the order of 3m. Thereby with $B=90m^2$ and $s = 3m$, the minimum modulation index of a backward channel is 0.092% (920ppm).

3.7.4 Comparison

Figure 3.12 and 3.13 show the modulation index as a function of d_1 and d_2 respectively.

From figure 3.12 it is visible that the modulation index in a forward channel is always greater than that in an identically placed backward channel. In particular near the exciter, the backward channel suffers far more than a forward channel.

In addition, figure 3.14 shows the large difference in minimum modulation index for both channel configurations. Again, the graph highlights that for $s = 2\lambda$ an unrealistically low modulation index is calculated for larger range-reach budgets. For a minimum reach of 3m, then a minimum modulation index of about 0.04% is to be expected.

This value is still incredibly low. For example, Karimi et al. [29] demonstrated an ASK receiver design that was able to function at modulation indices of 0.6%. The design, however, was demonstrated using symmetric channels, which did not show the worst-case tag arrangement possible in a network.

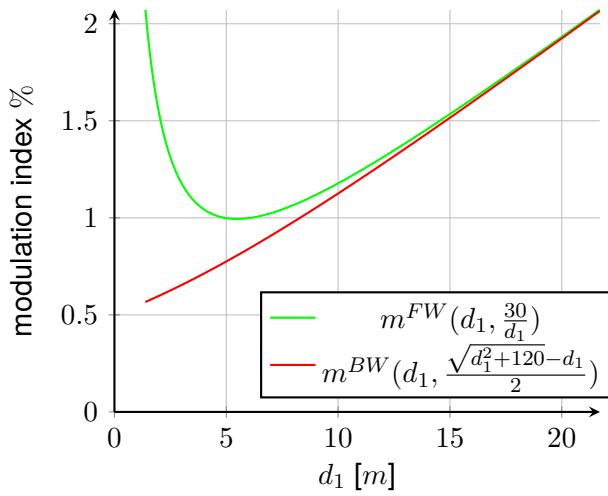


Figure 3.12: Modulation index for values of d_1 in domain $(2\lambda, \frac{B}{2\lambda})$ ($B = 30m^2$).

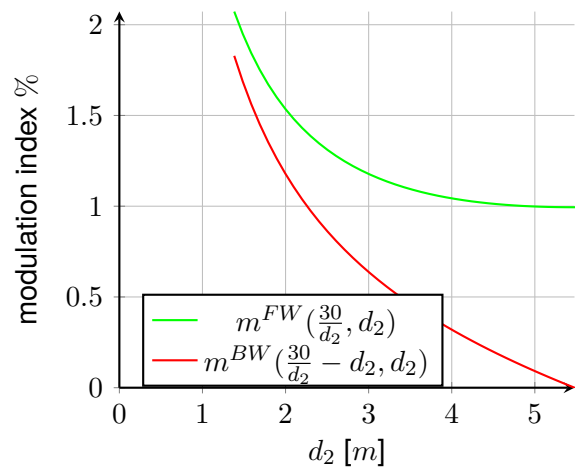


Figure 3.13: Modulation index for values of d_2 ($B = 30m^2$)

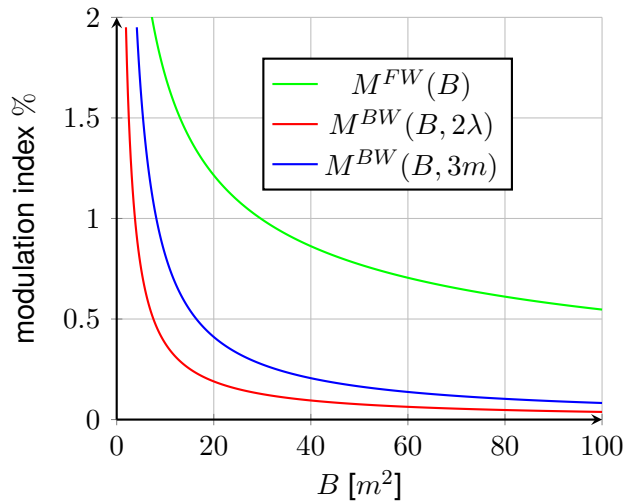


Figure 3.14: Minimum modulation index as a function of B

4 | Node Design

This chapter will perform a design space exploration on the components that can be used to build an energy efficient backscatter sensor node. The final section will display the block diagram of the board schematic of this node.

4.1 Node System Architecture

The top-level block diagram of an energy harvesting wireless sensor node is shown in figure 4.1. The functions are described in the upcoming paragraphs.

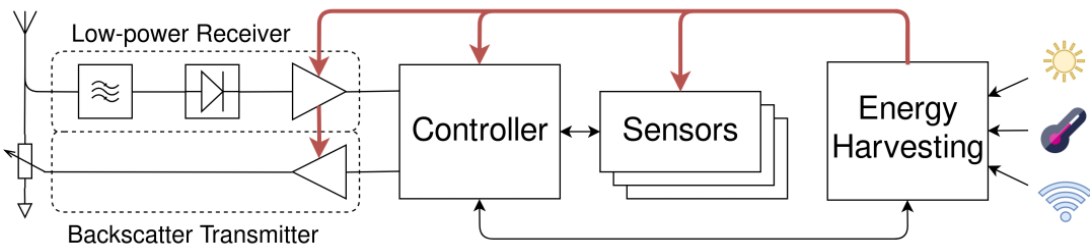


Figure 4.1: A perpetual wireless sensor node with energy harvesters and backscatter radio

A duplex radio is needed for tag-to-tag communication. The radio consists of a backscatter transmitter that will be used to send data with the help of the exciter’s carrier tone. A receiver tailored towards backscatter and low power will be used to receive symbols from other nodes.

The controller will need to perform the translation between (digital) symbols and data packets. These packets form the basis of typical protocol stacks. Conventional radios focused at sub-GHz IoT networking have a packet buffer size between 64 and 128 bytes[53], [54].

The sensors used are application specific and have a big influence on design decisions in for example firmware (e.g. sampling interval, processing, etc.). The goal of this thesis is to investigate and improve backscatter radio. As a proof of concept, a temperature and humidity sensor is going to be used.

Although energy harvesting and management is an essential part of perpetual wireless sensor networks, this thesis will focus on improving range and/or decreasing the power consumption of the backscatter radio.

A hypothetical infinite energy source will be implemented using a standard CR2032 Lithium battery. The power and energy measurements will indicate of the energy harvester requirements.

4.2 Design Space Exploration

This section will offer several design space options to implement the various components as shown in the system diagram of figure 4.1.

4.2.1 Backscatter transceiver (analog)

The backscatter transceiver allows for tag-to-tag communication while targeting link budgets of at least 70dB as shown in chapter 3. However, figure 3.10 also shows that for a reach of up to

20m, a link budget of at least 85dB is necessary. Thereby, if the backscatter transceivers are paired with an exciter of 30dBm, then a receiver with -55dBm sensitivity is required.

To build an experiment with backscatter tags to characterize the range-reach budget, a discrete low-power ASK receiver will be required. At the time of writing this thesis, there were no off-the-shelf designs available for this task. The receiver will be designed in conjunction with the backscatter transmitter.

Non-coherent type receivers based on diode detectors are primarily built when the aim is a low power receiver with compromised sensitivity, as diode detectors omit the need for active components such as mixers and VCO's. The non-coherent property restricts the modulation types to non-constant envelope based approaches, such as ASK modulation. This will also be the chosen modulation for this backscatter tag-to-tag communication.

The input of the analog transceiver section is digital (to control the RF switch). The output of the receiver is a digital signal created with a comparator. The use of a comparator omits the need for A/D converters, as those add additional power consumption to the system design. However, the performance may be constrained by noise, in-band interferers and signal amplitude, however, this will be discussed in more detail in chapter 6.

4.2.1.1 Transmitter

The backscatter impedance modulation that is shown in figure 4.1 suggests that a variable impedance is used. The choice of impedances has 2 axes of freedom: namely resistance and reactance. In equation 3.5 it was shown that the range-reach budget is proportional to the magnitude of the reflection coefficient difference. To build the most effective transmitter, the magnitude of $\Delta\Gamma_{L,i}$ must be maximized.

Daskalakis et al.[16] has shown a backscatter modulator that can accomplish a variable impedance by using an RF field effect transistor and 5-bit DAC. This design, however, requires an active DAC, introducing additional complexity and power consumption.

Thereby a programmable load impedance will be realized using an RF switch between the antenna and an array of impedances. The ME is maximized when $\Gamma_{L,1} = 1$ and $\Gamma_{L,2} = -1$ is chosen (short and open circuit). To combat phase cancellation, the complex reflection coefficients $\Gamma_{L,1} = j$ and $\Gamma_{L,2} = -j$ will also be needed using a matched inductor and capacitor load respectively. This requires at least a 4-load RF switch to facilitate the scattering pairs $\Gamma_{L,A} = (1, -1)$ and $\Gamma_{L,B} = (j, -j)$.

However, as the receiver will also need to be connected to the antenna, which typically will have a 50Ω impedance, it is necessary for the RF switch to create a bypass connection such that the receiver can become active.

4.2.1.2 Receiver

The goal of the low power receiver is to receive ASK symbols that are modulated on top of the strong exciter incident signal. This causes the modulation index to be very low ($\ll 1\%$) as shown in chapter 3.

As suggested, a non-coherent diode detector receiver architecture can be used to realize a low power receiver. Many existing backscatter implementations have looked at "passive" receivers, where there is no active amplification of the received signal. These receivers are very low power ($< 1\mu\text{W}$ [5]), however, do not have outstanding sensitivity to create sufficient range (order of -45dBm).

The sensitivity can be improved by adding gain into the receiver path, as was shown by Karimi et al.[29]. The choices and effects on the pass-band characteristic will be discussed in chapter 6. The output of the receiver chain is a digital output,

4.2.2 Power Management

All components will be powered from a single supply voltage of 1.8V. When powered from a 3V source (Lithium CR2032 coin cell), a linear regulator will dissipate approximately $3 - 1.8 = 1.2V$ times the load current, as it performs constant-current regulation. Thereby only 60% of the consumed power is used to perform work.

A switched-mode regulator can perform this conversion with up to 90% efficiency. For this design, the TPS62740[55] switching buck regulator has been chosen, due to its 90%+ efficiency, but most importantly it's very low quiescent current of $0.36\mu A$. Thereby a high efficiency is realized even for the low loads since the part has a static dissipation of roughly $1\mu W$.

The receiver will be powered through a power switch since it will consume a large portion (up to $36\mu W$) of the power budget. The TPS22917[56] load switch will be used, as it has a quiescent current of 10nA. The transmitter RF switch and sensor are not controlled via a load switch since all of these components have satisfactory quiescent currents of 50 to 100 nA.

4.2.3 Backscatter transceiver (digital) & Controller

The low power consumption of a backscatter transmitter and receiver design puts extra emphasis on efficient digital processing. Off-the-shelf WSN sensors are typically built using a combination of a radio ASIC and microcontroller. The radio ASIC handles the RF and base-band processing functions and integrates a preamble detector, packet/framing engine and even built-in CRC checks. The microcontroller can then access the radio registers over a serial bus to receive or transmit packets. The bitrate of these radio chipsets for IoT is often relatively low ($<1Mbps$).

A microcontroller is well suited to the task of wireless sensor networks, because the radio protocol stack is a large portion of the node's responsibilities, and often customized to suit the application. Protocol stacks also rely heavily on control flow.

In addition, static power consumption is also a crucial criterion for battery operation. FPGAs and CPLDs are outclassed in static power consumption by microcontrollers. The IGLOO nano series from MicroSemi is a series of small FPGAs (100 to 3000 logic elements) with 2 to $24\mu W$ power in freeze mode, respectively[57].

A search among other FPGA vendors (Intel, Xilinx and LatticeSemi) did not yield any results with lower power FPGAs. In contrast, modern microcontrollers typically consume 1 to $2\mu W$ of static power in sleep (with RAM retention and RTC running)[38]–[44].

4.2.3.1 Interfacing with RF transceiver

The output of the receiver is a digital output created by a comparator. The backscatter transmitter requires several digital lines that select the correct load impedance on the antenna. The microcontroller should measure or create these timed signals for communication.

Microcontrollers contain (multiple) hardware timers which can be used for this purpose. In case of transmitting, it is possible to create a variant of pulse-width modulation (PWM) such that different symbols can be transmitted that vary in pulse width (such as in FM0 encoding). The

PWM can typically be created using the timers programmable time base and compare registers, which set the pulse width of the output waveform.

The received could be sampled with a fixed period, and then iterated through a software algorithm that measures the high/low pulse widths for each symbol. However, most microcontroller timers also have the capability of a capture input, which allows for hardware-based measurements of the signal high and low pulse widths.

Virtually all modern microcontrollers have the aforementioned capture & compare functionality built into their timer peripherals. Some microcontrollers allow the combination of a sequence of timer capture or compare events and DMA to even further offload the data transmission & reception into hardware. Then the CPU is only responsible for encoding or decoding a set of symbols from the hardware.

4.2.3.2 Part Survey Methods

To narrow down the large selection of available microcontrollers, the EEMBC ULPmark[58] benchmark has been used as a basis for this survey. EEMBC designs processor benchmarks for embedded applications. The ULPmark focuses on low power/energy consumption of processor plus peripherals, and has 3 different suites[58]:

- **ULPmark-CP** The Core Profile quantifies the efficiency of duty cycling the processor between active and sleep periods (including overhead from wake-up latency and peak power), as well as the efficiency for short computational bursts. Note that "idle", where oscillators are active but the CPU is clock gated off, is not used in this benchmark.
- **ULPmark-CM** The CoreMark profile measures the execution efficiency (performance per Watt or Joule) of the processor. The standard "CoreMark" suite (a set of tasks that exercises a fixed workload) is run several times, while the energy consumption for those executions is measured.
- **ULPmark-PP** The Peripheral Profile measures the peripheral consumption in the absence of the processor by using the idle mode of the processor. The microcontroller ADC, timer, SPI and RTC peripherals are used with a low (32.768kHz) and high (≥ 16 MHz) clock frequency. This benchmark contains 10 tests that are combined to a single score.

Any low power/energy application can be a combination of all 3 tests, with some applications having a stronger dependence for 1 test than others. In the case of the low-power sensor node, the following requirements have been identified:

- The ULPmark-CP primarily quantifies the sleep power consumption and wake-up overhead. This will not be a good indicator of performance in this application. In active radio operation, the processor cannot be duty cycled into sleep because a "high-frequency" (HF) oscillator is required for receiving symbols (timer pulse measurement, DMA). Most microcontrollers require the system to stay in idle operation to keep an HF oscillator running. Some microcontrollers offer low-power timers that can operate at the low-frequency clock domain (32.768kHz), however, these cannot be used in conjunction with DMA.
- The (initial) processing requirements are relatively low due to the bitrate and simple algorithms. Although a good ULPmark-CM score will contribute to efficiency, it is expected to be a relatively small contributor to the overall energy consumption.

- Thereby the high duty cycle of the high-frequency oscillator is expressed in the ULPmark-PP benchmark, making this the primary benchmark to select controllers on.

Table 4.1 enumerates several low power microcontrollers found sorted on the ULPmark-PP benchmark score (higher is better)[59]. The score is calculated as $ULPmark_{PP} = \frac{10000}{E_{consumed}}$, where $E_{consumed}$ is the total number of μJ consumed for all 10 tests.

The columns list for each microcontroller it's CPU core architecture, the ULPmark CP and PP scores, along with the available amount of memory (FLASH and RAM) and power consumption (in μW) for different power modes. Bold-faced figures are interpolated using a linear model $P_{fig}(f) = P_{dynamic} \cdot f + P_{static}$ which is based on higher-clocked consumption figures from the datasheets. Although the power consumption for microcontrollers is rarely linear over the whole range of clock configurations (e.g. from 32kHz up to 80MHz), however within the same range (e.g. 1 vs 4MHz from same oscillator source) is typically fairly linear, and thereby a reasonable approximation.

4.2.3.3 Part Investigation

The ATXMEGA32E5[44] and MSP430FR5969[43] are popular in academic literature due to their accessible programming tools, learning environment support and excellent documentation. However, as can be observed from the raw benchmark scores, their power consumption efficiency is not the best. These controllers often rely on vendor-specific peripheral event systems such that the microcontroller peripherals can perform more complex tasks while the CPU remains in deep(er) sleep modes.

The APOLLO2[42] boasts excellent $\mu\text{A}/\text{MHz}$ at maximum clock frequency, yielding an excellent ULPmark-CP score. However, the quiescent current of the oscillator is relatively high, contributing to a low ULPmark-PP score.

The STM32L011[41] does not feature a very strong ULPmark-PP score, due to the relatively high power consumption of the internal 32.768kHz oscillator ($0.4 \mu\text{A}$). The power consumption of the high-speed oscillator is $0.6 \mu\text{A}$ at 131kHz and $4.5 \mu\text{A}$ at 1.05MHz[41].

From the consumption figures, the STM32L431[40] compares close to the STM32L412[38] part: however the PP benchmark scores are significantly different. This is presumably because of the largely different testing conditions and supply voltage. Based on the datasheets of both parts, their power consumption figures are almost identical. Therefore the STM32L431 has been chosen due to the richer peripheral set and significantly more memory.

The ATSAML11E16A[39] ULPmark-PP score was published on 1 March 2019, which is 2 months after the choice for the STM32L431 part had been made. The ULPmark-PP subscores suggest this part could be an even better choice because the subscore for test 9 (which uses a high-frequency oscillator for timers) was almost two times better than the STM32L412 ($29 \mu\text{J}$ STM32L412 vs $17.1 \mu\text{J}$ ATSAML11E16A).

4.2.3.4 Power optimization & estimation

There are several optimizations which can be utilized to further improve the energy efficiency of the system. The timer is used to digitize the square wave output of the ASK receiver (pulse width measurement). The digitized pulses will be moved to SRAM using DMA such that the CPU can remain off for these transfers.

The high-frequency oscillator must remain active continuously for the timer to operate. To minimize the active consumption, the oscillator is set at the lowest frequency possible of 100kHz.

Part	Core	CP	PP	FLASH	RAM	Active	Idle	Sleep
STM32L412[38]	Cortex M4F	247	167	128kB	40kB	198	66	0.5
ATSAML11E16A[39]	Cortex M23	280	167	64kB	16kB	214	121	2.3
STM32L431[40]	Cortex M4F	253	121	256kB	64kB	203	70	0.5
STM32L011[41]	Cortex M0+	161	82.9	16kB	2kB	248	83	0.97
APOLLO2[42]	Cortex M4F	377	54.8	512kB	64kB	239	103	0.94
MSP430FR5969[43]	MSP430	124	n/a	64kB	2kB	220	77	0.88
ATXMEGA32E5[44]	AVR	80	n/a	32kB	4kB	279	99	1

Table 4.1: Comparison of microcontrollers[38]–[44]. Columns active, idle and sleep figures are in μW , with $f_{cpu} = f_{sys} = 1\text{MHz}$ for active and $f_{cpu} = 0\text{Hz}$, $f_{sys} = 1\text{MHz}$ for idle.

The power consumption of FLASH is relatively high. The program could also be run from SRAM such that the FLASH can be turned off. This optimization is possible on all processors except for the ATXMEGA32E5, as this processor is a Harvard architecture. The other microprocessors are a modified Harvard machine, where the instruction memory bus can access the SRAM memory through the AHB cross-bar.

The STM32CubeMX design tool[60] has been used to extract a design-time power consumption estimate of the microcontroller. The overall system consumption can be estimated when combined with the RF transceiver power consumption and buck regulator efficiency. It is estimated using that the active and idle power consumption of the microcontroller is 43 and $24\mu\text{W}$ respectively.

5 | Backscatter Transmitter

This chapter will discuss the design and unique problems found in backscatter radio. First, the basic concept of amplitude and phase modulation is described using load impedances. Then, the aliasing of the modulated signal with the exciter is described, to explain how PSK modulation can be used with an ASK receiver in backscatter. The aliasing is then used to repeat the background of phase cancellation, and why a tag-to-tag radio must be equipped with countermeasures.

5.1 Backscatter Modulation

5.1.1 Amplitude and phase modulation

Figure 5.1 shows the Smith chart of amplitude modulation. The chart contains 2 impedances $Z_{L,i}$, where 1 is matched to the antenna impedance Z_A ($Z_{L,1} = Z_A, \Gamma_{L,1} = 0$) and one is unmatched with a short circuit ($Z_{L,2} = 0\Omega, \Gamma_{L,2} = -1$).

When $\Gamma_{L,1} = -1$ and $\Gamma_{L,2} = 1$ (or with complex impedances, $\Gamma_{L,1} = j$ and $\Gamma_{L,2} = -j$) is used, then a BPSK modulation output is created. This is shown in figure 5.2. The use of this modulation pair is attractive since the ME is 4 (modulation efficiency), which should result in a more effective scattering.

Figure 5.3 shows a QPSK modulation system. Jumping from $\Gamma_{L,i} = -1$ to $\Gamma_{L,i} = \pm j$ will result in a 90-degree phase shift of the reflected incident wave since the mismatch transitions from a resistive ($Z_L = 0, \Gamma_{L,i} = -1$) to an inductive ($\Gamma_{L,i} = j$) or capacitive ($\Gamma_{L,i} = -j$) state. Since 4 of these points can be defined with a 90-degree difference of each other, a QPSK constellation can be created. However, the ME in the QPSK example is only 2.

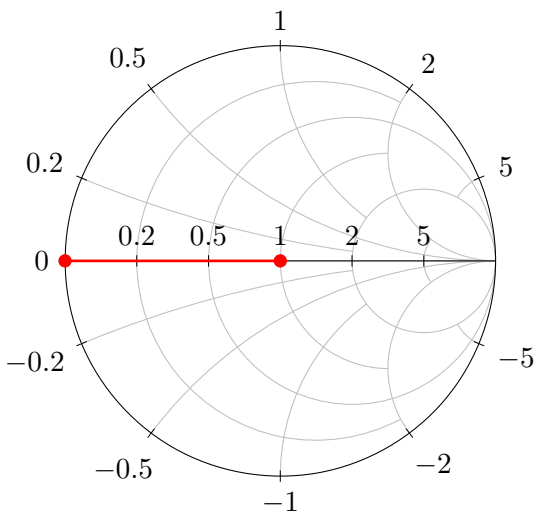


Figure 5.1: Example of an ASK modulation pair with ME=1.

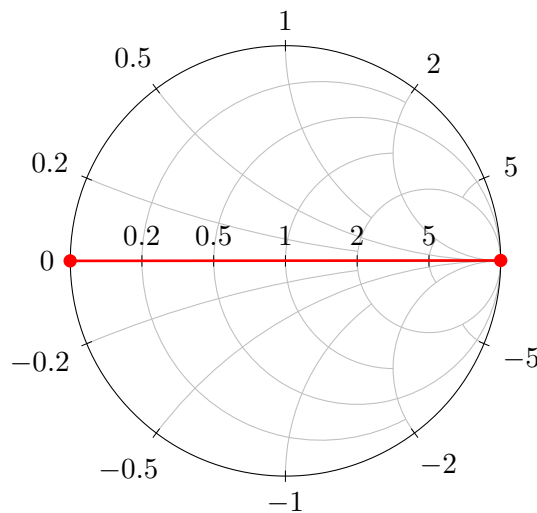


Figure 5.2: Example of a BPSK modulation pair with ME=4.

5.1.2 Aliasing of BPSK modulation

The receiver sees a combination (superposition) of the exciter and the scattered signal. In ASK modulation, a non-constant envelope signal is scattered back to the receiver which intuitively

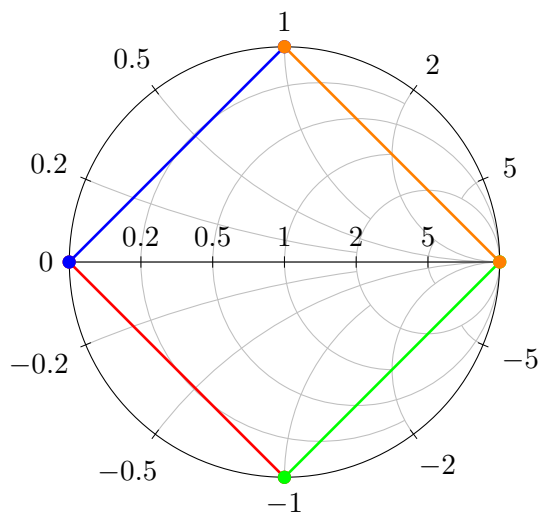


Figure 5.3: 1 constellation of QPSK

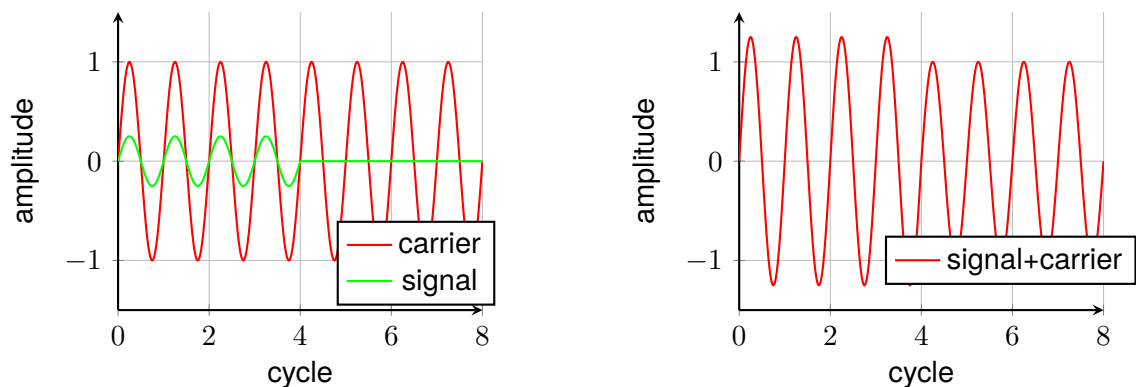


Figure 5.4: Example of a carrier and reflected signal using ASK modulation. Left shows the individual signals, right shows the addition of them at a receiver

can be detected. In BPSK, the receiver normally observes a constant envelope signal, where the signal is in phase or out of phase with the carrier.

However in conventional radio, typically carrier suppression is performed. The reasons are twofold: first, the PA of the transmitter should not waste power on transmitting the carrier tone which contains no information. Secondly, the carrier can be seen as a large in-band interference.

Figure 5.4 and 5.5 show the ASK and BPSK modulations (green) in combination with the exciter tone (red). In ASK, the signal is scattered in-phase, resulting in an addition of the waves' amplitudes at the receiver. After cycle 4 a matched impedance is connected, reducing the scattered signal to zero, thereby leaving only the carrier signal at the receiver.

In the BPSK example, the same situation occurs in cycle 0 to 4. After that, the signal is scattered completely out-of-phase. This results in subtraction of both amplitudes at the receiver. The receiver observes a twice as big amplitude difference. This process makes BPSK modulation usable even with ASK receivers.

5.1.3 Phase cancellation

The previous section assumed that the signals are either perfectly in-phase or out of phase. However, phase shifts may be introduced at various places, such as a transmission line or time of flight in the communication channel.

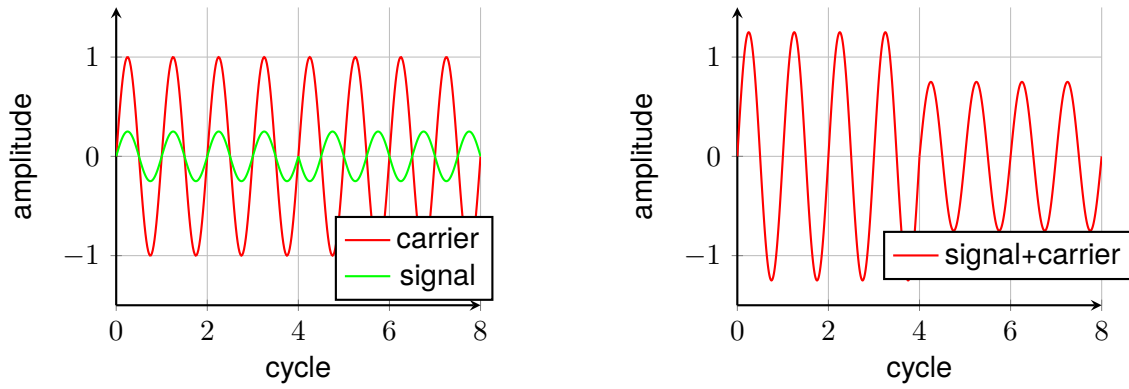


Figure 5.5: Example of a carrier and reflected signal using BPSK modulation. Left shows the individual signals, right shows the addition of them at a receiver

This arbitrary phase offset can result in a complete cancellation of the exciter and scattered wave. An example would be when the signal is offset by $\frac{\pi}{2}$, leading to the addition of sine and cosine, where intuitively $\cos^2(x) + \sin^2(x) = 1$. The observable amplitude and phase change observable is almost negligible.

Figures 5.6 and 5.7 shows this effect for ASK and BPSK modulation respectively. In this case, the scattered signal has been changed from a sine to a cosine function, effectively introducing a $\frac{\pi}{2}$ phase shift. This problem is called phase cancellation in the literature.

To mitigate these effects, the channel properties must be known such that any backscattering can be performed using either a modulation pair that scatters in-phase or as a quadrature variant[19]. Shen et al.[20] showed mathematically that the phase shift of $\frac{\pi}{2}$ is most effective at reducing the effects of phase cancellation.

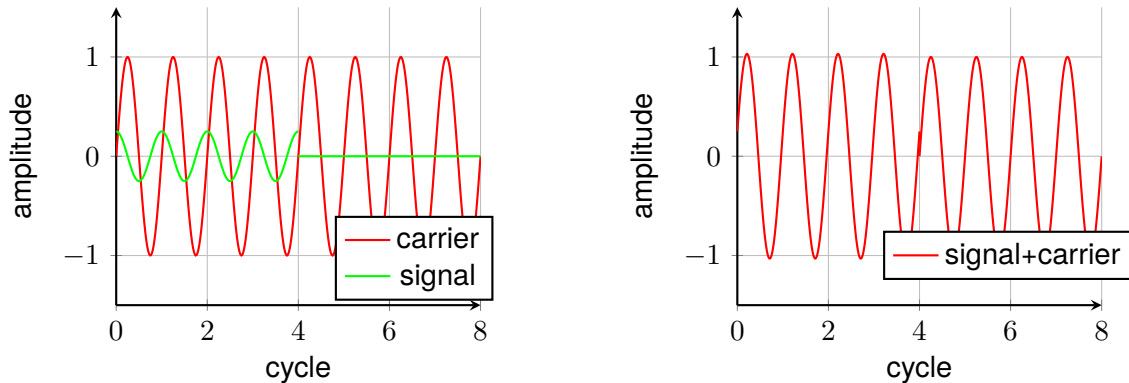


Figure 5.6: Phase cancellation with ASK modulation. Here a sine-wave exciter and cosine scattered signal are added, resulting in almost complete cancellation.

5.2 Transmitter Design

Figure 5.8 shows the Smith chart of the transmitter. The transmitter will be realized with a multi-pole switch, which can connect the antenna to different load impedances, as is depicted in figure 5.9. The red line indicates the scattering pair $\Gamma_{L,A}$, and blue the scattering pair $\Gamma_{L,B}$. The green dot indicates the switch connected to the receiver.

The required load impedance can be calculated using[13]:

$$Z_{L,i} = Z_a \frac{1 + \Gamma}{1 - \Gamma} \quad (5.1)$$

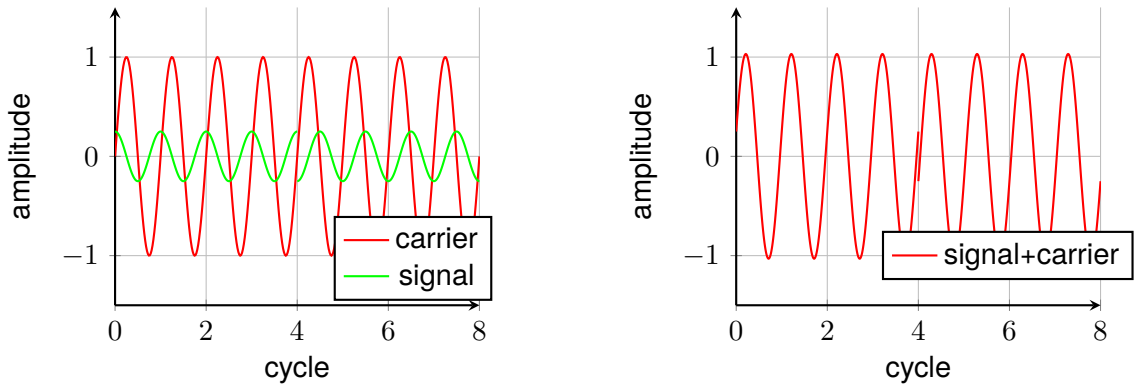


Figure 5.7: Phase cancellation with BPSK modulation. Here a sine-wave exciter and cosine scattered signal are added, resulting in almost complete cancellation.

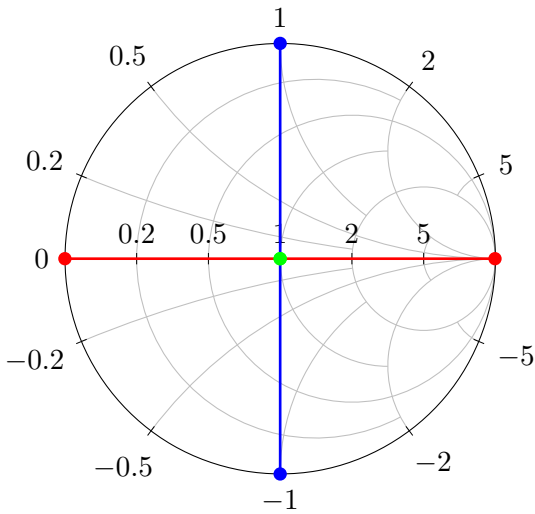


Figure 5.8: 2 scattering pairs (red, blue) and receiver (green).

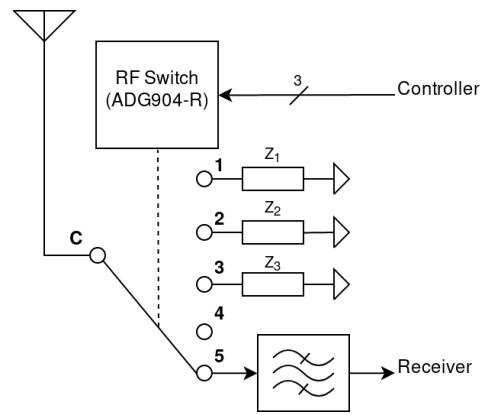


Figure 5.9: Block diagram of the backscatter transmitter

with $Z_a = 50 + 0j\Omega$. The $Z_{L,i}$ for each $\Gamma_{L,i}$ are listed in table 5.1. The component values have been calculated using $Z_L = j\omega L$ and $Z_C = \frac{1}{j\omega C}$ with $\omega = 434 \cdot 10^6 \cdot 2\pi$:

$$Z_L = 50j = j \cdot 434 \cdot 10^6 \cdot 2\pi \cdot L \implies L = 18.336nH \approx 18nH \tag{5.2}$$

$$Z_C = -50j = \frac{1}{j \cdot 434 \cdot 10^6 \cdot 2\pi \cdot C} \implies C = 7.334pF \approx 7.3pF \tag{5.3}$$

5.3 Component schematic

The impedance switching as depicted in figure 5.9, requires an RF switch that can load the antenna with 5 different impedance levels. This is possible by using a 4-pole RF switch which an enable signal, where a disabled reflective switch will create an open circuit impedance state (Z_4 of table 5.1).

The switch must have switching times that are sufficiently quick to modulate symbols at 1 to 10 kHz, thereby introducing a requirement that the switching times of the switch are far smaller than $100\mu s$ (10kHz).

Only the Analog Devices ADG904-R[61] was found to satisfy the following requirements:

Z_i	$\Gamma_{L,i}$	$Z_{L,i}$	Component
Z_1	$-j$	$-50j\Omega$	7.3pF RF capacitor
Z_2	j	$50j\Omega$	18nH RF inductor
Z_3	-1	0Ω	0Ω resistor / jumper to ground
Z_4	1	$\infty\Omega$	Open circuit
Z_5	0	50Ω	SAW filter of receiver

Table 5.1: Load impedances for the backscatter transmitter.

- Single pole 4 taps (SP4T) RF switch
- Reflective ports (no termination)
- >434MHz -3dB bandwidth
- Fast ($\ll 100\mu\text{s}$) switching times
- Operable at any point between 1.8V to 3.0V
- Low quiescent power ($< 10\mu\text{A}$)

Figure 5.10 shows the schematic of the backscatter transmitter. The mapping between the block diagram and pins on the schematic do not match, as the pin selection has been optimized for board layout. Pin RF3 is used for the receiver. Components marked as "DNP" indicate Do Not Place (leave open).

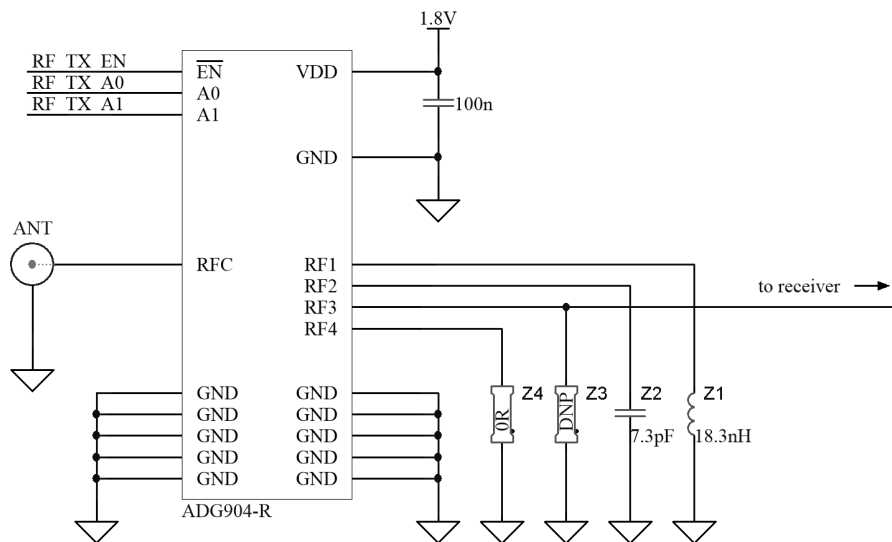


Figure 5.10: Schematic diagram of ADG904-R based switch circuit used as a backscatter transmitter and signal bypass for the receiver.

6 | Low power ASK receiver

6.1 Block Diagram

The signal path of the receiver is shown in figure 6.1. The antenna is connected through the backscatter transmitter, but the transmitter has been omitted in this diagram for simplicity. The receiver input acts as a 50Ω matched input for the antenna, which could be used as a backscatter load.

The antenna signal is first filtered through a SAW filter, to attenuate out-of-band signals and select the 433.92MHz band. The signal is then demodulated using a square law detector, which passes only the envelope of the RF signal (removing the carrier). The signal is band-pass filtered to only keep the symbol frequencies. The signal is then amplified using the programmable gain amplifier (PGA), which can be controlled digitally via the microcontroller. The PGA has a switchable gain and band-pass frequency response.

The PGA output signal is put into a symbol decision circuit. The circuit decides which symbol is being received by comparing the instantaneous and averaged PGA output. The symbol output is a digital output which can be decoded further into bits and packets using the microcontroller.

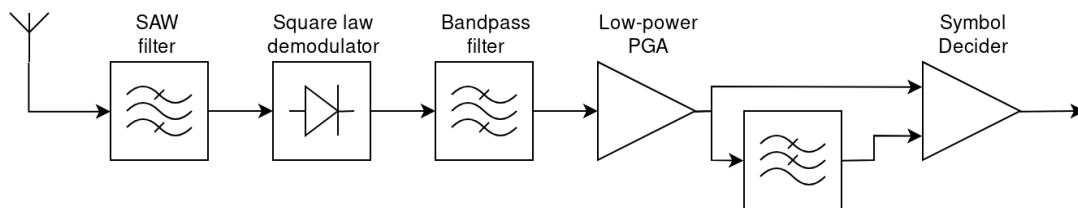


Figure 6.1: The architecture of ASK low power receiver

6.2 Circuit Design

A more detailed schematic diagram of the receiver is shown in figure 6.2. The band selection filter is implemented using a SAW (surface acoustic wave) filter. These filters have some insertion loss (several dB), however, offer a very sharp roll-off for signals that are outside the band. This is necessary since the square law detector does not have selectivity.

The impedance of the antenna, SAW filter and detector diode ports are impedance matched to optimize for maximum power transfer. SMA-style antenna's and SAW filters are typically available in 50Ω variants, where some custom or PCB style antennas may have varying (complex) impedances. The impedance of the detector circuit is however, hard to quantify since it contains a non-linear demodulation diode. It has been chosen to add an LC tank, which output impedance is matched to allow maximum power transfer for the weakest input signal.

The output of the diode detector is then filtered using 2 combinations of R-C filters. A low-pass filter is created using R_3 & C_2 and a high-pass filter is created using R_5 & C_3 . The opamp is biased through R_5 at $V_{bias} = V_{DD} / 2 = 0.9V$.

The opamp circuit is a modified non-inverting voltage amplifier. The feedback path through R_1 has been modified with the addition of an AC coupling capacitor. This makes the opamp circuit a voltage-follower for DC signals, however, it has a set gain for the pass-band and then have the gain roll-off due to the finite gain-bandwidth product (GBW) of the opamp.

The ratio of the R_1 and R_2 will set the gain of the amplifier and thereby the low-pass -3dB of the pass-band. The high-pass -3dB frequency is set using R_1 and C_1 . Since $R_1 + C_1$ are in series and connect to ground, it is possible to add a second parallel circuit with a different R+C time constant. Since R_1 is involved in setting the gain (which sets the low-pass frequency) and the high-pass frequency, it is possible to program the pass-band using a parallel $R'_1 + C'_1$ circuit and a signal transistor (MOSFET).

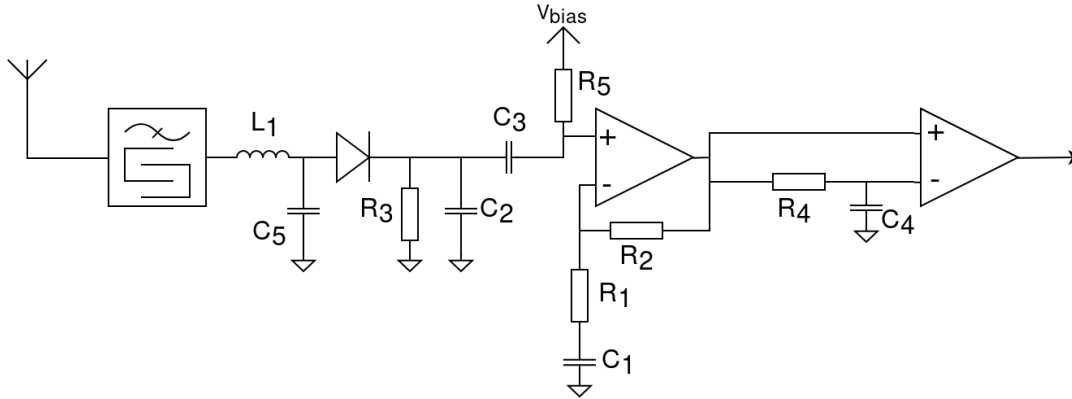


Figure 6.2: Circuit schematic of ASK low power receiver

6.2.1 Envelope Detector

A square law detector element is used in this design, which detects the amplitude envelope of the RF signal. In literature, the Qualcomm HSMS-285x[62] and HSMS-286x[63] series of RF detector diodes are very popular for their nominal $50\text{mV}/\mu\text{W}$ voltage sensitivity.

The diode tangential signal sensitivity (TSS) specifies the sensitivity at which the output SNR is 8dB[64]. The noise equivalent power (NEP) of a detector diode is typically modelled as a resistor R_j (the dynamic impedance), where the value of $R_j = \frac{\partial V_D}{\partial I_D} = \frac{Nv_T}{I_S + I_B}$ [62], and depends on the diode saturation current I_S (fixed) and biasing current I_B . The TSS can be calculated using[64]:

$$P_{TSS} = \frac{2.5\sqrt{4kTR_jB_v}}{\gamma} \quad (6.1)$$

where $\sqrt{4kTR_j}$ is the noise equivalent power (NEP) of R_j (Johnson-Nyquist noise), B_v is the video bandwidth (typically specifications assume 2MHz), and γ is the voltage sensitivity per power (V/W).

The HSMS-285x series has an $R_j = 8829\Omega$ and a specified TSS of -57dBm for $B_v=2\text{MHz}$ [62]. For 1kHz bandwidth, the TSS should theoretically decrease to -74dBm. At 10kHz bandwidth, the TSS increases to -69dBm. The HSMS-286x series is better suited at higher frequency bands, however, it has an $R_j = 529k\Omega$. Although this impedance can be lowered with bias current, this will require extra quiescent power. Without bias, the HSMS-286x series has a TSS of -65dBm at 1kHz and -60dBm at 10kHz.

6.2.2 Opamp 1/f noise mitigation

For extremely low-bit rate ASK receivers, the pass-band of the amplifier will be well into the 1/f input voltage noise density curve. The high amplification of this 1/f noise results in a very high

noise at the output, and defeats the purpose of using lower bandwidths with higher gain in the amplifier.

Appendix A presents an analysis of receiver noise performance. It was shown that the opamp voltage noise contributes significantly to the output noise, and it is an important selection criterion for the chosen opamp in the circuit. A so-called chopper operational amplifier can be used to mitigate most of the $1/f$ flicker noise.

A chopper opamp performs an internal chopping operation twice, such that the input spectrum is mirrored around f_{chop} , effectively putting DC signals nearby f_{chop} . The chopping is performed once more after amplification to put f_{chop} back to DC. The added flicker noise by the internal high-gain amplifiers will be present at f_{chop} in the output. Since f_{chop} can be far outside the band of interest, it can be suppressed sufficiently with a 1st order low-pass filter.

Chopper amplifiers typically have extremely low DC offset voltages, high open loop gain and little $1/f$ noise (i.e. flat noise density curve).

6.3 Circuit Analysis

The complete analysis (including small-signal linearization, transfer functions and noise performance) can be found in appendix A. The performance analysis section will take the results from this appendix as a base to predict and quantify the performance of the receiver.

6.4 Part Choice

6.4.1 Opamp Comparison

The performance of a wide selection of op-amps has been predicted using a Mathematica script. The script performs a circuit simulation according to the model (available in appendix A). The model incorporates the filter dimensioning & noise models.

For each available design using a particular opamp and bitrate, an expected sensitivity is dimensioned. This sensitivity is then used to calculate an RRB using equation 3.5. The expected power consumption of each part is also available using the datasheet typical power consumption. The opamp is expected to drive a high impedance load ($\gg 100k\Omega$), so it is not necessary to incorporate the load impedance in the power consumption.

The power consumption of each design also incorporates the expected power consumption of the STM32L431 microcontroller[40], which will be expected to consume $30\mu W$ when running at a clock speed 100kHz. This clock speed should be sufficient to implement the digital baseband processing functionality. For more details see chapter 7.

A figure-of-merit has been used that measures the trade-off between sensitivity and power. The FOM takes the reciprocal of RRB and power and is defined as $FOM = \frac{B}{P}$, where B is in m^2 and P in μW .

Tables 6.1 to 6.4 show an overview of all opamp parts that were considered in this calculation. Part selection is based on the parametric search engines of analog semiconductor suppliers TI, Maxim, Analog Devices, Microchip and STMicroelectronics. Over 25 parts have been investigated with current consumption up to $30\mu A$ at 1.8V. The calculated range-reach budget is calculated using $f = 434MHz$ and an exciter power of 20dBm (100mW).

As can be seen from the tables, the TLV333 is not the best part for any chosen symbol frequency. However, its performance remains fairly consistent in the top 4 rankings of all reviewed parts, making it an excellent choice for an experimental backscatter node platform.

Rank	Part	Power	Sensitivity	RRB	FOM
1	LTC2066	36.5	-69.0	85.6	2.35
2	TLV379	30.2	-66.3	62.6	2.07
3	TLV333	53.6	-69.8	93.8	1.75
4	ADA4051-1	50.0	-68.9	84.1	1.68
5	ISL28133	55.4	-69.2	87.1	1.57
6	LMP2231	41.0	-66.4	63.5	1.55
7	NCS333	60.8	-69.1	85.8	1.41
8	OPA193	77.0	-69.6	91.7	1.19
9	TSZ121	78.8	-69.7	92.6	1.17
10	ADA4505-1	39.2	-61.4	35.5	0.91
11	MCP6421	32.9	-59.8	29.5	0.90
12	LT6000	46.4	-62.7	41.1	0.89
13	AD8505	52.7	-63.0	42.7	0.81
14	NCS20091	59.0	-63.5	45.1	0.76
15	OPA317	60.8	-63.3	44.1	0.73
16	NCS325	60.8	-63.2	43.7	0.72
17	MAX4240	48.2	-56.2	19.6	0.41
18	MCP6231	59.0	-55.9	19.0	0.32
19	TSV711	41.0	-50.1	9.63	0.23
20	MAX9914	59.0	-48.5	8.06	0.14
21	TLV2760	59.0	-41.0	3.40	0.06
22	TSV621	75.2	-42.8	4.16	0.06
23	TSV6290	75.2	-40.6	3.25	0.04

Table 6.1: Comparison of opamps tuned for 10Hz. Power is in μW , sensitivity in dBm and 'RRB' is the range-reach budget in m^2 .

Rank	Part	Power	Sensitivity	RRB	FOM
1	TLV379	30.2	-64.4	50.2	1.66
2	LTC2066	36.5	-64.3	49.5	1.36
3	LMP2231	41.0	-64.6	51.7	1.26
4	TLV333	53.6	-65.2	55.2	1.03
5	ADA4051-1	50.0	-64.1	48.7	0.97
6	ISL28133	55.4	-64.9	53.5	0.96
7	LT6000	46.4	-63.0	42.8	0.92
8	OPA317	60.8	-65.2	55.3	0.91
9	ADA4505-1	39.2	-61.2	34.5	0.88
10	MCP6421	32.9	-59.6	29.0	0.88
11	NCS333	60.8	-65.0	53.5	0.88
12	NCS20091	59.0	-64.5	50.9	0.86
13	NCS325	60.8	-64.0	47.8	0.79
14	AD8505	52.7	-62.5	40.4	0.77
15	MAX4240	48.2	-60.9	33.5	0.70
16	TSZ121	78.8	-65.1	54.3	0.69
17	TSV711	41.0	-59.2	27.6	0.67
18	MCP6231	59.0	-62.0	38.2	0.65
19	OPA193	77.0	-61.5	35.8	0.46
20	MAX9914	59.0	-55.1	17.2	0.29
21	TLV2760	59.0	-48.6	8.16	0.14
22	TSV621	75.2	-50.6	10.3	0.14
23	TSV6290	75.2	-46.3	6.26	0.08

Table 6.2: Comparison of opamps tuned for 100Hz. Power is in μW , sensitivity in dBm and 'RRB' is the range-reach budget in m^2 .

Rank	Part	Power	Sensitivity	RRB	FOM
1	TLV379	30.2	-55.6	18.2	0.60
2	TLV333	53.6	-60.3	31.1	0.58
3	MCP6421	32.9	-55.6	18.2	0.55
4	NCS20091	59.0	-60.6	32.3	0.55
5	ISL28133	55.4	-60.0	30.2	0.54
6	LMP2231	41.0	-57.2	21.8	0.53
7	LTC2066	36.5	-56.0	19.1	0.52
8	OPA317	60.8	-60.3	31.2	0.51
9	TSV711	41.0	-56.8	21.0	0.51
10	MCP6231	59.0	-60.0	30.1	0.51
11	NCS333	60.8	-60.1	30.4	0.50
12	NCS325	60.8	-59.0	27.0	0.44
13	ADA4051-1	50.0	-57.0	21.4	0.43
14	TSZ121	78.8	-60.1	30.7	0.39
15	MAX4240	48.2	-55.6	18.2	0.38
16	AD8505	52.7	-55.8	18.7	0.35
17	ADA4505-1	39.2	-53.0	13.5	0.35
18	LT6000	46.4	-53.0	13.5	0.29
19	MAX9914	59.0	-54.9	16.8	0.28
20	TLV2760	59.0	-54.7	16.4	0.28
21	TSV621	75.2	-55.9	18.9	0.25
22	TSV6290	75.2	-55.3	17.7	0.23
23	OPA193	77.0	-51.5	11.3	0.15

Table 6.3: Comparison of opamps tuned for 1kHz. Power is in μW , sensitivity in dBm and 'RRB' is the range-reach budget in m^2 .

Rank	Part	Power	Sensitivity	RRB	FOM
1	TLV2760	59.0	-53.0	13.5	0.23
2	ISL28133	55.4	-52.0	12.1	0.22
3	MAX9914	59.0	-52.4	12.7	0.21
4	TLV333	53.6	-51.5	11.3	0.21
5	TSV6290	75.2	-54.3	15.8	0.21
6	NCS20091	59.0	-51.5	11.3	0.19
7	TLV379	30.2	-45.6	5.74	0.19
8	NCS333	60.8	-51.5	11.3	0.19
9	NCS325	60.8	-51.5	11.3	0.19
10	MCP6231	59.0	-50.8	10.5	0.18
11	MCP6421	32.9	-45.6	5.74	0.17
12	OPA317	60.8	-50.8	10.5	0.17
13	LMP2231	41.0	-47.2	6.90	0.17
14	LTC2066	36.5	-46.0	6.05	0.17
15	TSV621	75.2	-52.3	12.4	0.16
16	TSV711	41.0	-46.8	6.63	0.16
17	TSZ121	78.8	-52.0	12.1	0.15
18	ADA4051-1	50.0	-47.0	6.77	0.14
19	MAX4240	48.2	-45.6	5.74	0.12
20	AD8505	52.7	-45.8	5.90	0.11
21	ADA4505-1	39.2	-43.0	4.28	0.11
22	LT6000	46.4	-43.0	4.28	0.09
23	OPA193	77.0	-41.5	3.58	0.05

Table 6.4: Comparison of opamps tuned for 10kHz. Power is in μW , sensitivity in dBm and 'RRB' is the range-reach budget in m^2 .

6.4.2 Passives

All passives are chosen to create the smallest possible pass-band for the receiver. For the circuit depicted in 6.1, it has been chosen that $R_3 = R_4 = 100k\Omega$, $R_5 = 200k\Omega$, $C_2 = C_3 = 18nF$, $C_4 = 100nF$, $R_2 = 348k\Omega$ and the pairs of R_1, C_1 are $1k\Omega / 680nF$ for 1kHz bitrate, and $10k\Omega / 6.8nF$ for 10kHz bitrate.

6.4.3 Performance

Tables 6.5 and 6.6 show the overall noise calculation for 1kHz and 10kHz bit-rates respectively, while using the HSMS-285B detector[62] diode and TLV333 amplifier[65]. It can be seen that the noise floor of the circuit increases by a factor of $\sqrt{10}$ for a 10x higher gain factor.

Part	Flatband Density	σ_{out} (mV)
HSMS-285B	$12nV/\sqrt{Hz}$	0.167
R3	$41nV/\sqrt{Hz}$	0.0513
R5	$41nV/\sqrt{Hz}$	0.166
v_n opamp	$55nV/\sqrt{Hz}$	0.763
i_n non-inv	$100fA/\sqrt{Hz}$	0.032
i_n inv	$100fA/\sqrt{Hz}$	1.30 E-3
R1	$4.1nV/\sqrt{Hz}$	1.05
R2	$76nV/\sqrt{Hz}$	2.98 E-3
R4/C4	$41nV/\sqrt{Hz}$	0.2 E-3
Total		1.56

Table 6.5: Noise contributors in TLV333-based PGA tuned for 1kHz

Part	Flatband Density	σ_{out} (mV)
HSMS-285B	$12nV/\sqrt{Hz}$	0.052
R3	$41nV/\sqrt{Hz}$	0.016
R5	$41nV/\sqrt{Hz}$	0.052
v_n opamp	$55nV/\sqrt{Hz}$	0.240
i_n non-inv	$100fA/\sqrt{Hz}$	0.002
i_n inv	$100fA/\sqrt{Hz}$	0.412 E-3
R1	$1.3nV/\sqrt{Hz}$	0.319
R2	$76nV/\sqrt{Hz}$	9.0 E-3
R4/C4	$41nV/\sqrt{Hz}$	0.2 E-3
Total		0.406

Table 6.6: Noise contributors in TLV333-based PGA tuned for 10kHz

6.4.4 Comparator Hysteresis

The comparator hysteresis level is chosen depending on the noise level. For example, if an SNR of 10dB is desired to keep the BER sufficiently low, then the worst noise magnitude is taken and increased with 10dB. In this case, a hysteresis of approximately 8mV is needed to accommodate the 1kHz and 10kHz receiver modes with the same comparator.

The sensitivity at 1kHz and 10kHz can then be estimated as follows. It is given that the comparator needs 8mV amplitude to detect a symbol and that the (nominal) conversion gain is 350x and 35x for 1kHz/10kHz respectively. This gives a minimum input voltage amplitude of 23 to 229 μV . According to the HSMS-285B[62] datasheet and assuming a modest voltage sensitivity of 30mV/ μW (50mV/ μW advertised), then a sensitivity of -54dBm / -44dBm for 1kHz/10kHz can be expected.

It is important to note that if a receiver is built which is dimensioned only for 10kHz, then a comparator hysteresis of only 2.5mV ($\sqrt{10}$ smaller) is needed. The sensitivity of the receiver at 10kHz is then -49dBm, which is 5dB ($= \sqrt{10}$) better than the receiver with bitrate switching capability.

6.5 Bitrate efficacy on sensitivity

Having established that lowering the bitrate significantly improves the sensitivity of a receiver given the right circuit design, it is possible to investigate to what limits these modifications can work. From the previous analysis, it is possible to define 3 constraints which limit the sensitivity of a receiver when it is specifically tuned to a particular bitrate:

- **GBW:** A higher bit-rate receiver requires more bandwidth, but also sufficient gain to amplify the incoming input signal such that it is sufficient to surpass the hysteresis level of the comparator.
- **Circuit Noise:** If the bitrate and thus bandwidth is lowered, then it is possible to exploit more gain an opamp (given constant GBW). However, at some point, the circuit noise will dominate over the amplified signal and the SNR becomes insufficient. A required SNR of 10dB is considered in this analysis.
- A_{VOL} : All op-amps have a specified open-loop voltage gain. Typically op-amps are used with gains where a highly linear amplifier is realized with insignificant residual errors. At extremely low bitrates (e.g. 10Hz) the desired gain introduces a limitation. An upper bound for the voltage gain of the PGA is set at $A_{VOL}/50$, where a factor of 50 is chosen such that the part has sufficient loop gain left to provide an accurate output.

Figure 6.3 shows the sensitivity for various bitrate tuning (x-axis) of the diode detector and PGA. As was described, the comparator hysteresis has been chosen such that an SNR of 10dB remains when the amplifier is configured to operate at 1kHz. This is visible in the plot since the GBW limit (i.e. not enough signal amplitude for reliable detection) becomes the bottleneck at 1kHz.

If a lower comparator amplitude is chosen, then the GBW limit line will move downwards, which could suggest a similar sensitivity at 1kHz while yielding a better performance at 10kHz. However, in that case, many false glitches will be detected due to noise.

The black line indicates the "worst-case" of all 3 regions. Since the slope (in the logarithmic domain) of the GBW limit is constant, the efficacy of the programmable bitrate design is also constant. For a given distance, in this example factor 10 was chosen, an equiproportional gain in sensitivity (10dB) is achieved, which translates to an increased range-reach budget of $\sqrt{10}$.

Choosing an even lower bit-rate design requires different gain values (which is modelled in this graph), but also a different comparator threshold (not modelled in the graph). With the comparator threshold, the GBW limit boundary will shift accordingly. Overall, the performance can then improve by 5dB per decade, up to the A_{VOL} limit.

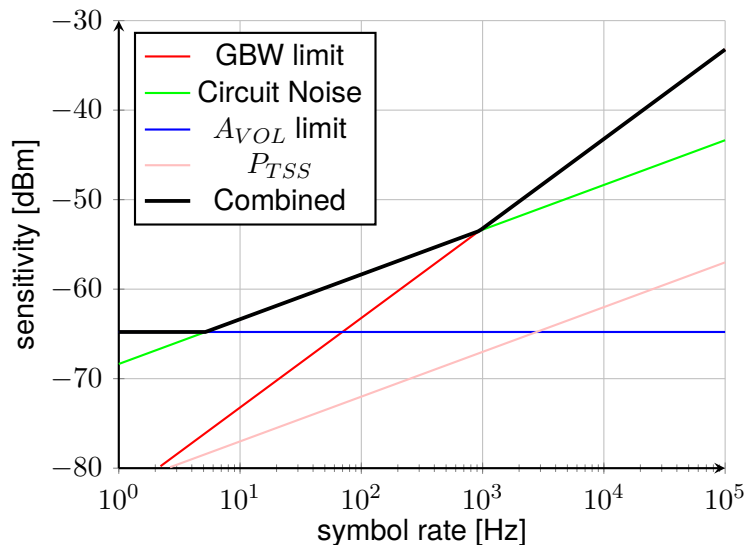


Figure 6.3: Symbol rate versus predicted sensitivity, with comparator hysteresis set to 8mV.

7 | Radio Firmware

The microcontroller will handle all digital functions for the radio; this includes the physical layer and upwards in a standard OSI model. Thereby it puts requirements on processing raw symbols from the analog receiver to bits, communication packets and application-specific tasks.

7.1 Software Architecture

Figure 7.1 shows an informal representation of the firmware architecture. The arrows indicate which modules are called by other software modules. The following distinct layers are visible:

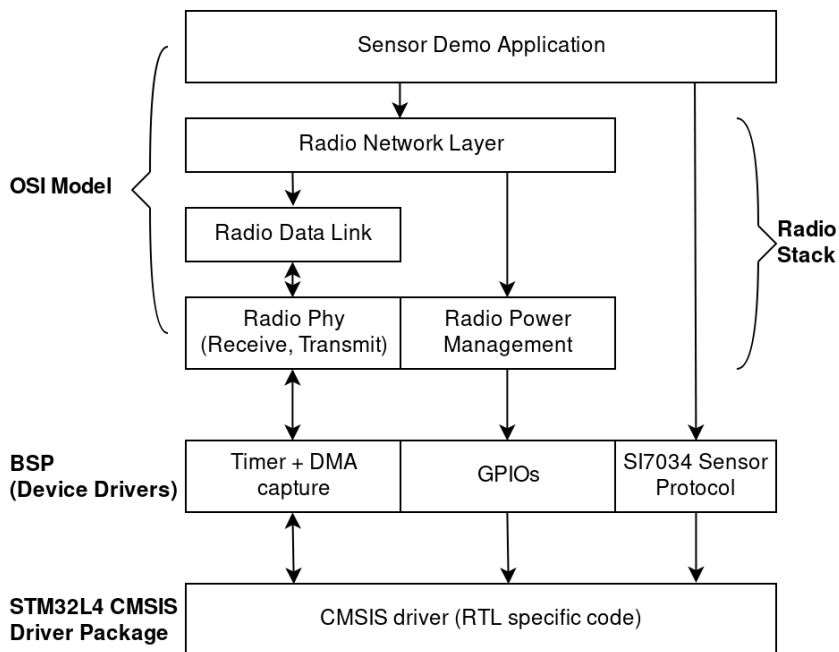


Figure 7.1: Informal graphical representation of firmware architecture

- **CMSIS driver package** The manufacturer ST supplies a supplementary driver package called the "Cortex Microcontroller Software Interface Standard" (CMSIS). This software package provides C functions, such as initialization and using peripherals, for the particular microcontroller series and model. All other blocks (BSP and above) are custom firmware of this thesis project.
- **BSP** The Board Support Package provides C/C++ functions for the sensor application and radio network stack to make use of the available hardware. The BSP hides hardware implementation specific code, thereby allowing interchangeability between hardware implementations or even environments (PC simulation).
- **Radio Stack** The current radio stack covers 3 layers:
 - **Radio Phy** The physical layer accepts blocks of (half) symbols from the DMA transfers and decodes these into bits, finds synchronization (preamble) and performs CRC checking on complete packets. In transmit, it takes a raw packet and encodes it into symbols, while including CRC, preamble and synchronization.

- **Radio Data Link** The data link assists in CRC checking, provides packet buffering and contains finite state machines (FSM) for the physical layer. In later revisions, this layer will also be responsible for MAC functions.
- **Radio Network Layer** In the context of multi-hop routing, this layer will decide if a received packet needs forwarding or processing by the sensor application.
- **Sensor Demo Application** The demo application will periodically poll the radio stack for packets. If needed, it can access the BSP to sample the Si7034 temperature & humidity sensor and transmit this information using the radio stack.

In the remaining of this chapter, a top-down description will be given starting at the radio data link layer. For a complete proof of concept of the intended sensor application, the network (multi-hop routing) and sensor demo (sampling, gateway, etc.) must also be implemented. This is, however, due to time constraints, outside the scope of this thesis.

Experiments will thereby test the range and reach improvement of a single tag-to-tag link only, as was analyzed in chapter 3.

7.2 Radio Physical & Data Link

7.2.1 Tight Coupling

In the current implementation, the data link and physical layers are tightly coupled. The reason for this tight coupling is because symbols are to be processed in blocks as captured by the DMA hardware.

DMA was chosen since it can reduce the power consumption of the firmware implementation. This is because of reduced overhead from interrupts entry & exit (CPU cycles 'wasted' on stack pushing and popping). In addition, when the radio routines are waiting for a DMA transfer to complete, the CPU can be used for other tasks or turned off, causing the device to enter a power efficient state (sleep/idle) faster.

On the downside is that DMA may increase the latency depending on the DMA block size and processing requirements.

The choice for using DMA at an early stage does complicate the proof-of-concept radio processing routines. However, by investing time early into a more optimized implementation, it can be avoided that the software architecture must be redefined at a later stage of the project.

7.2.2 FM0 Encoding

FM0 is a line encoding scheme used to remove DC bias in the transmitted symbols. The "low" or "high" time should be about one half on average; regardless of whether a continuous stream of 1s or 0s is sent.

Figure 7.2 shows an example of FM0 encoding. Each bit period toggles the current symbol value. However, a '0' has an extra toggle at half of the symbol period.

Each bit now requires 2 symbols to be sent: either a single (stretched) toggle for a '1', or 2 successive toggles. The encoding is also level insensitive, since flipping the symbols won't corrupt the data.

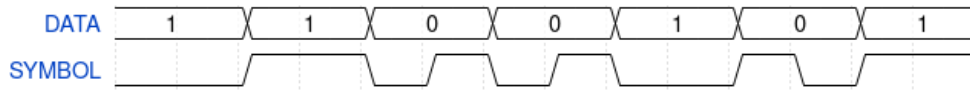


Figure 7.2: Example of a few bits encoded in FM0

7.2.3 Radio Frames & Packet definitions

The data link layer communicates with the network layer using small packets. Table 7.1 shows the structure of a data packet. The packet contains a small header of 4 bytes and a variable size payload.

The length field indicates the size of the complete packet, including the header, making that the payload size n is $length - 4$. Thereby the length value must be between 4 and $4 + n_{max}$, where n_{max} is the maximum packet size allowed due to fixed buffer sizing (32 bytes in this implementation).

The header contains source and destination fields for basic routing functionality. Further, the packet contains a checksum by using a CRC with polynomial B7h.

In the data link & physical layer, the translation is performed between frames and packets. A frame encodes information in an array of pulse lengths, alternating between an indication of the high and low time. The high/low times thus describe an FM0 symbol, where 1 long pulse indicates a "1" and 2 short pulses indicate a "0" (matching figure 7.2). Table 7.2 shows an abstract representation of the fields in a frame. A frame also contains a preamble and unique ID, which are used by the receiver to synchronize with the data transmission.

The high and low pulse width times are measured by a hardware timer, which is abstracted inside the BSP layer. A frame symbol value is equal to the number of clock ticks of the hardware timer, after which it must toggle its output. Likewise, for receiving, an input toggle event will be used to capture the counter value of the timer, which is the measurement of the pulse width. The exact implementation of the STM32L431 timers is described in the BSP section.

The radio phy requires interaction with the BSP to know what clock frequency the timer peripheral counts at, such that it can determine the required pulse widths for short and long pulse duration. The calculation of the short and long pulse duration is as follows:

$$long = \frac{f_{tmrclk}}{bitrate} \quad (7.1)$$

$$short = \frac{long}{2} \quad (7.2)$$

With $f_{tmrclk} = 100kHz$, $bitrate = 1kHz$, then $long = 100$ cycles and $short = 50$ cycles.

7.2.4 Transmitter Implementation

Algorithm 1 shows the procedure for FM0 encoding. The algorithm shows that first the preamble and synchronization bytes are encoded. After that, each byte of the packet is processed and turned in 'short' and 'long' symbols. These symbols indicate the pulse width of a zero or one that is sent.

Figure 7.3 shows a graphical representation of a packet to be transmitted as a frame. The rectangle colours indicate the field of a packet to be encoded. During encoding of a frame, the preamble and synchronization ID are prepended. A packet is always encoded one-to-one into a frame representation, meaning that the frame buffer must be sufficiently sized to contain the

Field	Type	Contents
Length	uint8	$n = length - 4$
Src	uint8	node ID
Dst	uint8	node ID
CRC	uint8	checksum
Payload	uint8[n]	data

Table 7.1: Memory structure of a data packet

Field	Type	Contents
Preamble	uint8[..]	[F0h, ...]
Sync	uint16	2DD4h
Length	uint8	$n = length - 4$
Src	uint8	node ID
Dst	uint8	node ID
CRC	uint8	checksum
Payload	uint8[n]	data

Table 7.2: Abstract representation of a frame

worst-case size of a packet. An EOF (End of Frame) is inserted by keeping the transmit output constant for multiple symbol periods.

The maximum size of a packet is 36 bytes: up to 32 byte payload and a 4 byte header. In addition, a 2-byte synchronization ID and a (configurable) 4 byte preamble are added. This results in a total of 42 bytes for 1 packet.

The payload and header length is based on existing industry radio chipsets, such as the CC110L[54], which has a similar configuration. The datasheet of this chipset recommends a 4 byte preamble, 2-byte or 4-byte synchronization word, single byte node addressing and supports packets up to 64 bytes in total (including header etc.)

A zero symbol is represented using 2 pulses in the FM0 line encoding scheme. Therefore a total of up to 16 pulses must be stored for each byte. If a peripheral clock frequency of 100kHz is used in combination with a 100Hz bit rate, then the longest time duration of an edge is in the order of 10ms and requires a 16-bit time resolution measurement. Thereby each pulse will be stored as a 16-bit unsigned integer. The total size c_{frame} is then:

$$c_{frame} = (32 + 4 + 2 + 4) \cdot 8 \cdot 2 \cdot 2 = 1344 \text{ bytes} \quad (7.3)$$

This is a significant memory overhead for using DMA since 1344 bytes is an expansion of 37.3x compared to the size the original 1 packet. The overhead could be reduced by encoding a packet over multiple frames as is needed when time progresses, rather than performing the encoding step in 1 burst.

7.2.5 Receiver Implementation

7.2.5.1 Finite State Machine

Algorithm 2 shows the basic procedure for FM0 decoding. The algorithm accepts a block of symbols (pulse widths) and translates these into bits (for synchronization) and eventually a complete packet.

The algorithm does not show implementation details of preemption, that were required when processing is performed without the aid of a preemptive RTOS. Preemption is necessary as the packet may span across multiple frames. This behaviour is shown in figure 7.3. The frame size c_{frame} has been set to support the maximum size of a frame. Thereby in an ideal case, the same symbols have been transferred using DMA into the buffer and can be parsed starting at index zero.

However, due to interference or bit errors (insufficient SNR), the receiver buffer might contain "garbage" symbols (shown in red as interference) before the actual packet that was transmitted.

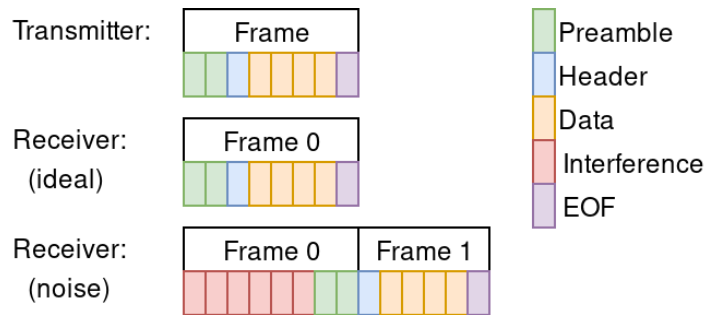


Figure 7.3: Ideal packet and frame translation, versus additional noise.

Then it is required that synchronization is first established by making use of the transmitted preamble and synchronization word.

The synchronization word has been added, such that the preamble can be of variable size. The receiver looks for a combination of a 2 byte preamble and a 2 byte synchronization word. The transmitter, however, transmits 4 bytes of preamble, such that old hardware state of the radio front-end is "flushed" first.

To support preemption of the radio algorithm, the receiver contains a state machine along with some additional state variables to support the parsing across 2 frames. The finite state machine has 3 phases of decoding:

- **Synchronization** The received symbols are decoded and appended to a shift register. Once the shift register matches a magic word (a combination of preamble and synchronization bytes), then the next state is entered which will decode the rest of the packet.
- **Header (Length)** The first byte of the header contains the packet length, which is necessary to determine how many bytes should be received by the decoder. The length byte is checked for lower and upper bounds ($4 < length < 4 + 32$). Once successful, it proceeds to the packet state. If the length is out of bounds, then the synchronization phase is entered.
- **Packet** All bytes are read from the frame symbols. Once received, the CRC is computed by the BSP driver (hardware acceleration) and checked with the transmitted CRC of the packet. If the checksum fails, the packet is rejected silently. If it succeeds, the packet will be handed over to the network layer.

If the state machine is called when a partial or complete frame has been received by hardware. A complete frame is defined as when the DMA has filled the complete buffer that was allocated for the reception. A partial frame could occur when an EOF (end of frame) event occurs, which is when a symbol timeout occurs of 10 symbol periods.

7.2.5.2 Preemptive Decoder & Decoding Granularity

The difficulty with parsing symbols (but also bytes) across 2 frames, is that support must be added for preemption of the decoding in the first frame, such that it can be resumed in the second frame.

Figure 7.4 shows a potential case of data corruption when this is not properly implemented. In this case, frame 0 contains 8 line symbols, where an "S" sample denotes a short pulse between pin toggle, and "L" denotes a long pulse. In FM0, a single long pulse denotes a "1" symbol value, while 2 short pulses denote a "0" value.

The decoder assumes that if a short symbol is observed in the list, that the next symbol must also be short (otherwise a bit error would occur), and thereby it is a reasonable optimization to skip the second "S". This is shown in figure 7.4, where the decoder starts at decoding at index 1 of frame 0, then jumps to index 3 and then 5. At index 5 a long pulse is sampled, so only a single jump is made to index 6. The decoder then jumps to index 8, and finally to index 10. Index 10 is out of bound of the buffer, indicating that decoding of this frame has completed.

However, symbol 8 of frame 0 and symbol 1 of frame 1 are 2 short pulses that belong to the same FM0 symbol. This means that incorrect parsing occurs if the decoder resumes at index 1 of frame 1 since it incorrectly skips over the "L" at index 2 of frame 1. A correct implementation is shown in figure 7.5 where the "half" symbol status of frame 0 is copied over to frame 1 at index 0. This index 0 is a virtual index, which is not filled by hardware but is rather over provisioning which the decoder can use to move leftovers from frame 0 into.

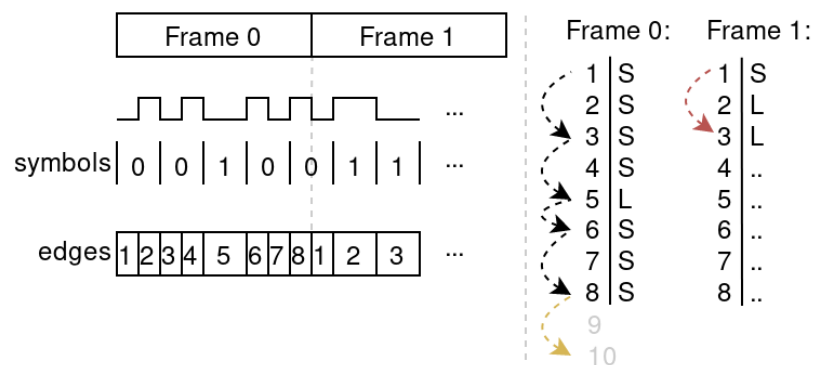


Figure 7.4: Incorrect half FM0 symbol decoding

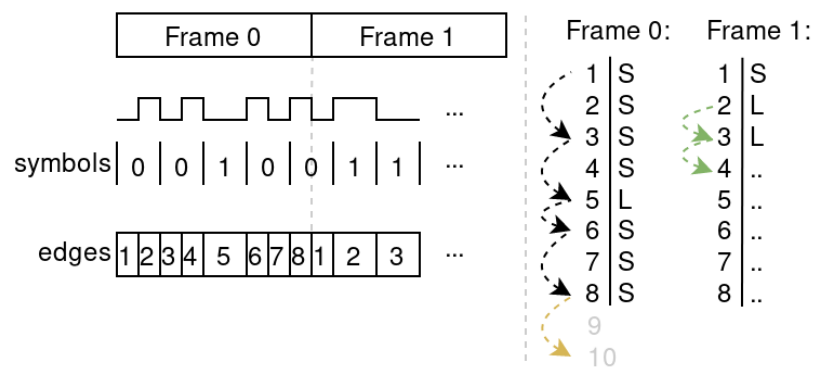


Figure 7.5: Correct half FM0 symbol decoding

The concept of over-provisioning is also explained in figure 7.6, but with the application of larger granularity decoding. To minimize the number of cycles spent per decoding of an FM0 symbol, it has been chosen to support 2 levels of decoding granularity: on a bit or byte level.

In the synchronization phase, it is not yet known at which symbol a new byte starts, so it is necessary to perform a bit level sampling of the symbol buffer until the synchronization word has been found. At this point, it is possible to decode a whole byte at once. By decoding 8 bits at once, as was also shown in algorithm 2, the compiler can unroll the decoding loop for 8 bits, and perform optimizations on a bit level (such as hardcoded bit and buffer indexing).

Additionally, only 1 buffer underflow check is performed per byte, further reducing the number of cycles spent per byte. This then also ties into the over provisioning requirement: if it has been detected that a buffer underflow can occur when 1 byte is read at once, then basically a

similar situation of a "half" symbol occurs as shown in figure 7.4 and 7.5. In figure 7.7, it is then shown what happens if a byte is split in half across frame 0 and 1: the decoder will recognize the buffer underflow, and move the leftovers to the over-provisioning space of frame 1. When the decoder is then called for frame 1, it can now successfully decode the leftovers from frame 0.

To ensure that this preemptive decoder works under all these optimization and mitigation techniques, a series of unittests (testbenches) has been written using the GoogleTest unit testing framework. These unit tests were then run on a workstation PC, such that an exhaustive sweep of all possible frame offsets can be verified to function correctly.

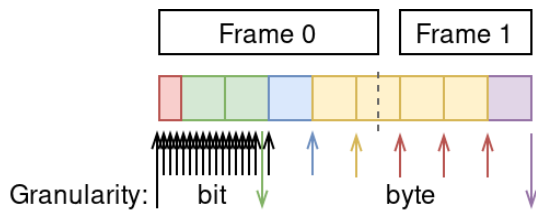


Figure 7.6: Incorrect preemption decoding

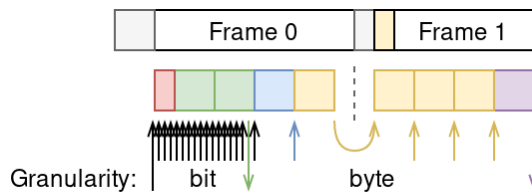


Figure 7.7: Preemption decoding support

7.3 BSP

7.3.1 Timer & DMA

The radio functions are implemented using one of the STM32L431 hardware timers. Timer peripherals at their basis have an up- or down counter, which is clocked at (an integer fraction of) the peripheral or system frequency. The current timer value can be used to compare against fixed values using a compare match module (e.g. to generate a PWM). A timer also features capture channels which can be used to measure the time(span) of rising and/or falling edge.

The STM32L4 timer contains various counting modes. The standard mode is a upcounting timer with period/autoreload. In this mode, the counter value is compared to a period value, and when matched, the counter value will be loaded with an autoreload value (which is commonly zero). The reload event can also be generated using an (external) trigger event, e.g. from an I/O pin directly (trigger + reset mode) or another timer compare output (slave timer mode).

In addition, timers can be configured to generate CPU interrupts or DMA requests using the events as mentioned earlier, for example, a counter overflow or trigger. These events are used in transmit and receive mode to move the pulse width symbol data from SRAM to the peripheral (transmit) or peripheral to SRAM (receive), even while the CPU is clock gated off. The transfer size is set at the frame size to be transmitted, or the maximum size of the receive buffer. Once all bytes have been transferred, the DMA peripheral generates an interrupt which will wake-up the CPU and jumps to the DMA interrupt routine to inform the radio stack about the hardware event.

7.3.2 Radio RTL equivalent description

Figures 7.8 and 7.9 show the equivalent RTL diagrams of the microcontroller timer peripheral configuration for the transmit and receive functions.

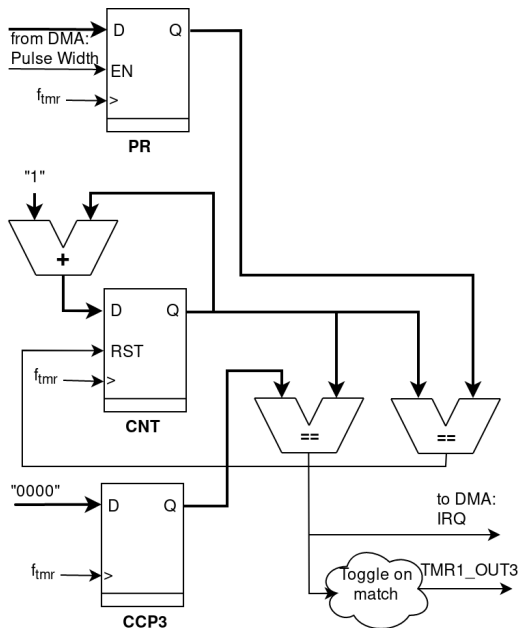


Figure 7.8: Transmitter RTL diagram.

7.3.2.1 Transmitter

The transmitter RTL is shown in figure 7.8. The timer counter **CNT** runs in a continuous up-counting mode. Once the timer value reaches the **PR** (period) value, the timer is reset to zero. The timing waveform is shown in figure 7.10. The register **CCP3** holds a compare value with the timer counter value and generates a match for the fixed value zero. This value is used to toggle the I/O pin of the radio. The mechanism described up until now will generate a square wave with fixed pulse widths.

To send the symbols in those pulse widths, the compare match will also trigger a DMA transfer event. The DMA transfer has been set up to write a new pulse width to the **PR** register, which will change the time at which the timer will reset and a pin toggle is performed.

Although the DMA transfer may have some latency as it must propagate through the microcontroller peripheral bus structure (not shown in figure 7.10), the typical pulse widths will be long enough for this not to be a limitation (in the order of 50 cycles).

7.3.2.2 Receiver

The RTL of the receiver is shown in figure 7.9. The period register **PR** is not used. The timer is still run in a continuous up-counting mode. The edge detector logic has been set to create a trigger event on both the rising and falling edge. Once this trigger occurs, the **CCP1** (capture compare channel 1) register will capture the current timer counter value. In addition, the counter value will be reset to zero. The trigger will also initiate a DMA transfer request, which will copy the contents of **CCP1** into SRAM. The timing waveform is shown in figure 7.11.

Not pictured in figure 7.9 is **CCP2**, which has been set up to generate a processor interrupt on a bit timeout. This timeout can be used to abort the current DMA transfer and process any values that were captured. The EOF interrupt is meant to reduce the latency to processing since otherwise, the system will keep waiting till the DMA transfer has filled the maximum allocated buffer space.

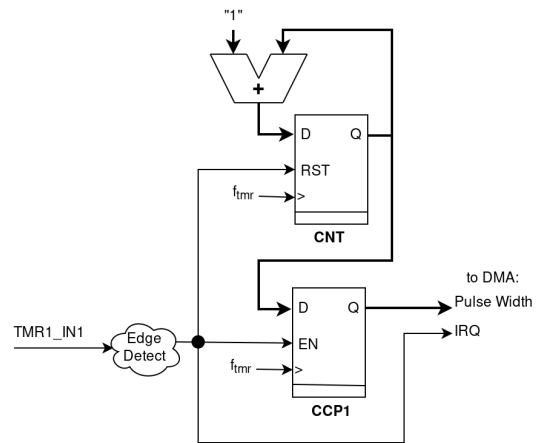


Figure 7.9: Receiver RTL diagram.

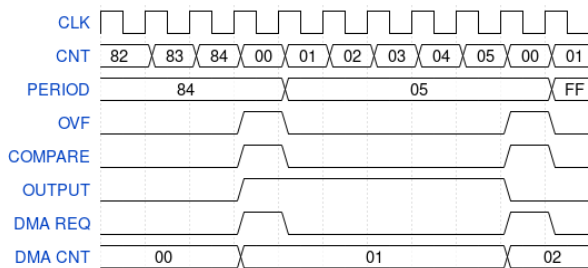


Figure 7.10: Timing in transmitter operation

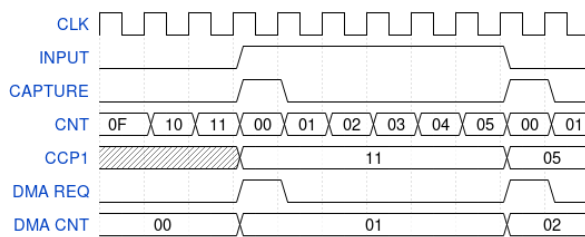


Figure 7.11: Timing in receiver operation

Algorithm 1: Algorithm for FM0 encoding**Input:** RF packet P **Output:** array of pulsewidths**Output:** j no of pulses**Data:** preamble: array of bytes (F0h, F0h, F0h, F0h, 2Dh, D4h)

```

1   $j \leftarrow 0$ 
2  for each byte  $B$  in preamble do
3      for bit  $\leftarrow 7$  to 0 do
4          if  $B \& (1 \ll \text{bit})$  then
5              edges[ $j$ ]  $\leftarrow$  LONG;
6               $j \leftarrow j + 1$ ;
7          else
8              edges[ $j$ ]  $\leftarrow$  SHORT;
9              edges[ $j+1$ ]  $\leftarrow$  SHORT;
10              $j \leftarrow j + 2$ ;
11         end
12     end
13 end
14 for each byte  $B$  in  $P$  do
15     for bit  $\leftarrow 7$  to 0 do
16         if  $B \& (1 \ll \text{bit})$  then
17             edges[ $j$ ]  $\leftarrow$  LONG;
18              $j \leftarrow j + 1$ ;
19         else
20             edges[ $j$ ]  $\leftarrow$  SHORT;
21             edges[ $j+1$ ]  $\leftarrow$  SHORT;
22              $j \leftarrow j + 2$ ;
23         end
24     end
25 end

```

Algorithm 2: Algorithm for FMO decoding

Input: array of pulsewidths**Input:** size: no of pulses**Output:** P: RF packet**Data:** i: byte index in P**Data:** sr: preamble synchronization shift-register

```
1 i ← 0;
2 sr ← 0;
3 for j ← 0 to size do
4   if edges[j] > (SHORT+LONG)/2 then
5     | sr ← (sr « 1) | '1';
6   else
7     | sr ← (sr « 1) | '0';
8     | j ← j + 1;
9   end
10  if sr = F0F02DD4h then
11    | goto decode-packet
12  end
13 end
14 return PREAMBLE-FAILURE;
15 decode-packet:
16 for j ← up to size do
17   data ← 0;
18   for bit ← 7 to 0 do
19     | if edges[j] > (SHORT+LONG)/2 then
20       | data ← data | (1 « bit) j ← j + 1;
21     else
22       | j ← j + 2;
23     end
24   end
25   P[i] ← data;
26   i ← i + 1;
27 end
28 if CRC of P is invalid then
29   | return CRC-FAILURE
30 else
31   | return P
32 end
```

8 | Implementation & Measurements

An experimental platform for backscatter tag-to-tag research has been designed to demonstrate the range and reach variation as a function of receiver sensitivity. In addition, the prototype is meant to show that building a backscatter radio even with COTS (Complete Off The Shelf) components can yield a low power consumption.

8.1 Experimental Platform

8.1.1 Board Design

Figure 8.1 shows a block diagram of the hardware design for the sensor node. A PCB has been designed from this hardware block diagram, which is shown in figure 8.2 as a 3D CAD rendering. The 4-layer PCB has a dimension of 44x44mm, and it's shaped to fit in a 50x50mm low-cost (MPN: Hammond 1551RBK) plastic enclosure. The schematic and bill of materials can be found in appendix B.

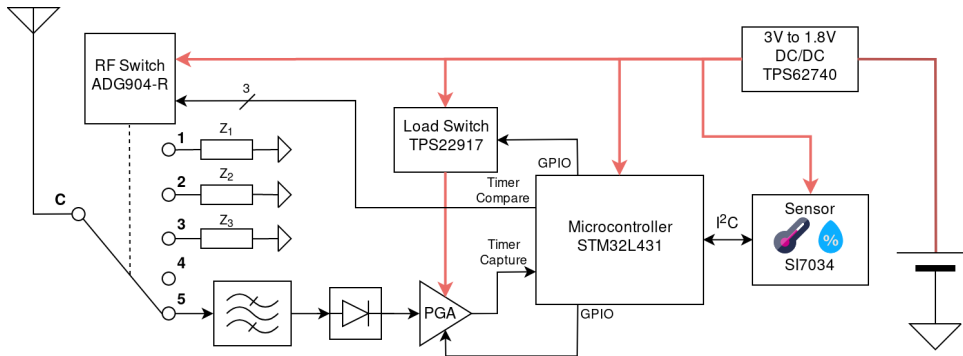


Figure 8.1: Block diagram of node hardware design

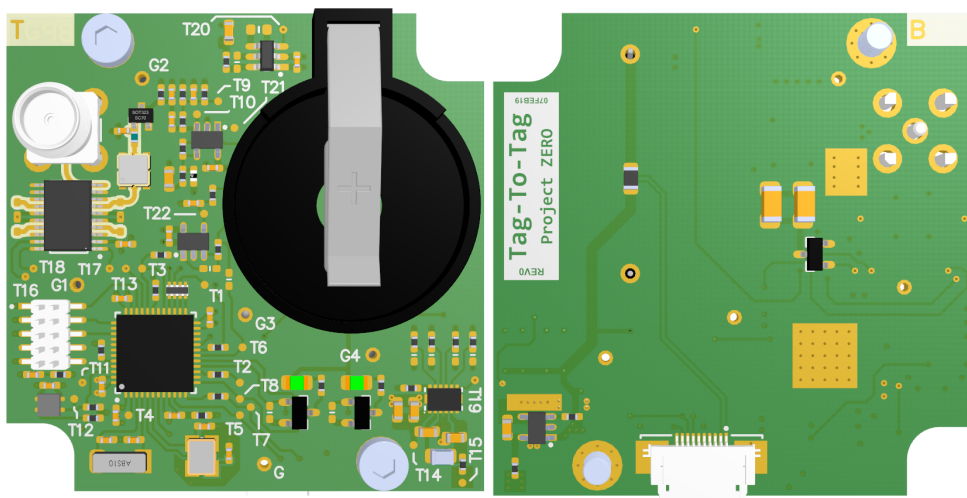


Figure 8.2: 3D CAD rendering of the PCB design for an experimental tag-to-tag backscatter platform

The antenna connects using an SMA connector to ADG904 RF switch, which then connects to the ASK receiver. The switch can also select 4 different other load impedances for the an-

tenna. The ASK receiver is power gated to reduce power consumption. The antenna chosen for initial experiments is a small-band 433.92MHz miniature antenna (MPN: TI.10.0111) from Taoglas.

The tag is powered from a CR2032 3V Lithium coin-cell. However, all board components operate at 1.8V, which is converted using a linear or buck regulator. The STM32L431 microcontroller is used to implement the digital radio and tag specific functions. It can be programmed using SWD (Serial Wire Debug) over an industry standard 10-pin Cortex Debug connector. Although the board contains footprints for a 32.768kHz and high-frequency crystal, the STM32 internal clock sources will be used for initial experiments.

8.1.2 Power Consumption

An overview of the power consumption for each device on the board is presented in table 8.1. The table lists the typical current consumption from the datasheet while being operated at a particular supply voltage. The last column P then states the power consumption for that device. Some devices have different operational modes, so multiple numbers are available that must be combined for the particular function or state the board is operating in.

Device	Functionality and operational mode	I_{DD} (typ)	V_{DD}	P
STM32L431	Microcontroller, 100kHz, CPU Running	28.38 μ A	1.8V	51.1 μ W
STM32L431	Microcontroller, 100kHz, CPU Idle	19.9 μ A	1.8V	35.8 μ W
STM32L431	Microcontroller, Sleep	0.52 μ A	1.8V	0.94 μ W
ADG904-R	Transmitter (RF switch), 0Hz	0.10 μ A	1.8V	0.18 μ W
ADG904-R	Transmitter (RF switch), 10kHz	0.16 μ A	1.8V	0.28 μ W
SI7034	Sensor (idle)	0.05 μ A	1.8V	0.09 μ W
SI7034	Sensor (sampling)	337 μ A	1.8V	0.61mW
TLV333	Receiver (opamp)	17 μ A	1.8V	30.6 μ W
LPV7215	Receiver (comparator)	0.58 μ A	1.8V	1.04 μ W
Bias Network	Receiver (biasing)	0.90 μ A	1.8V	1.62 μ W
TPS22917	Load switch (power gating), on	0.50 μ A	1.8V	0.90 μ W
TPS22917	Load switch (power gating), off	0.01 μ A	1.8V	0.02 μ W
TPS78318	LDO, quiescent	0.50 μ A	3.0V	1.5 μ W
TPS62740	Buck regulator, quiescent	0.36 μ A	3.0V	1.08 μ W

Table 8.1: Nominal power consumption of each component.

The power numbers for the microcontroller are with the program code executed from FLASH. These can be decreased slightly when configured to run the program code from SRAM. In addition, the idle power consumption is also presented here, but it is not assumed that duty cycling will be used at this stage of the experimental development.

The standby power consumption when all components are in an idle state, the microcontroller is in sleep and the receiver turned off (load switch off). The board components then consume 1.23 μ W from the 1.8V supply rail. When the board is powered from a 3V source, the total power consumption is 2.45 μ W with the buck regulator and 3.55 μ W with the low-dropout

(LDO) regulator.

When transmitting data, the peak power consumption of the board $51.49\mu\text{W}$ from the 1.8V supply rail. The total power consumption is $58.3\mu\text{W}$ with a buck regulator and $87.3\mu\text{W}$ with the LDO regulator. In receive mode, the receive circuitry will be turned on which consumes an additional $34.16\mu\text{W}$. The total power consumption is then $96.1\mu\text{W}$ with a buck regulator and $144.1\mu\text{W}$ with an LDO regulator. These numbers show that the desirable $100\mu\text{W}$ from the research question can be met.

Table 8.2 summarizes the current and power consumption for the different operational power profiles and the two regulator types. These will be verified with measurements to characterize power usage, and which parts (e.g. firmware or hardware, including MCU configuration) may be a limitation or subject to further optimizations.

The conversion from current consumption in the 1.8V domain to LDO and buck converter is done as follows. For a linear regulator, the output current is equal to the input current minus the part's quiescent current. The power is then calculated assuming a fixed 3V voltage source. For the buck regulator, the part performs a constant-power conversion between 1.8V and 3V: thereby the output power is equal to the input power while taking into account the conversion efficiency and the part's quiescent current.

It is assumed that the conversion efficiency is 90%, regardless of load power. Note that conversion efficiency does not equal to the total power supply efficiency, as the latter also takes into account the quiescent power draw of the buck regulator itself. This is a major reason why total efficiency will drop off significantly at low output powers. At high load powers, the conversion efficiency will drop off due to non-linear losses (e.g. $P_R = I^2 \cdot R$), however, it is a fair approximation that these are not dominant for sub mA load currents.

Function	Radio	I_{IN} LDO	I_{IN} Buck	P_{IN} LDO	P_{IN} Buck
CPU shutdown	Off	$1.18\mu\text{A}$	$0.81\mu\text{A}$	$3.55\mu\text{W}$	$2.45\mu\text{W}$
Receive CPU run	RX	$48.0\mu\text{A}$	$32.0\mu\text{A}$	$144.1\mu\text{W}$	$96.1\mu\text{W}$
Receive CPU idle	RX	$39.5\mu\text{A}$	$26.4\mu\text{A}$	$118.5\mu\text{W}$	$79.1\mu\text{W}$
Transmit CPU run	TX	$29.1\mu\text{A}$	$19.4\mu\text{A}$	$87.3\mu\text{W}$	$58.3\mu\text{W}$
Transmit CPU idle	TX	$20.6\mu\text{A}$	$13.8\mu\text{A}$	$61.9\mu\text{W}$	$41.3\mu\text{W}$

Table 8.2: Expected power consumption for the different board power profiles

8.2 Measurements

8.2.1 Base-band Packet Tests

To test the radio firmware functionality (in particular the BSP connecting to the radio phy and data link layer), a full radio packet has been synthesized such that it can be replayed on an arbitrary waveform generator (AWG). An AWG generator can be programmed to output any waveform using a series of digital samples.

Figure 8.3 shows the measurement setup. The diagram shows the receiver block diagram. The AWG generator is connected through the RF switch, with position fixed at 5 (bypass to the receiver). This measurement setup will also be used for sensitivity measurements, although the AWG generator is then replaced with a vector signal generator.

The packets that were being replaced by the AWG waveform, were successfully received by the receiver and firmware. The receiver has been verified to work for 1kHz and 10kHz bitrates.

The transmitter was manually verified by using an oscilloscope.

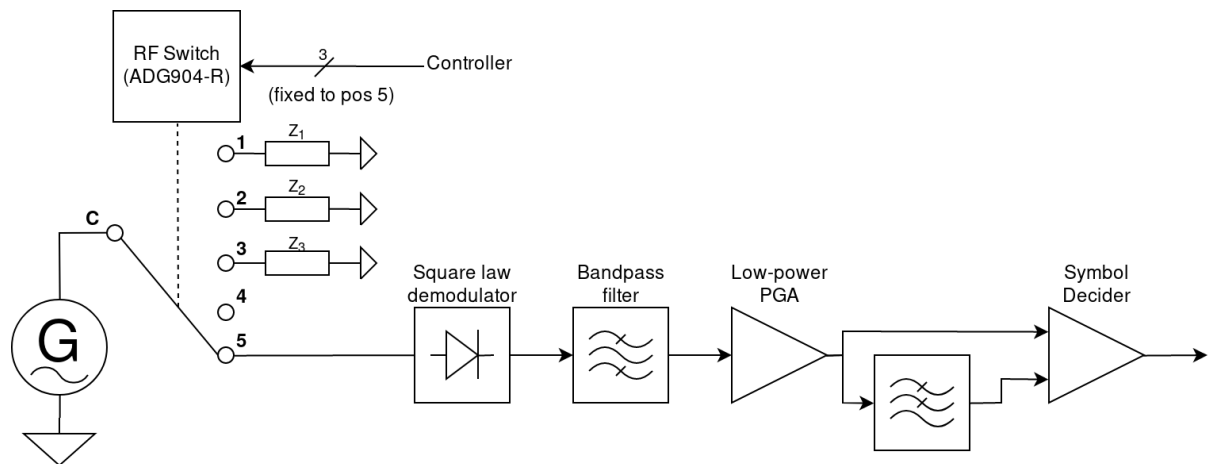


Figure 8.3: Baseband signal test of receiver using AWG

8.2.2 Sensitivity without exciter presence

The receiver sensitivity has been measured by applying a known amplitude modulated RF signal to the receiver. The measurement setup from figure 8.3 is also used here. Note that the SAW filter was not installed. The receiver has been programmed to then count the number of bit errors compared to the known test sequence. A status indicator will be turned on when the bit error of above 1% is detected.

A test has been performed with a continuous sequence of zeros and a continuous sequence of ones. For a 1kbit/s bitrate, a continuous sequence of zeros in FM0 line encoding can be created by programming a 1kHz ASK modulation at 100% modulation index. Similarly and a sequence of ones can be created with 500Hz modulation (1kbit/s throughput). The test signal has been generated at the 433.92MHz carrier frequency using an Agilent Technologies E8267D vector signal generator.

The sensitivity has been measured separately for each test sequence, and then the worst power figure has been taken at the sensitivity. It was found that for a continuous sequence of zeros, less conversion gain was available (due to -3dB of opamp circuit), and thus the sensitivity was slightly worse. This measurement approach also does not measure intersymbol interference (ISI), however, at this stage, the sensitivity improvement is of interest.

For a 10kHz test signal (10kbit/s), the minimum power level required for <1% BER was -43.2dBm. When the frequency is decreased to 1kHz, the minimum power level improves to -52.9dBm, which is 9.7dB better. This is almost exactly the improvement as was suggested in chapter 6.

The assumed voltage sensitivity of 30mV/ μ W was verified by applying a -30dBm test signal and verify the diode output amplitude, resulting in good correspondence with figure 6.3. The conversion gain of the diode detector and PGA amplifier was 41.9dB for 1kHz (50.8dB nominal) and 24.7dB for 10kHz (30.8dB nominal).

8.2.3 Sensitivity with exciter presence

The previous test assumed that the modulated signal has a modulation depth of 100%, and thereby there is no exciter presence. Table 8.3 and 8.4 show measured minimum modulation

index for a given average antenna port power P_{in} . Then, the P_{sig} and corresponding range-reach budget B (with an exciter of 30dBm) is calculated accordingly.

The signal power can be calculated from average power P_{in} and the modulation index m . In an ASK modulation, the generator will fluctuate the output power by a factor $+m$ and $-m$:

$$P_{in} = P_{in} \frac{1-m}{2} + P_{in} \frac{1+m}{2} \quad (8.1)$$

The signal power is then defined as the difference between the "high" output power and the "low" output power:

$$P_{sig} = P_{in} \frac{1+m}{2} - P_{in} \frac{1-m}{2} = P_{in} \cdot m \quad (8.2)$$

This suggests that a -60dBm sensitivity with 0dBm exciter incident wave, requires a receiver that can handle a modulation index of $10^{\frac{0-60}{10}} = 1ppm$. This is in contrast with chapter 3, where greater modulation indices of 400ppm or more were assumed. A 0dBm incident power level can be expected when a tag is deployed 3 meters from a 30dBm 434MHz exciter. Even at 30 meters from the exciter, an incident power level of -25dBm can be expected.

The results from 8.3 and 8.4 show that a backscatter receiver will always operate at these high power levels with degraded sensitivity. This is best visualized in graph 8.4, which plots the input power P_{in} against the signal sensitivity for 1kHz and 10kHz bit rates. In this compression region, the sensitivity of the receiver does not improve by a nominal 10dB any more if the bitrate changes by a factor of 10. Although the range-reach budget does improve for a lower bit rate, it is not by the expected $\sqrt{10}$ as was predicted in chapter 3 and 6.

P_{in} [dBm]	m	P_{sig} [dBm]	B [m^2]
0	0.107%	-29.7	2.9
-5	0.169%	-32.7	4.1
-10	0.273%	-35.6	5.8
-15	0.496%	-38.0	7.6
-20	0.975%	-40.1	9.7
-25	2.13%	-41.7	11.7
-30	5.36%	-42.7	13.1
-35	14.9%	-43.3	13.9
-40	41.3%	-43.8	14.9
-43.2	100%	-43.2	13.8

Table 8.3: Sensitivity test with exciter interference for a symbol rate of 10kHz

P_{in} [dBm]	m	P_{sig} [dBm]	B [m^2]
0	0.026%	-35.9	5.9
-5	0.033%	-39.8	9.4
-10	0.042%	-43.8	14.8
-15	0.063%	-47.0	21.4
-20	0.109%	-49.6	29.0
-25	0.240%	-51.2	34.7
-30	0.630%	-52.0	38.1
-35	1.85%	-52.3	39.6
-40	5.70%	-52.4	40.1
-45	17.0%	-52.7	41.3
-50	48.0%	-53.2	43.7
-52.9	100%	-52.9	42.3

Table 8.4: Sensitivity test with exciter interference for a symbol rate of 1kHz

8.2.4 Board Power Consumption

Table 8.5 shows the power measurement from the current firmware implementation. The micro-controller has been set-up as described in chapter 7. The power values have been determined

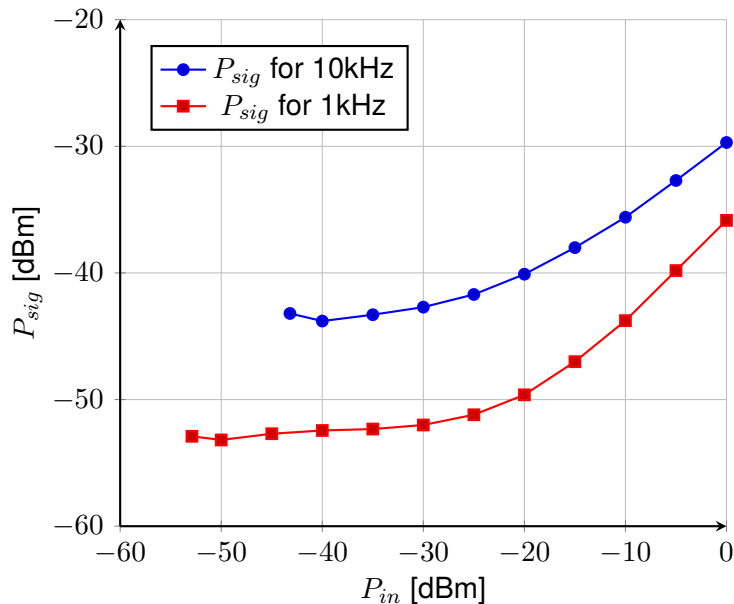


Figure 8.4: Sensitivity versus input power for 1kHz and 10kHz bitrate

by measuring the current consumption of the board with a multimeter, and then multiplying this with the supply voltage (nominal 3.0V).

In the CPU shutdown functionality, only the quiescent currents of all components matter. The receiver is turned off. From the expected power consumption (table 8.2), the board should consume $1.18\mu\text{A}$ (LDO) and $1.12\mu\text{A}$ (buck). The power consumption P_{IN} can be calculated by multiplying the currents with the nominal 3.0V supply voltage. For both power supplies, a $1.3\mu\text{A}$ consumption was measured, which is very close to the expected value.

When the board operates in receive mode, the microcontroller is either in active or idle mode, with the ADG904-R transmitter in idle, and the receiver active (load switch on). The current consumption on the 1.8V power domain is $47.51\mu\text{A}$ (CPU run) and $39.03\mu\text{A}$ (CPU idle). The LDO requires $0.5\mu\text{A}$ for regulation, thereby the expected current consumption is $48.01\mu\text{A}$ and $39.53\mu\text{A}$ for CPU run and idle respectively. The idle consumption is thereby $9.9\mu\text{A}$ higher than expected, and $17.3\mu\text{A}$ for sleep mode.

For transmit a similar result is shown: as it is expected that the board consumes $29.15\mu\text{A}$ and $20.67\mu\text{A}$ respectively (Transmit CPU run and idle respectively). The transmit idle is very close to expected (LDO), but in run it does not.

Giving the discrepancy in receiver idle, and an increased discrepancy when the microcontroller CPU is running, this suggests that both receiver and CPU has a greater than nominal power consumption.

The buck regulator converter, however, is working as expected. With a nominal efficiency of 90% at these low load currents ($<100\mu\text{A}$), it is indeed visible that the consumed power drops by approximately 33% when compared to the LDO implementation.

8.2.5 Observations

After the sensitivity tests and separate firmware verification, some informal tests have been performed to verify the backscatter operation with a +15dBm exciter. The exciter has been set up using the vector signal generator set at a fixed frequency and output power, and no modulation enabled.

Function	Radio	I_{IN} LDO	I_{IN} Buck	P_{IN} LDO	P_{IN} Buck
CPU shutdown	Off	$1.3\mu A$	$1.3\mu A$	$3.9\mu W$	$3.9\mu W$
Receive CPU run	RX	$65.3\mu A$	$44.8\mu A$	$196\mu W$	$134\mu W$
Receive CPU idle	RX	$49.4\mu A$	$34.4\mu A$	$148\mu W$	$103\mu W$
Transmit CPU run	TX	$39.8\mu A$	$26.9\mu A$	$119\mu W$	$80.7\mu W$
Transmit CPU idle	TX	$20.7\mu A$	$13.4\mu A$	$62.1\mu W$	$40.2\mu W$

Table 8.5: Measured power consumption for the different board power profiles

It was verified that backscatter transmission and reception works in using the 433.92MHz 15dBm carrier signal. It was also observed that the output amplitude of the detector has strong and weak spots, as was described as the phase cancellation problem by Shen et al.[20].

Tag-to-tag communication has been observed with distances up to 6 meters from the exciter, however, in this case, the transmitter and receiver antennas were placed next to each other (few centimetres apart). At 3 meters from the exciter, it was possible to place the tags more than half a meter apart. The firmware did not yet take advantage of the real and complex modulation pairs, so these distances may increase if these mitigations are implemented. It is important to stress then that these distance measurements are only a preliminary observation and not a conclusive measurement.

Unfortunately, the lab environment was not arranged such that larger range measurements could take place with a high level of confidence. With the motivation that is better to perform and document 1 good measurement rather than many bad measurements, it has been decided that in the interest of time to postpone these measurements to future work.

8.3 Results

The performed measurements and observations show that functioning tag-to-tag communication has realized using backscatter.

The power consumption measurements show that backscatter communication can be performed with low active power consumption while using off the shelf components. In this stage of implementation, the receive power is $134\mu W$ (no CPU duty cycling). The energy/bit figure of merit is then $134nJ/bit$ at 1kHz and $13.4\mu J/bit$ at 10kHz. For backscatter transmission, the energy/bit drops to $42.2nJ/bit$ and $4.22nJ/bit$ respectively.

This then means that radio reception is more expensive than transmission, which is the same conclusion as was found by Majid et al.[3]. The realized $134\mu W$ is slightly higher than the set goal as in the background research questions, but with further optimizations, sub- $100\mu W$ should be possible with the current hardware design.

The improvement in range-reach budget without exciter presence is as expected. However, it was observed that a P_{1dB} compression point is present at -30dBm, which dramatically decreases the radio performance. Resolving this compression point is potentially much more important than lowering the bit-rate at this stage of the investigation.

The compression point is observable in the datasheet of the HSMS-285B diode, as it the point at which the square law region starts. In addition, the ADG918 is electrically specified at a power level of 0dBm, and a maximum input power of 18dBm. The measurements were carried out without a SAW filter, thereby leaving only the detector circuit (in particular diode) as the cause for this compression.

9 | Conclusion & Discussion

9.1 Conclusion

The main research question that was raised at the start of this thesis was:

Can lowering the bitrate of a backscatter transceiver be used to increase the range of a multi-hop backscatter network?

From the mathematical definitions found in chapter 3, it was possible to find a first-order relationship between radio link budget and range for single-hop and multi-hop backscatter links. The definitions highlight the trade-off between the range (tag-to-tag distance) or reach (exciter-to-tag distance) choice in a backscatter tag placement, which is bounded by the range-reach budget, that can be calculated using the link budget.

Multi-hop backscatter network configurations can allow for a more efficient expenditure of the range-reach budget. From a two-dimensional placement analysis, it was reasoned that forward and backward channels exercise the best and worst placement for tag-to-tag communication respectively. By making use of tag-to-tag communication, it is possible to significantly improve the range or reach of a backscatter network.

The range-reach budget also highlights that a more sensitive receiver (more link budget) is required to satisfy the reach requirements. Even by utilizing multi-hop, a link budget of around 90dB is required to get up to 30m reach. Reducing the radio bit rate could be used to aid this goal. The receiver design chapter suggests, without accounting for compression point of the receiver, that at a bitrate of tenths of symbols per second, a "passive" receiver with -60dBm sensitivity could be realized.

An experimental tag platform has been designed which includes the backscatter transmitter (chapter 5), ASK receiver (chapter 6), firmware for controller (chapter 7) and power supply (chapter 4) to operate from a coin cell battery. The tag prototypes and energy optimized firmware show that it is possible to implement a tag with COTS components while staying close to the set goal of 100 μ W system power consumption.

However, despite the popularity of diode detectors in RFID and backscatter literature, it was found that these detectors have a significant dynamic range limitation, due to the strong presence of exciter power. A lower bitrate does show sensitivity improvements when considered without exciter, however, these improvements did not scale as expected.

The measurements show that only 6.2dB improvement was realized when a 0dBm exciter incident wave is present, whereas approximately 10dB was expected. This resulted in the range-reach budget only being doubled from $2.9m^2$ to $5.9m^2$, where an improvement to $9.2m^2$ was expected ($\sqrt{10}$). But perhaps most importantly is that the compression of the receiver degraded the range-reach budget by 86%.

9.2 Future Work

This work has shown that the design of a low power sensor node that is suitable for backscatter communication. After this master thesis work, the intention is to finalize the firmware, implement more power optimizations to approach the expected power consumption figures and build a sensor demonstrator on the platform.

In a survey of wake-up receivers[31], it was found that CMOS radio implementations outperform COTS variants significantly. However, wake-up receivers do not operate with the strong presence of an exciter signal, which is a special property of backscatter networks. Research into backscatter receivers with improved dynamic range is needed to improve the performance.

The assumption that multi-hop routing can be used in backscatter to improve the network coverage looks like it is still a valid promise, but needs to be demonstrated while adhering to the range-reach budget model. The model may need to be expanded to take additional radio parameters into account, such as fading, multi-path and other losses and higher path loss exponents. In addition, the trade-off between additional energy costs for relaying functions of tags and range/reach improvement remains unexplored.

Furthermore, the exciter has been assumed to be a static component in the network. However, if the exciter also has a scarce energy supply, then it could be useful to vary the exciter output power in time. The design space is open for future investigation.

Finally, as a general observation, the robustness of backscatter networking needs to be improved for wide-spread use. During experimentation, the issues such as phase cancellation, multi-path and non-linearity (compression) phenomena are assumed to be a limiting factor, where backscatter communication works only for a small fraction of the space.

A | Receiver Circuit Analysis

A.1 Model

In order to analyze the linear amplifier and filters in between, a model has been made as shown in figure A.1. The model is driven by the characterized output voltage V_D of the HSMS285x[62] diode detector, with output impedance R_j being the dynamic impedance of the diode. The output V_{out} is defined as a differential voltage output that is seen by the comparator. An intermediate voltage V_{in} is defined that specifies the voltage to GND at the non-inverting input of the operational amplifier. The output of the operational amplifier is named V_{op} .

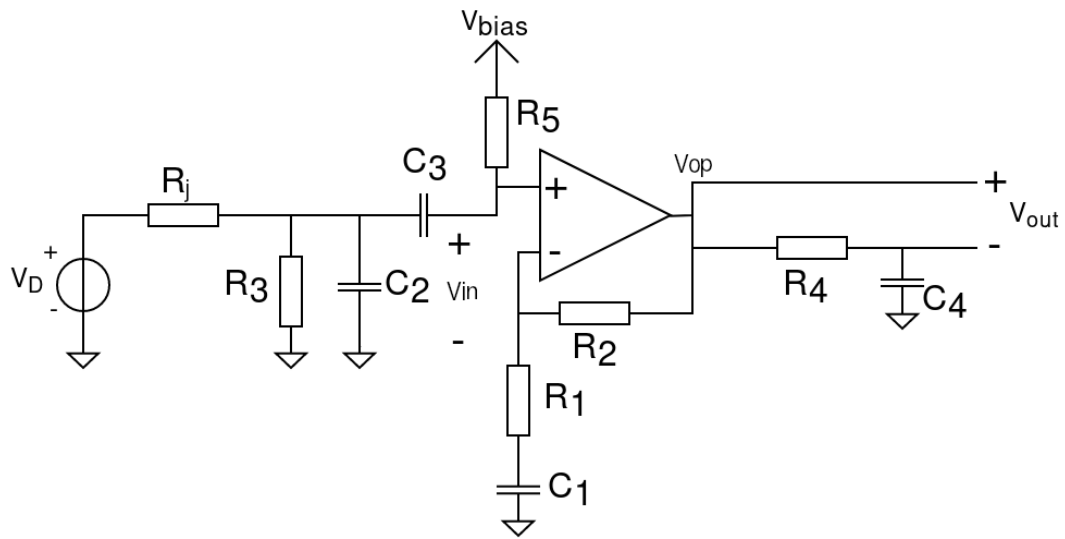


Figure A.1: Circuit of baseband processing part of the receiver

The opamp is replaced with a first order small signal model in figure A.2. The small signal model models an open-loop voltage gain with a finite bandwidth. The bandwidth is modelled using a single pole roll-off. This pole frequency can be calculated according to the gain-bandwidth product (GBW) from the opamp specifications. This refinement is needed to get accurate results for the AC performance, since the aim is to have a relatively high gain for a small pass-band. The differential input voltage of the opamp has been called V_a . The output supply V_{op} is a voltage dependent voltage source, and its transfer function and output voltage V_{op} is defined as:

$$H_{v-op}(s) = \frac{V_{op}}{V_a} = \frac{A_{VOL}}{1 + s\tau} \quad (\text{A.1}) \quad V_{op}(s) = V_a \frac{A_{VOL}}{1 + s\tau} \quad (\text{A.2})$$

with A_{VOL} the DC voltage open-loop gain of the amplifier, and τ the frequency roll-off of this amplifier. The GBW, A_{VOL} and τ can be calculated accordingly:

$$f_{GBW} = \frac{A_{VOL}\tau}{2\pi} \quad (\text{A.3}) \quad \tau = \frac{2\pi f_{GBW}}{A_{VOL}} \quad (\text{A.4})$$

With this definition, the opamp has an unity voltage gain at GBW frequency, i.e. $|H_{v-op}(2\pi f_{GBW})| \approx 1$.

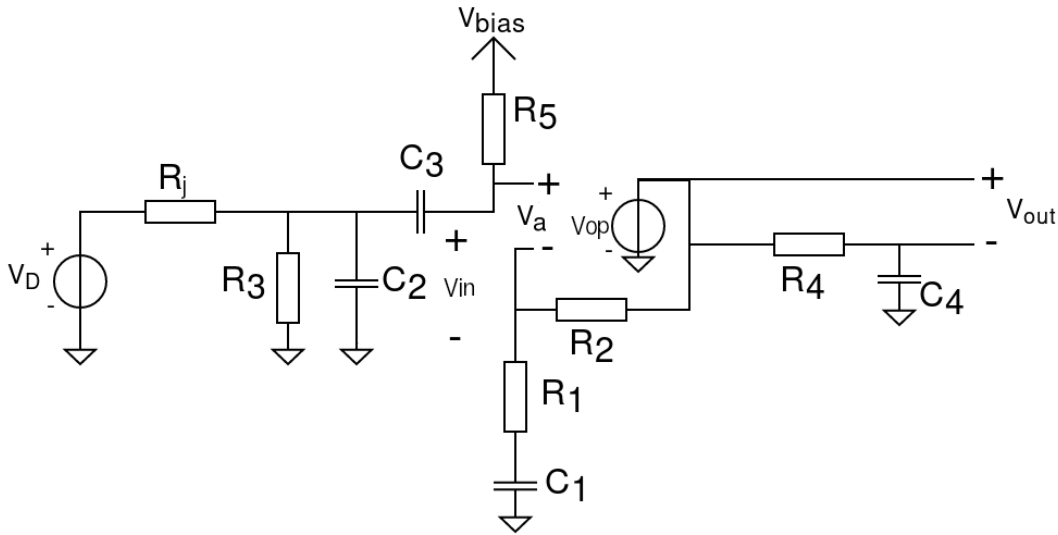


Figure A.2: Small signal model of the baseband processing circuit

A.2 Transfer Functions

This section models the transfer functions of all linear components in the receiver. The square law detector has been added into the input band-pass filter stage. It is assumed that the detector diode is unbiased, and a simple linearised model is assumed.

A.2.1 Input Band-pass filter

A small-signal AC model of the input band-pass filter has been drawn explicitly for analysis of the transfer function. The bias network V_{bias} has been replaced by the output impedance R_{bias} . The goal is to find $H_f = V_{in} / V_D$.

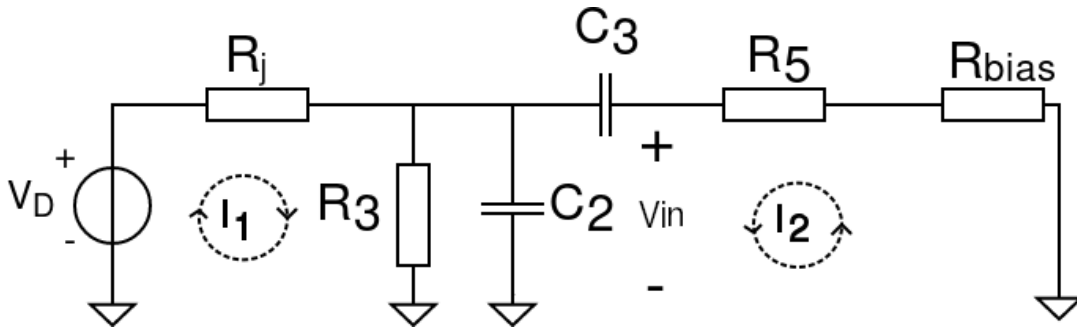


Figure A.3: Diode detector low-pass filter, and AC-coupling high-pass filter

The analysis of the circuit is performed by making use of 2 current loops I_1 and I_2 , and formulating a set of equations that describe the relationship between V_D and the circuit:

$$V_D = Z_f(I_1 + I_2) - R_j I_1 \quad (\text{A.5}) \quad V_D = (Z_{C_3} + R_5 + R_{bias})I_2 - R_j I_1 \quad (\text{A.6})$$

where $Z_{C_x} = \frac{1}{sC_x}$ with $x = 2, 3$ and $Z_f = \frac{R_3 Z_{C_2}}{R_3 + Z_{C_2}} = \frac{R_3}{1 + sR_3 C_2}$. The voltage V_{in} can be found by using $V_{in} = -I_2(R_5 + R_{bias})$. Therefore the set of equations is written in a linear system and solved for I_2 using Cramer's rule:

$$\begin{pmatrix} Z_f - R_j & Z_f \\ -R_j & Z_{C_3} + R_5 + R_{bias} \end{pmatrix} \begin{pmatrix} I_1 \\ I_2 \end{pmatrix} = \begin{pmatrix} V_D \\ V_D \end{pmatrix} \quad \begin{pmatrix} a_1 & b_1 \\ a_2 & b_2 \end{pmatrix} \begin{pmatrix} x \\ y \end{pmatrix} = \begin{pmatrix} c_1 \\ c_2 \end{pmatrix} \quad (\text{A.7})$$

With Cramer's rule, $x = \frac{c_1 b_2 - b_1 c_2}{a_1 b_2 - b_1 a_2}$ and $y = \frac{a_1 c_2 - c_1 a_2}{a_1 b_2 - b_1 a_2}$. The solution for I_2 , V_{in} and H_f is:

$$I_2(s) = \frac{(Z_f - R_j)(V_D) - (-R_j)(V_D)}{(Z_f - R_j)(Z_{C_3} + R_5 + R_{bias}) - (Z_f)(-R_j)} \quad (\text{A.9})$$

$$I_2(s) = \frac{Z_f V_D}{(Z_f - R_j)(Z_{C_3} + R_5 + R_{bias}) - (Z_f)(-R_j)} \quad (\text{A.10})$$

$$I_2(s) = \frac{V_D}{(1 - \frac{R_j}{Z_f})(Z_{C_3} + R_5 + R_{bias}) + R_j} \quad (\text{A.11})$$

$$V_{in}(s) = -I_2(R_5 + R_{bias}) = -\frac{V_D(R_5 + R_{bias})}{(1 - \frac{R_j}{Z_f})(Z_{C_3} + R_5 + R_{bias}) + R_j} \quad (\text{A.12})$$

$$H_f(s) = \frac{V_{in}}{V_D} = -\frac{R_5 + R_{bias}}{(1 - \frac{R_j}{Z_f})(Z_{C_3} + R_5 + R_{bias}) + R_j} \quad (\text{A.13})$$

$$H_f(s) = \frac{V_{in}}{V_D} = -\frac{R_5 + R_{bias}}{(1 - (1 + sR_3C_2)\frac{R_j}{R_3})(\frac{1}{sC_3} + R_5 + R_{bias}) + R_j} \quad (\text{A.14})$$

This equation suggests that it is optimal to choose high values ($\gg R_j$) for R_5 and R_{bias} . However, as will be shown more explicitly in the noise discussion, there is a trade-off between insertion loss and noise.

The denominator of $H_f(s)$ shows an interesting term $(1 - \frac{R_j}{Z_f})$. By matching the magnitude of Z_f (R_3 and C_2 in parallel) to match R_j , the most optimal transfer can be reached.

To not defer from the datasheet specification of the HSMS-285B diode[62], $R_3 = 100k\Omega$ as a nominal load. It is important to realize that the capacitor C_2 is charged through $R_j = 9k\Omega$, but discharged through $R_3 = 100k\Omega$. The -3dB frequency of this low-pass filter must then not be limited by $\tau = C_2 \cdot R_3$. For 10kHz bandwidth then the maximum value of C_2 is:

$$|Z_{C_2}| = \left| \frac{1}{j2\pi 10^4 C_2} \right| = 100k\Omega \rightarrow C_2 = 159pF \quad (\text{A.15})$$

It has been chosen to use $C_2 = 100pF$.

For the high-pass section, capacitor C_3 must be chosen high enough such that it will dominate the $Z_{C_3} + R_5 + R_{bias}$ term. If $R_5 + R_{bias} = 600k\Omega$ and the minimum symbol frequency is 100Hz, then $|Z_{C_3}(s)| \ll R_5 + R_{bias}$:

$$|Z_{C_3}(2\pi 100)| = \left| \frac{1}{j2\pi 10^2 C_3} \right| \ll 600k\Omega \rightarrow C_3 \gg 26.5pF \quad (\text{A.16})$$

Since the capacitor is part of a voltage divider, it is reasonable to pick a value several orders of magnitude higher than the calculated bound (10nF to 100nF).

A.2.2 PGA Transfer Function

The voltage transfer function of a feedback circuit can be formulated using the classic feedback formula $H(s) = \frac{Y}{X}(s) = \frac{A(s)}{1+A(s)\beta(s)}$ where A is the open-loop gain, and β is the feedback circuit[66]:

$$A(s) = \frac{A_{VOL}}{1+s\tau} \quad (\text{A.17}) \quad \beta(s) = \frac{Z_1}{Z_1+Z_2} \quad (\text{A.18})$$

$$H_v(s) = \frac{V_{op}(s)}{V_{in}(s)} = \frac{A_{OL}(s)}{1+\beta(s)A_{OL}(s)} = \frac{\frac{A_{VOL}}{1+s\tau}}{1+\frac{Z_1}{Z_1+Z_2}\frac{A_{VOL}}{1+s\tau}} = \frac{A_{VOL}}{1+s\tau+\frac{Z_1}{Z_1+Z_2}A_{VOL}} \quad (\text{A.19})$$

$$H_v(s) = \frac{A_{VOL}}{1+s\tau+\frac{R_1+\frac{1}{sC_1}}{R_1+R_2+\frac{1}{sC_1}}A_{VOL}} = \frac{A_{VOL}}{1+s\tau+\frac{sC_1R_1+1}{sC_1(R_1+R_2)+1}A_{VOL}} \quad (\text{A.20})$$

$$H_v(s) = \frac{A_{VOL}(sC_1(R_1+R_2)+1)}{(sC_1(R_1+R_2)+1)(1+s\tau)+(sC_1R_1+1)A_{VOL}} \quad (\text{A.21})$$

Solving for the poles and zeros in this transfer function results in the following solutions:

$$z_1 = -\frac{1}{\tau} \quad (\text{A.22}) \quad z_2 = -\frac{1}{C_1(R_1+R_2)} \quad (\text{A.24})$$

$$p_1 = -\frac{1}{\tau} \quad (\text{A.23}) \quad p_{2,3} = -\frac{\alpha \pm \sqrt{\alpha^2 - 4(1+A_{VOL})(R_1+R_2)C_1\tau}}{2C_1(R_1+R_2)\tau} \quad (\text{A.25})$$

with $\alpha = \tau + C_1(R_1(1+A_{VOL})+R_2)$. When $R_2 = (G-1)R_1\Omega$, then z_2 and $p_{2,3}$ are:

$$z'_2 = -\frac{1}{R_1C_1G} \quad (\text{A.26}) \quad p'_{2,3} = -\frac{\alpha' \pm \sqrt{\alpha'^2 - 4(1+A_{VOL})R_1C_1G\tau}}{2R_1C_1G\tau} \quad (\text{A.27})$$

with $\alpha' = \tau + R_1C_1(G+A_{VOL})$.

A.2.3 Resonance

It is important to note that this design can exhibit resonance if the value of C_1 is chosen too small, as the square root of $p_{2,3}$ can go negative. This creates a constraint $\alpha^2 - 4(1+A_{VOL})GR_1C_1\tau \geq 0$ which can then be solved for C_1 :

$$C_1 \geq \frac{A_{VOL}(2G-1)\tau - G - 2\sqrt{A_{VOL}(A_{VOL}(G-1)-G)G}}{(A_{VOL}+G)^2R_1} \quad (\text{A.28})$$

Despite the complexity of this equation, it shows that for lower values of R_1 a bigger value of C_1 must be used. However practical reasons may bound the value of R_1 , as C_1 may get infeasibly large (hundreds of μF), especially for extremely low bit rates where an extremely low zero frequency is necessary. Large capacitance values, beside their physical footprint, will also start to suffer from higher leakage which may influence the AC response of the PGA.

A.2.4 Comparator

The output voltage of the linear model is the differential voltage between the instantaneous PGA output and a filtered version. The transfer function of the output filter can be defined as $H_{lp} = \frac{V_{out}}{V_{op}}$:

$$V_{out}(s) = V_{op}(s)(1 - H_{lp}(s)) = V_{op}(s)\left(1 - \frac{1}{1 + R_4 C_4 s}\right) = V_{op}(s)\left(\frac{R_4 C_4 s}{1 + R_4 C_4 s}\right) \quad (\text{A.29})$$

Equation A.29 shows that the output circuit of the overall circuit is a high-passed variant of the operational amplifier output. From this relationship, it can be learned that $\tau_{cmp} = R_4 C_4$ must be chosen such that it cuts off frequencies below the lowest symbol frequency.

A.2.5 Complete Transfer Function

The previous paragraph have described the transfer functions from the band-pass filter, amplifier and comparator filter. Then the total front-end can be modelled as:

$$H_{bb}(s) = H_f(s)H_v(s)H_{lp}(s) = \frac{V_{in} V_{op} V_{out}}{V_D V_{in} V_{op}} = \frac{V_{out}}{V_D} \quad (\text{A.30})$$

where H_{bb} stands for the transfer function of the base-band signal processing. Figures A.4 and A.5 show bode plots for the TLV333 receiver tuned for 1kHz and 10kHz symbol rates respectively. The simulation show a conversion gain of 50dB for 1kHz and 30dB for 10kHz.

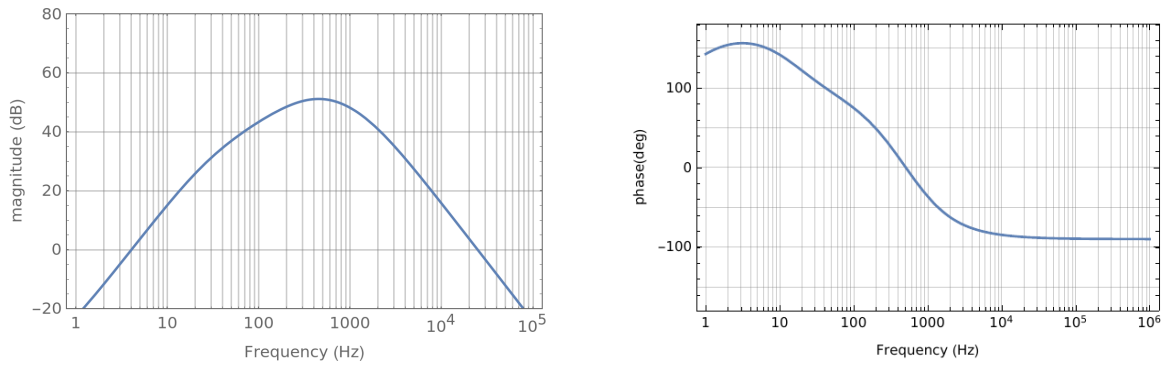


Figure A.4: Bode plot of baseband transfer function configured for 1kHz

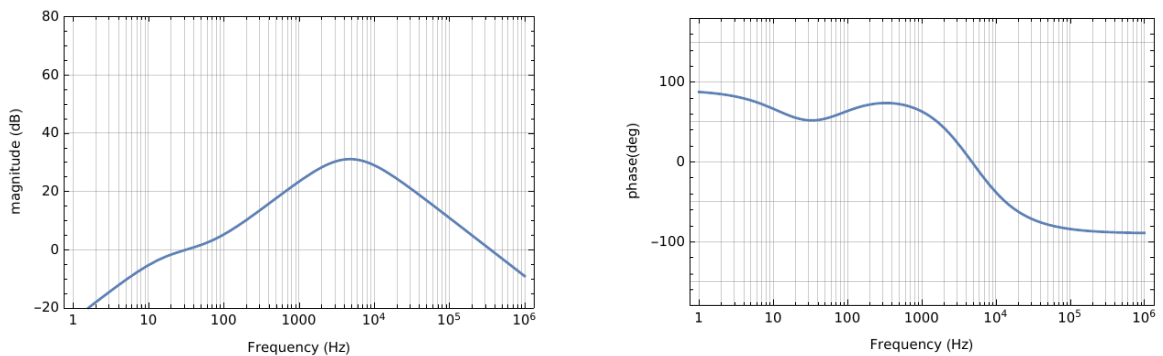


Figure A.5: Bode plot of baseband transfer function configured for 10kHz

A.3 Noise Sources

A.3.1 Diode detector

The HSMS-285x has a flicker noise specification of $-162\text{dBV}/\text{Hz}$ at 100Hz [62]. This figure equals to a noise density of $7.94\text{ nV}/\sqrt{\text{Hz}}$. However, at lower frequency the flicker noise increases with $10\text{dB}/\text{decade}$, which will limit SNR at lower bitrates. The graph A.6 shows how the noise temperature ratio as a function of frequency. The noise temperature ratio is calculated with the fraction of the diode's noise divided by the noise of a resistor $R = R_v$ [62].

Thereby, the reference of the graph at "0dB" can be calculated by using $R = R_v = 9\text{k}\Omega$. The baseline noise density is $12.2\text{nV}/\sqrt{\text{Hz}}$ ($-158\text{dBV}/\text{Hz}$)¹.

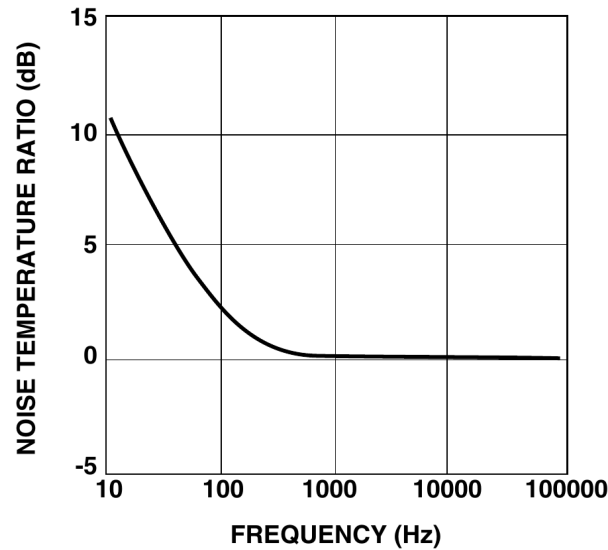


Figure A.6: Spectral noise density of HSMS-285x[62] as a function of frequency, with the reference of 0dB set at $v_n = 12.2\text{nV}/\sqrt{\text{Hz}}$ [62].

Other noise sources in the diode detector include $R_3 = 100\text{k}\Omega$, which magnitude can be deceiving. A $100\text{k}\Omega$ resistor has a voltage noise density of $41\text{nV}/\sqrt{\text{Hz}}$, which would suggest that the detector diode circuit performance is severely limited by this resistor, however this is not the case by examining the circuit qualitatively (by using figure A.3):

With superposition the voltage source V_D will be shorted to ground. When analyzing the circuit for LF, all capacitors can be seen as open-circuit. By removing C_3 , any transfer defined as $H = \frac{V_{in}}{V_{N-R3}}$ is inhibited, and thereby $H(0) = 0$.

Since the input filter creates a pass-band filter, it must be that $R_5C_3 \gg R_3C_2$ (high-pass pole must be above low-pass pole), and thereby there is a mid-band frequency where C_3 becomes rather low-impedance while C_2 is still high impedance. In that case the transfer function is roughly $\frac{R_j}{R_j+R_3} \approx \frac{9}{109}$. This introduces about 21dB of attenuation.

At higher frequencies, when C_2 starts to become low impedance, the resistor noise will be a low-pass filtered, exhibiting a $\frac{kT}{C}$ behavior[66]. With $R_2 = 100\text{k}\Omega$ and $C_2 = 18\text{nF}$, a pole of 88Hz will be created. Combined with 21dB of mid-band damping, the -3dB frequency of the noise source is at 1kHz.

With the 21dB attenuation, the resistor R_3 will introduce $3.7\text{nV}/\sqrt{\text{Hz}}$ measured at V_{in} .

¹For some unknown reason, this is a more pessimistic figure than the frontpage specification

A.3.2 Opamp bias network

Through LTspice simulations it has been determined that the bias network is important in the performance of this receiver. It was chosen that $R_5 = 100k\Omega$ for biasing the input of the opamp. The bias supply V_{bias} will be created using a resistive voltage divider of $2 \times 1M\Omega$ resistors and a $100nF$ capacitor in parallel.

Likewise with the detector circuit, relatively high impedance values are used. However, unfortunately any noise generated by R_5 has a direct transfer to V_{in} whenever C_3 is not conducting yet (for low frequencies at several Hz).

For mid band and higher frequencies, fortunately components R_5 , C_3 and $C_2 || R_j$ will create a potential divider to ground. Using LTspice simulations, it was determined that with $C_3 = 100nF$ the noise density at v_{in} is $10 - 12nV/\sqrt{Hz}$ at $1kHz$ and $100Hz$ respectively.

This is about equal magnitude as the detector diode, so not severely performance limiting, especially considering the creation of the bias supply costs $0.9\mu A$.

A.3.3 Opamp voltage noise

Typical low power op-amps have rather poor noise characteristics when compared to the aforementioned noise densities of passive and discrete components. Voltage noise densities as high as $160nV/\sqrt{Hz}$ has been seen for the MAX9914 amplifier[3].

Some op-amps suffer from flicker noise with relatively high corner frequencies of 1 to $10kHz$. These high corner frequencies means that the noise density is severely elevated at frequencies of interest.

In contrast, chopper operational amplifiers can have virtually no flicker noise altogether, since their input stage incorporates a chop function that mirrors the frequency spectrum. The output stage then "unmirrors" the frequency spectrum. Since all high-gain amplification occurs at non-DC frequencies, it is possible to avoid flicker noise. These architecture of op-amps are strongly preferred for receivers that target very low bit rates.

The transfer function $\frac{v_{in}}{v_{vn-op}}$ is unity. In addition the transfer function from V_{in} to V_{out} is also already known, making calculations from all noise sources to/from input or output possible with the previous definitions.

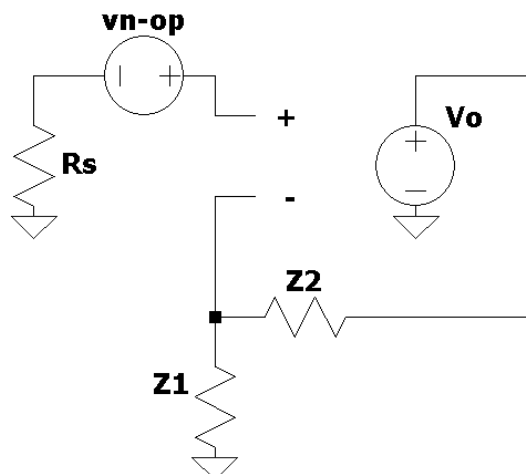


Figure A.7: Small-signal circuit of voltage noise of opamp

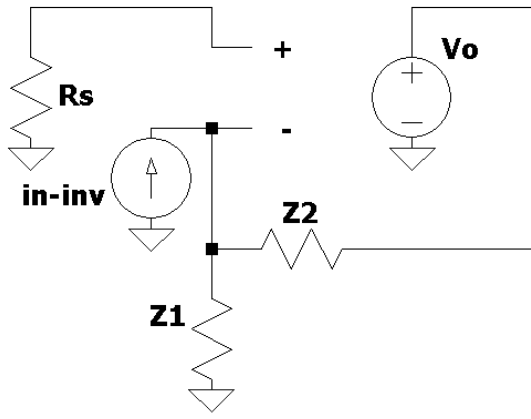


Figure A.8: Small-signal circuit of inverting current noise of opamp

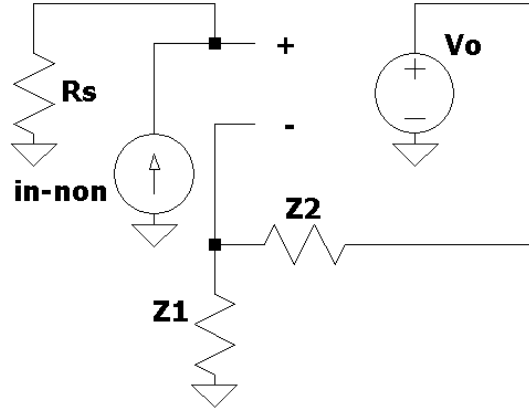


Figure A.9: Small-signal circuit of non-inverting current noise of opamp

A.3.4 Opamp current noise

An operational amplifier also suffers from current noise, which can be modelled as a current source parallel to each input. The small signal model circuits is shown in figure A.8 and A.9 for inverting and non-inverting terminals, respectively. The transfer functions for these sources to the output voltage of the opamp is shown in equations A.31 and A.32, for inverting and non-inverting terminals, respectively.

$$H_{in-inv}(s) = \frac{v_{op}}{i_{in-inv}} = R_2 \frac{A_{VOL}}{A_{VOL} + (1 + s\tau)(1 - \frac{sR_2C_2}{sR_1C_2 + 1})} \quad (\text{A.31})$$

For the inverting transfer function, high values of R_2 (to support high gain) will result in a rather high transconductance. Thereby the value of R_2 must be kept relatively low to set high gains. Fortunately the ratio $\frac{A_{VOL}}{A_{VOL} + (1 + s\tau)(1 - \frac{sR_2C_2}{sR_1C_2 + 1})}$ is always unity or less, since $R_2 \gg R_1$, thereby not elevating the already high transconductance of the noise source.

$$H_{in-non}(s) = \frac{v_{op}}{i_{in-non}} = R_s \frac{v_{op}}{v_{in}} = R_s H_v(s) \quad (\text{A.32})$$

For the non-inverting noise transfer, the output impedance of the band-pass filter is modelled as a single "resistor" R_s . This value must be kept low such that any generated noise is not amplified by $H_v(s)$. As was mentioned in the bias network section, with $R_5 = 100k\Omega$ and $R_{bias} = 500k\Omega$, the source impedance $R_s = R_5 + R_{bias} = 600k\Omega$.

A.3.5 Opamp feedback network

The noise contribution of R_2 to the output is almost unity, as shown in equation A.33

$$H_{vn-r2}(s) = \frac{v_{op}}{v_{vn-r2}} = \frac{\beta}{1 + \beta} \quad (\text{A.33})$$

For R_1 however, the opamp will directly see any noise on it's input pins. The transfer function for R_1 is expressed in equation A.34.

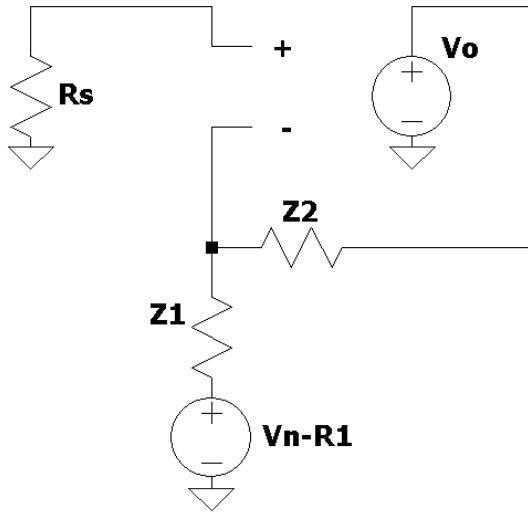


Figure A.10: Small-signal circuit of R_1 feedback resistor (in Z_1)

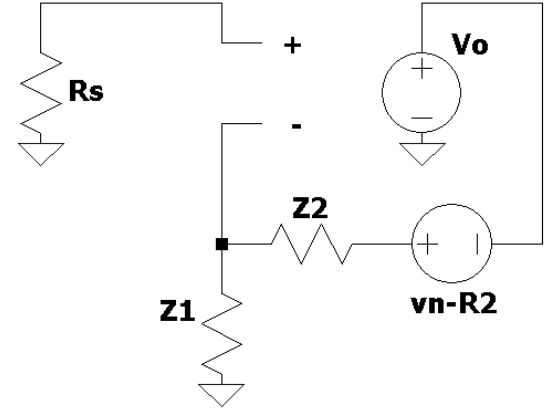


Figure A.11: Small-signal circuit of R_2 feedback resistor (in Z_2)

$$H_{v_{n-r1}}(s) = \frac{v_{op}}{v_{v_{n-r1}}} = -\frac{R_2}{Z_1+R_2} \frac{A_{VOL}}{1+A_{VOL}-A_{VOL}\frac{R_2}{Z_1+R_2}} \quad (\text{A.34})$$

$$= -\frac{R_2}{R_1+R_2+\frac{1}{sC_1}} \frac{A_{VOL}}{1+A_{VOL}-A_{VOL}\frac{R_2}{R_1+R_2+\frac{1}{sC_1}}} \quad (\text{A.35})$$

$$= -\frac{sR_2C_1}{s(R_1+R_2)C_1+1} \frac{A_{VOL}}{1+A_{VOL}-A_{VOL}\frac{sR_2C_1}{s(R_1+R_2)C_1+1}} \quad (\text{A.36})$$

$$= -\frac{A_{VOL}sR_2C_1}{(1+A_{VOL})(s(R_1+R_2)C_1+1)-A_{VOL}sR_2C_1}} \quad (\text{A.37})$$

When GBW roll-off w.r.t. A_{VOL} is neglected and assumed that $A_{VOL} \gg 1$, the expression can greatly simplified to show the pass-band gain of the noise source.

$$H_{v_{n-r1}}(s) \approx -\frac{sR_2C_1}{s(R_1+R_2)C_1+1-sR_2C_1} = -\frac{sR_2C_1}{sR_1C_1+1} \approx -\frac{R_2}{R_1} \quad (\text{A.38})$$

This confirms the intuition that the noise source is amplified like in an inverting voltage amplifier circuit. Therefore $v_{v_{n-r1}}$ has a much higher gain than $v_{v_{n-r2}}$.

A.3.6 Comparator filter

The R-C low pass filter is a classical example of a $\frac{kT}{C}$ circuit, where the value of the capacitor determines the noise power (Razavi, [66]). For $C_4 = 100nF$, the noise contribution is only $0.2\mu V$.

A.3.7 Total Result

Since the receiver will potentially be dealing with very low frequencies (tens of Hz), the $1/f$ noise has also been included. An example calculation is shown below for the input voltage noise of the operational amplifier. The calculation performs an integration of the spectral noise density $S_{v_{n-op-dens}}(s)$ across all frequencies, while taking into account the transfer function (Razavi, [66], p205-210).

$$v_{v_{n-c}}^2 = \int_0^\infty S_{v-c}(s) |H_{v-c}(s)|^2 ds \quad (\text{A.39})$$

where v_{vn-c} is the total noise voltage for component c , S_{v-c} is the noise voltage density as a function of s , and H_{v-c} is the transfer function of the noise source to the node of interest.

For resistors the noise density is flat, where the transfer function will introduce a frequency dependent noise behaviour to the output. For semiconductor devices, some flicker noise may be present (some op-amps or HSMS-285x diode [62]), which will be modelled using a single zero in the function of $S_v = S_{v-c}(1 + sz_1)$. In order to make the integral of A.39 convergent and computable in reasonable time (often only numerical results are computable), the integration bounds has been adjusted to 1mHz (10^{-3}) to 1MHz (10^6).

The noise amplitude of the complete receiver can be calculated by summing all v_{vn-c}^2 's and taking the square root:

$$v_{vn-out} = \sqrt{\sum_{c \in C} v_{vn-c}^2} \quad (\text{A.40})$$

where v_{vn-out} is the noise of the output node of interest, and the summation of component c in all of C will sum all noise sources (for each component) in the model.

The results of this model can be found in chapter 6.

A.4 Comparator Hysteresis

To prevent weak signals and/or noise from creating glitches and false switches on the comparator, some hysteresis must be set such that only the intended received signal is seen by the digital processor.

Figure A.12 shows a circuit to add positive feedback to the comparator such that this can be accomplished. The input level where V_{out} transitions from $V_{out|L}$ (output low) to $V_{out|H}$ (output high) is when:

$$V_{in|H} \frac{R_2}{R_1 + R_2} + V_{out|L} \frac{R_1}{R_1 + R_2} > V_{ref} \quad (\text{A.41})$$

This inequality describes the switching point when the non-inverting terminal is greater than the inverting terminal (neglecting comparator offset voltage). The non-inverting terminal voltage can be described as a superposition of the positive feedback from output through R_2 and the input voltage through R_1 .

The transition V_{out} from $V_{out|H}$ to $V_{out|L}$ is when:

$$V_{in|L} \frac{R_2}{R_1 + R_2} + V_{out|H} \frac{R_1}{R_1 + R_2} < V_{ref} \quad (\text{A.42})$$

If then $V_{in|L} = V_{ref} - V_{hys}$ and $V_{in|H} = V_{ref} + V_{hys}$:

$$(V_{ref} + V_{hys}) \frac{R_2}{R_1 + R_2} + V_{out|L} \frac{R_1}{R_1 + R_2} > V_{ref} \quad (\text{A.43})$$

$$(V_{ref} - V_{hys}) \frac{R_2}{R_1 + R_2} + V_{out|H} \frac{R_1}{R_1 + R_2} < V_{ref} \quad (\text{A.44})$$

These 2 inequalities can be turned into equalities to create a set of linear equations. Then:

$$(V_{ref} + V_{hys}) \frac{R_2}{R_1 + R_2} + V_{out|L} \frac{R_1}{R_1 + R_2} = V_{ref} \quad (\text{A.45})$$

$$(V_{ref} - V_{hys}) \frac{R_2}{R_1 + R_2} + V_{out|H} \frac{R_1}{R_1 + R_2} = V_{ref} \quad (\text{A.46})$$

Subtracting bottom from top equation:

$$2V_{hys} \frac{R_2}{R_1 + R_2} - (V_{out|H} - V_{out|L}) \frac{R_1}{R_1 + R_2} = 0 \quad (\text{A.47})$$

$$R_2 = \frac{V_{out|H} - V_{out|L}}{2V_{hys}} R_1 \quad (\text{A.48})$$

For the LPV7215 comparator circuit, then $V_{ref} = 0.9V$, $V_{hys} = 25mV$, $V_{out|L} = 0.1V$ and $V_{out|H} = 1.7V$. This can be satisfied with $R_1 = 10k\Omega$ and $R_2 = 32R_1 = 320k\Omega$.

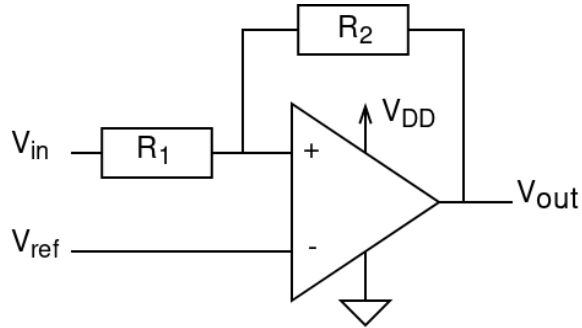
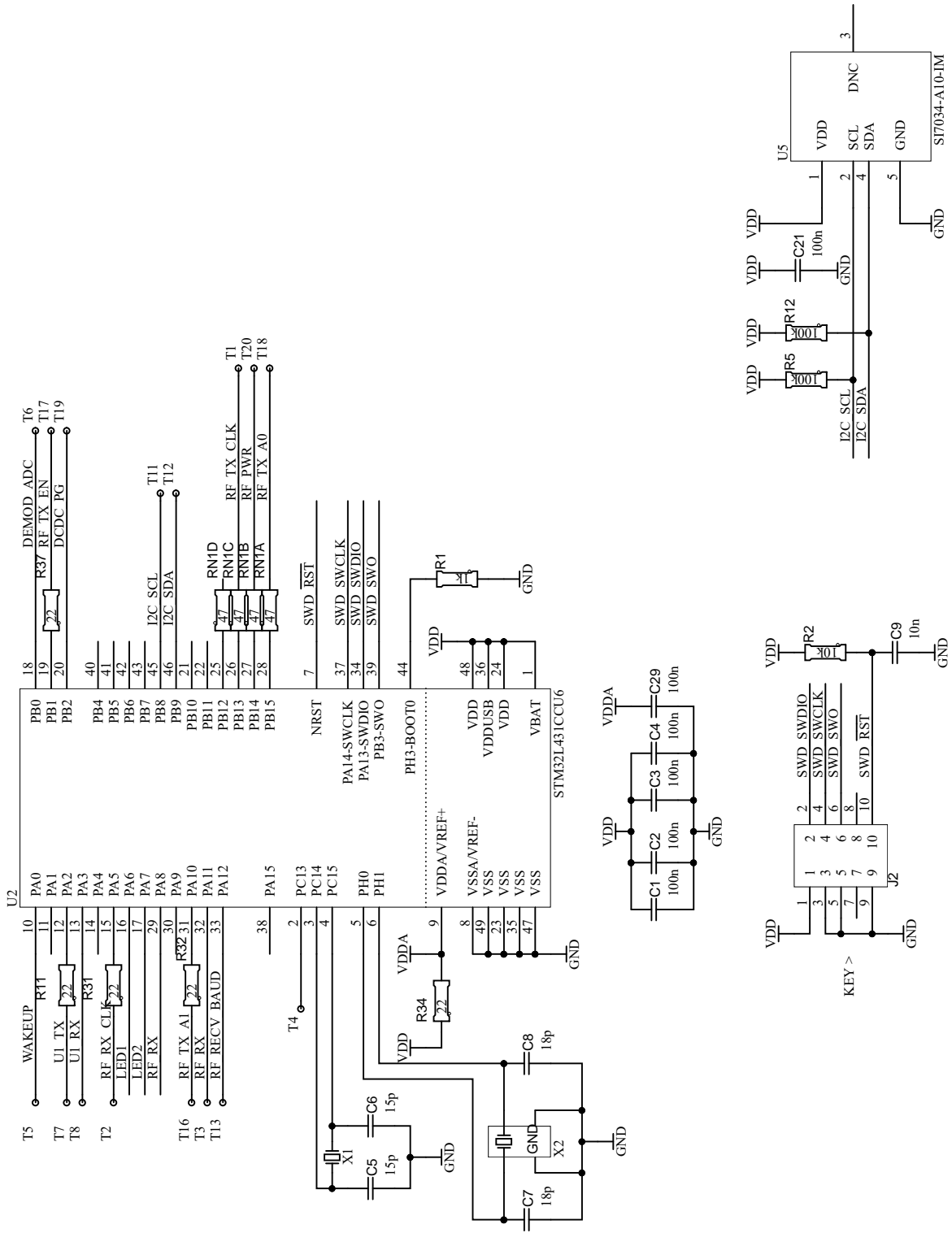


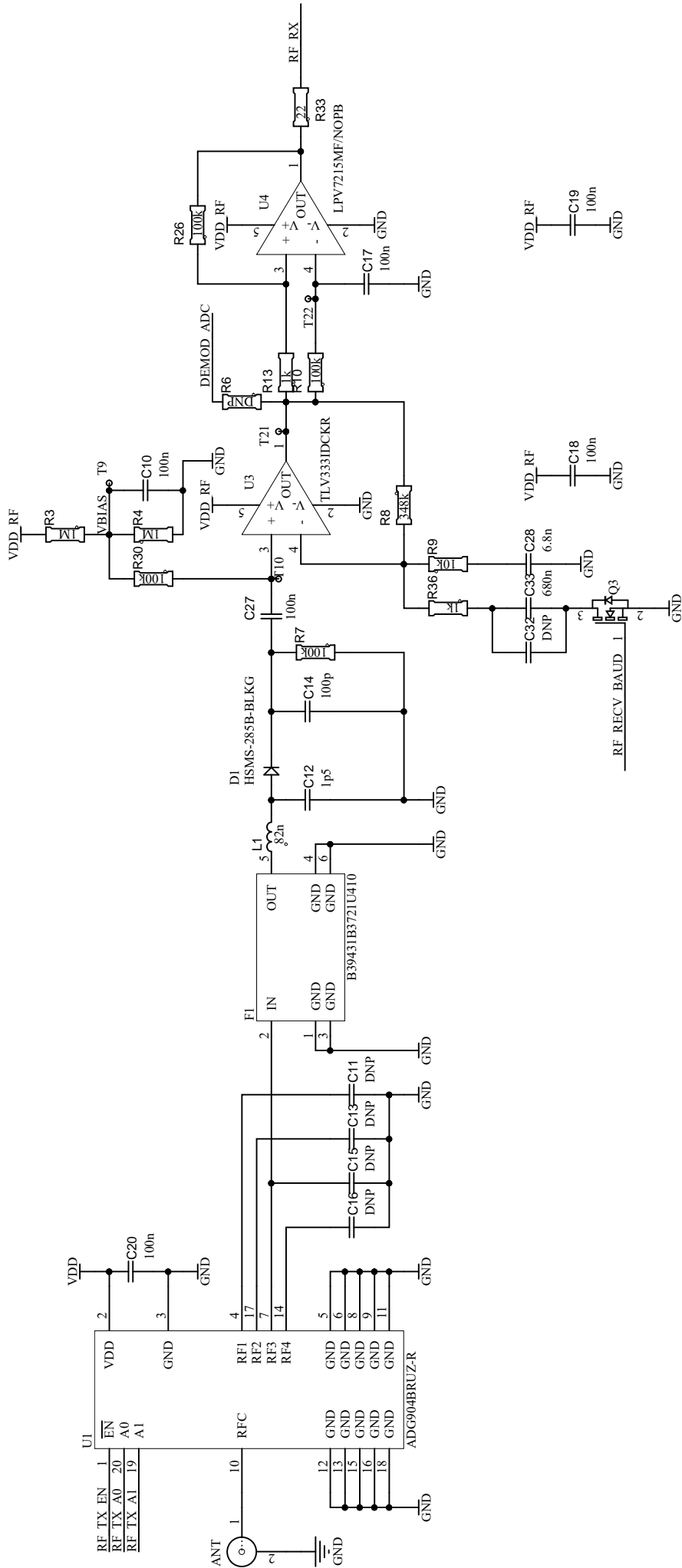
Figure A.12: Positive feedback loop in comparator to add hysteresis

B | Schematic & Bill of materials

Designator	Qty	Comment	Manufacturer	MPN
ANT	1	5-1814832-1	TE Connectivity	5-1814832-1
BAT1	1	CR2032 holder THT	Keystone	1066
C1, C2, C3, C4, C10, C17, C18, C19, C20, C21, C27, C29, C30	13	100nF 16V X7R 0402	Generic	
C12	1	1p5F 50V C0G 0402	Würth Elektronik	885012005002
C22, C23, C24, C25, C26, C34	6	10uF 6.3V X5R 0603	Generic	
C28	1	6.8nF 10V X5R 0603	Generic	
C33	1	680nF 10V X5R 0603	Generic	
C5, C6	2	15pF 50V C0G 0402	Generic	
C7, C8	2	18pF 50V C0G 0402	Generic	
C9	1	10nF 16V X7R 0402	Generic	
C14	1	100pF 16V X7R 0402	Generic	
D1	1	HSMS-285B-BLKG	Broadcom	HSMS-285B-BLKG
D2, D3	2	LED 0805 Green	Generic	
F1	1	433.92MHz SAW filter	Epcos	B39431B3721U410
J2	1	2x5 1.27mm pin header	Generic	
L1	1	MLK1005S82NJ	TDK	MLK1005S82NJ
L2	1	ELG-TEA2R2NA	Panasonic	ELG-TEA2R2NA
Q1, Q2, Q3	3	Signal NFET, 1Vthr	Rohm	RUC002N05HZGT116
R1, R36, R13, R14	5	0402 1% 1K	Generic	
R15				
R11, R28, R31, R32, R33, R34, R37	7	0402 1% 22R	Generic	
R2, R9	2	0402 1% 10K	Generic	
R22, R23, R24, R25, R29, R38, R39, R40	8	0402 1% 0R	Generic	
R27	1	0805 1% 0R	Generic	
R3, R4	2	0402 1% 1M	Generic	
R5, R7, R10, R12, R30, R26	6	0402 1% 100K	Generic	
R8	1	0402 1% 348K	Generic	
RN1	1	EXB-N8V470JX	Generic	
U1	1	ADG904BRUZ-R	Analog Devices	ADG904BRUZ-R
U2	1	STM32L431CCU6	STMicroelectronics	STM32L431CCU6
U3	1	TLV333IDCKR	Texas Instruments	TLV333IDCKR
U4	1	LPV7215MF/NOPB	Texas Instruments	LPV7215MF/NOPB
U5	1	SI7034-A10-IM	Silicon Labs	SI7034-A10-IM
U6	1	TPS62740DSST	Texas Instruments	TPS62740DSST
U7	1	TPS22917DBVT	Texas Instruments	TPS22917DBVT
U8	1	TPS78318DDCT	Texas Instruments	TPS78318DDCT
X1	1	ABS10-32.768KHZ-9-T	Abracon	ABS10-32.768KHZ-9-T
X2	1	12MHz 3.6x2.5mm	Generic	
C11	1	Backscatter Load 1	18nH 0402 inductor (Würth Elektronik, MPN: 744765118A)	
C13	1	Backscatter Load 2	7.3pF 0402 capacitor (Kemet, MPN: CBR04C739B5GAC)	
C15	1	Backscatter Load 3	DNP	
C16	1	Backscatter Load 4	0402 1% 0R	

Table B.1: Bill of materials of experimental radio board, listing component designators, quantity (qty), generic description and manufacturer with unique MPN (manufacturer part number).





Bibliography

- [1] *Nedap SENSIT parking sensors*. [Online]. Available: <https://www.nedapidentification.com/products/sensit/> (visited on Mar. 4, 2019).
- [2] *Nedap SENSIT Relay node datasheet*. [Online]. Available: <https://www.nedapidentification.com/products/sensit/sensit-relay-node/> (visited on Mar. 4, 2019).
- [3] A. Y. Majid, M. Jansen, G. O. Delgado, K. S. Yıldırım, and P. Pawełczak, “Multi-hop Backscatter Tag-to-Tag Networks”, en, Jan. 2019, arXiv: 1901.10274. [Online]. Available: <http://arxiv.org/abs/1901.10274> (visited on Feb. 4, 2019).
- [4] C. Liu and Z. J. Haas, “Multi-hop routing protocols for RFID systems with tag-to-tag communication”, en, *MILCOM 2017 - 2017 IEEE Military Communications Conference (MILCOM)*, Baltimore, MD: IEEE, Oct. 2017, pp. 563–568. [Online]. Available: <http://ieeexplore.ieee.org/document/8170764/> (visited on Sep. 6, 2018).
- [5] V. Liu, A. Parks, V. Talla, S. Gollakota, D. Wetherall, and J. R. Smith, “Ambient Backscatter: Wireless Communication Out of Thin Air”, en, p. 13, Oct. 2013.
- [6] V. Talla, M. Hessar, B. Kellogg, A. Najafi, J. R. Smith, and S. Gollakota, “LoRa Backscatter: Enabling The Vision of Ubiquitous Connectivity”, *Proc. ACM Interact. Mob. Wearable Ubiquitous Technol.*, vol. 1, no. 3, pp. 1–24, Sep. 2017.
- [7] A. Bachir, M. Dohler, T. Watteyne, and K. K. Leung, “MAC Essentials for Wireless Sensor Networks”, en, *IEEE Communications Surveys & Tutorials*, vol. 12, no. 2, pp. 222–248, 2010. [Online]. Available: <http://ieeexplore.ieee.org/document/5451759/> (visited on Oct. 21, 2018).
- [8] G. Anastasi, M. Conti, M. Di Francesco, and A. Passarella, “Energy conservation in wireless sensor networks: A survey”, en, *Ad Hoc Networks*, vol. 7, no. 3, pp. 537–568, May 2009. [Online]. Available: <http://linkinghub.elsevier.com/retrieve/pii/S1570870508000954> (visited on Oct. 24, 2018).
- [9] J. C. Bolomey, S. Capdevila, L. Jofre, and J. Romeu, “Electromagnetic Modeling of RFID-Modulated Scattering Mechanism. Application to Tag Performance Evaluation”, en, *Proceedings of the IEEE*, vol. 98, no. 9, pp. 1555–1569, Sep. 2010. [Online]. Available: <http://ieeexplore.ieee.org/document/5508334/> (visited on Oct. 18, 2018).
- [10] J. Ahn, H. Jang, H. Moon, J. Lee, and B. Lee, “Inductively Coupled Compact RFID Tag Antenna at 910 MHz With Near-Isotropic Radar Cross-Section (RCS) Patterns”, *IEEE Antennas and Wireless Propagation Letters*, vol. 6, pp. 518–520, 2007.
- [11] J.-P. Curty, M. Declercq, C. Dehollain, and N. Joehl, *Design and Optimization of Passive UHF RFID Systems*, en. Springer US, 2007. [Online]. Available: <http://www.springer.com/gp/book/9780387352749> (visited on Oct. 19, 2018).
- [12] J. F. Ensworth and M. S. Reynolds, “BLE-Backscatter: Ultralow-Power IoT Nodes Compatible With Bluetooth 4.0 Low Energy (BLE) Smartphones and Tablets”, en, *IEEE Transactions on Microwave Theory and Techniques*, vol. 65, no. 9, pp. 3360–3368, Sep. 2017. [Online]. Available: <http://ieeexplore.ieee.org/document/7898833/> (visited on Oct. 2, 2018).

- [13] *Wikipedia - Smith Chart*. [Online]. Available: https://en.wikipedia.org/wiki/Smith_chart (visited on Jul. 3, 2019).
- [14] J. Wei and X. Tian, "Capacity Analysis of Frequency Shift Based Backscatter Communication System", en, p. 5,
- [15] E. Kampionakis, J. Kimionis, K. Tountas, C. Konstantopoulos, E. Koutroulis, and A. Bletsas, "Backscatter sensor network for extended ranges and low cost with frequency modulators: Application on wireless humidity sensing", *2013 IEEE SENSORS*, Baltimore, MD: IEEE, Nov. 2013.
- [16] S. N. Daskalakis, R. Correia, G. Goussetis, M. M. Tentzeris, N. B. Carvalho, and A. Georgiadis, "Spectrally Efficient 4-PAM Ambient FM Backscattering for Wireless Sensing and RFID Applications", *2018 IEEE/MTT-S International Microwave Symposium - IMS*, Jun. 2018, pp. 266–269.
- [17] S. J. Thomas and M. S. Reynolds, "A 96 Mbit/sec, 15.5 pJ/bit 16-QAM modulator for UHF backscatter communication", en, *2012 IEEE International Conference on RFID (RFID)*, Orlando, FL, USA: IEEE, Apr. 2012, pp. 185–190. [Online]. Available: <http://ieeexplore.ieee.org/document/6193049/> (visited on Sep. 27, 2018).
- [18] J. Qian, A. N. Parks, J. R. Smith, F. Gao, and S. Jin, "IoT Communications with M-PSK Modulated Ambient Backscatter: Algorithm, Analysis, and Implementation", en, *IEEE Internet of Things Journal*, pp. 1–1, 2018. [Online]. Available: <https://ieeexplore.ieee.org/document/8423609/> (visited on Sep. 7, 2018).
- [19] J. Ryoo, J. Jian, A. Athalye, S. R. Das, and M. Stanaćević, "Design and Evaluation of "BTTN": A Backscattering Tag-to-Tag Network", *IEEE Internet of Things Journal*, vol. 5, no. 4, pp. 2844–2855, Aug. 2018.
- [20] Z. Shen, A. Athalye, and P. M. Djuric, "Phase Cancellation in Backscatter-Based Tag-to-Tag Communication Systems", en, *IEEE Internet of Things Journal*, vol. 3, no. 6, pp. 959–970, Dec. 2016. [Online]. Available: <http://ieeexplore.ieee.org/document/7419631/> (visited on Nov. 26, 2018).
- [21] P. Zhang, D. Bharadia, K. Joshi, and S. Katti, "HitchHike: Practical Backscatter Using Commodity WiFi", en, *Proceedings of the 14th ACM Conference on Embedded Network Sensor Systems CD-ROM - SenSys '16*, Stanford, CA, USA: ACM Press, 2016, pp. 259–271. [Online]. Available: <http://dl.acm.org/citation.cfm?doid=2994551.2994565> (visited on Sep. 27, 2018).
- [22] *Wikipedia - Radar Cross Section*. [Online]. Available: https://en.wikipedia.org/wiki/Radar_cross-section (visited on Feb. 26, 2019).
- [23] R. Harrington, "Electromagnetic scattering by antennas", en, *IEEE Transactions on Antennas and Propagation*, vol. 11, no. 5, pp. 595–596, Sep. 1963. [Online]. Available: <http://ieeexplore.ieee.org/document/1138078/> (visited on Apr. 26, 2019).
- [24] P. Nikitin, K. Rao, and R. Martinez, "Differential RCS of RFID tag", en, *Electronics Letters*, vol. 43, no. 8, p. 431, 2007. [Online]. Available: http://digital-library.theiet.org/content/journals/10.1049/e1_20070253 (visited on Nov. 27, 2018).
- [25] N. V. Huynh, D. T. Hoang, X. Lu, D. Niyato, P. Wang, and D. I. Kim, "Ambient Backscatter Communications: A Contemporary Survey", *IEEE Communications Surveys Tutorials*, pp. 1–1, 2018.

- [26] V. Iyer, V. Talla, B. Kellogg, S. Gollakota, and J. Smith, "Inter-Technology Backscatter: Towards Internet Connectivity for Implanted Devices", en, *Proceedings of the 2016 conference on ACM SIGCOMM 2016 Conference - SIGCOMM '16*, Florianopolis, Brazil: ACM Press, 2016, pp. 356–369. [Online]. Available: <http://dl.acm.org/citation.cfm?doid=2934872.2934894> (visited on Oct. 20, 2018).
- [27] A. Varshney, O. Harms, C. P. Penichet, C. Rohner, F. Hermans, and T. Voigt, "LoRea: A Backscatter Architecture that Achieves a Long Communication Range", *arXiv:1611.00096 [cs]*, Oct. 2016, arXiv: 1611.00096. [Online]. Available: <http://arxiv.org/abs/1611.00096> (visited on Sep. 5, 2018).
- [28] A. N. Parks, A. P. Sample, Y. Zhao, and J. R. Smith, "A Wireless Sensing Platform Utilizing Ambient RF Energy", en, p. 3,
- [29] Y. Karimi, A. Athalye, S. R. Das, P. M. Djurić, and M. Stanačević, "Design of a backscatter-based Tag-to-Tag system", *2017 IEEE International Conference on RFID (RFID)*, May 2017, pp. 6–12.
- [30] E. Nilsson and C. Svensson, "Power Consumption of Integrated Low-Power Receivers", en, *IEEE Journal on Emerging and Selected Topics in Circuits and Systems*, vol. 4, no. 3, pp. 273–283, Sep. 2014. [Online]. Available: <http://ieeexplore.ieee.org/document/6866244/> (visited on Sep. 21, 2018).
- [31] R. Piyare, A. L. Murphy, C. Kiraly, P. Tosato, and D. Brunelli, "Ultra Low Power Wake-Up Radios: A Hardware and Networking Survey", en, *IEEE Communications Surveys & Tutorials*, vol. 19, no. 4, pp. 2117–2157, 2017. [Online]. Available: <http://ieeexplore.ieee.org/document/7990121/> (visited on Sep. 30, 2018).
- [32] J. Griffin and G. Durgin, "Complete Link Budgets for Backscatter-Radio and RFID Systems", en, *IEEE Antennas and Propagation Magazine*, vol. 51, no. 2, pp. 11–25, Apr. 2009. [Online]. Available: <http://ieeexplore.ieee.org/document/5162013/> (visited on Nov. 11, 2018).
- [33] "EPCglobal Gen2 Specification", en, p. 152,
- [34] C. R. Valenta and G. D. Durgin, "Harvesting Wireless Power: Survey of Energy-Harvester Conversion Efficiency in Far-Field, Wireless Power Transfer Systems", en, *IEEE Microwave Magazine*, vol. 15, no. 4, pp. 108–120, Jun. 2014. [Online]. Available: <http://ieeexplore.ieee.org/document/6810996/> (visited on Mar. 4, 2019).
- [35] J. Blanckenstein, J. Klaue, and H. Karl, "A Survey of Low-Power Transceivers and Their Applications", en, *IEEE Circuits and Systems Magazine*, vol. 15, no. 3, pp. 6–17, 2015. [Online]. Available: <http://ieeexplore.ieee.org/document/7206826/> (visited on Mar. 4, 2019).
- [36] C. A. Repec, "Regulatory status for using RFID in the EPC Gen2 (860 to 960 MHz) band of the UHF spectrum", en, p. 18, 2019.
- [37] P. Zhang, P. Hu, V. Pasikanti, and D. Ganesan, "EkhoNet: High speed ultra low-power backscatter for next generation sensors", en, *Proceedings of the 20th annual international conference on Mobile computing and networking - MobiCom '14*, Maui, Hawaii, USA: ACM Press, 2014, pp. 557–568. [Online]. Available: <http://dl.acm.org/citation.cfm?doid=2639108.2639138> (visited on Sep. 25, 2018).
- [38] *STMicroelectronics STM32L412 Datasheet*. [Online]. Available: <https://www.st.com/en/microcontrollers-microprocessors/stm32l412cb.html> (visited on Apr. 17, 2019).

- [39] *Microchip ATSAM11e16a Datasheet*. [Online]. Available: <https://www.microchip.com/wwwproducts/en/ATSAML10E16A> (visited on Apr. 17, 2019).
- [40] *STMicroelectronics STM32I431 Datasheet*. [Online]. Available: <https://www.st.com/en/microcontrollers-microprocessors/stm32i431cc.html> (visited on Apr. 17, 2019).
- [41] *STMicroelectronics STM32I011 Datasheet*. [Online]. Available: <https://www.st.com/en/microcontrollers-microprocessors/stm32i011k4.html> (visited on Apr. 17, 2019).
- [42] *Ambiq Micro Apollo2 Datasheet*. [Online]. Available: <https://ambiqmicro.com/mcu/> (visited on Apr. 17, 2019).
- [43] *Texas Instruments MSP430FR5969 Datasheet*. [Online]. Available: <http://www.ti.com/product/MSP430FR5969> (visited on Apr. 17, 2019).
- [44] *Microchip ATXMEGA32e5 Datasheet*. [Online]. Available: <https://www.microchip.com/wwwproducts/en/ATXmega32E5#datasheet-toggle> (visited on Apr. 17, 2019).
- [45] M. Hesar, A. Najafi, and S. Gollakota, "NetScatter: Enabling Large-Scale Backscatter Networks", en, *arXiv:1808.05195 [cs]*, Aug. 2018, arXiv: 1808.05195. [Online]. Available: <http://arxiv.org/abs/1808.05195> (visited on Sep. 8, 2018).
- [46] C. Pérez-Penichet, C. Noda, A. Varshney, and T. Voigt, "Battery-free 802.15.4 Receiver", en, p. 12, 2018.
- [47] J. F. Ensworth, A. T. Hoang, T. Q. Phu, and M. S. Reynolds, "Full-duplex Bluetooth Low Energy (BLE) compatible Backscatter communication system for mobile devices", *2017 IEEE Topical Conference on Wireless Sensors and Sensor Networks (WiSNet)*, Jan. 2017, pp. 45–48.
- [48] J. Pandey and B. P. Otis, "A Sub-100 uW MICS/ISM Band Transmitter Based on Injection-Locking and Frequency Multiplication", en, *IEEE Journal of Solid-State Circuits*, vol. 46, no. 5, pp. 1049–1058, May 2011. [Online]. Available: <http://ieeexplore.ieee.org/document/5741743/> (visited on Feb. 18, 2019).
- [49] H. Chen, C. Zhai, Y. Li, and B. Vucetic, "Cooperative Strategies for Wireless-Powered Communications: An Overview", *IEEE Wireless Communications*, vol. 25, no. 4, pp. 112–119, Aug. 2018.
- [50] M. Babaie, F.-W. Kuo, H.-N. R. Chen, L.-C. Cho, C.-P. Jou, F.-L. Hsueh, M. Shahmohammadi, and R. B. Staszewski, "A Fully Integrated Bluetooth Low-Energy Transmitter in 28 nm CMOS With 36% System Efficiency at 3 dBm", en, *IEEE Journal of Solid-State Circuits*, vol. 51, no. 7, pp. 1547–1565, Jul. 2016. [Online]. Available: <http://ieeexplore.ieee.org/document/7476842/> (visited on Feb. 18, 2019).
- [51] X. Huang, S. Rampu, X. Wang, G. Dolmans, and H. de Groot, "A 2.4ghz/915mhz 5 uW wake-up receiver with offset and noise suppression", en, *2010 IEEE International Solid-State Circuits Conference - (ISSCC)*, San Francisco, CA, USA: IEEE, Feb. 2010, pp. 222–223. [Online]. Available: <http://ieeexplore.ieee.org/document/5433958/> (visited on Dec. 13, 2018).
- [52] X. Huang, P. Harpe, G. Dolmans, H. de Groot, and J. R. Long, "A 780–950 MHz, 64–146 uW Power-Scalable Synchronized-Switching OOK Receiver for Wireless Event-Driven Applications", en, *IEEE J. Solid-State Circuits*, vol. 49, no. 5, pp. 1135–1147, May 2014. [Online]. Available: <http://ieeexplore.ieee.org/document/6763014/> (visited on Jun. 13, 2019).

- [53] *Silicon Labs SI4455-C datasheet*. [Online]. Available: <https://www.silabs.com/documents/public/data-sheets/Si4455.pdf> (visited on Mar. 7, 2019).
- [54] *Texas Instruments CC1101 Datasheet*. [Online]. Available: <https://www.silabs.com/documents/public/data-sheets/Si4455.pdf> (visited on Mar. 7, 2019).
- [55] *Texas Instruments TPS62740 Datasheet*. [Online]. Available: <http://www.ti.com/product/TPS62740> (visited on Apr. 17, 2019).
- [56] *Texas Instruments TPS22917 Datasheet*. [Online]. Available: <http://www.ti.com/product/TPS22917#> (visited on Apr. 17, 2019).
- [57] *MicroSemi IGLOO nano FPGA series Datasheet*. [Online]. Available: <https://www.microsemi.com/product-directory/fpgas/1689-igloo#igloo-nano> (visited on Apr. 17, 2019).
- [58] *EEMBC ULPmark information*. [Online]. Available: <https://www.eembc.org/ulpmark/index.php> (visited on Apr. 17, 2019).
- [59] *EEMBC ULPmark-CP and ULPmark-PP scores*. [Online]. Available: <https://www.eembc.org/ulpmark/scores.php> (visited on Apr. 17, 2019).
- [60] *STMicroelectronics STM32cubemx design software*. [Online]. Available: <https://www.st.com/en/development-tools/stm32cubemx.html> (visited on Apr. 17, 2019).
- [61] *Analog Devices ADG904 & ADG904-R Datasheet*. [Online]. Available: <https://www.analog.com/en/products/adg904.html> (visited on Oct. 18, 2018).
- [62] *HSMS-285x Datasheet*. [Online]. Available: <https://www.broadcom.com/products/wireless/diodes/schottky/hsms-2852> (visited on Mar. 7, 2019).
- [63] *HSMS-286x Datasheet*. [Online]. Available: <https://www.broadcom.com/products/wireless/diodes/schottky/hsms-2862> (visited on Mar. 7, 2019).
- [64] A. Cowley and H. Sorensen, "Quantitative Comparison of Solid-State Microwave Detectors", en, *IEEE Transactions on Microwave Theory and Techniques*, vol. 14, no. 12, pp. 588–602, Dec. 1966. [Online]. Available: <http://ieeexplore.ieee.org/document/1126337/> (visited on Mar. 1, 2019).
- [65] *Texas Instruments TLV333 Datasheet*. [Online]. Available: <http://www.ti.com/product/TLV333> (visited on Apr. 17, 2019).
- [66] B. Razavi, *Design of Analog CMOS Integrated Circuits*. 2001.